博士論文

Two-dimensional transition metal carbides MXenes as a charge storage host in hydrate melt electrolyte

（常温溶融水和物中での二次元遷移金属炭化物 MXene の電荷貯蔵機能）

金 基宰 (Kijae Kim)

Department of Chemical System Engineering

Graduate School of Engineering

The University of Tokyo

Table of contents

Chapter 1: General introduction

Owing to growing concerns about climate changes and air pollution from the burning of fossil fuels and depletion of the world fossil energy resources, many researchers and policymakers have started to turn their attention to energy storage solutions.[1,2] Indeed, energy storage systems can help to solve issues related to the intermittent nature of renewable energies such as solar and wind power; it can also, in many cases, make a smart grid city quick to respond to large fluctuations in the demand and hence reducing the needs of backup power sources.[3-5] The performance of an energy storage system is determined by how rapidly it can react to changes in the demand, how quickly it can be charged and discharged, and how largely it can store the energy. To make the grid city smarter and eco-friendly, a broad range of applications (*e.g.*, UPS, electric vehicle, renewable energy) requires the high performances of energy storage such as fast charge/discharge capability, long cycle life, good safety, and high energy density as shown in **Figure 1.1**.[6-8] Therefore, many energy storage materials and mechanism (intercalation, alloying, conversion, and adsorption) have been widely explored to provide higher energy and power densities.[9,10]

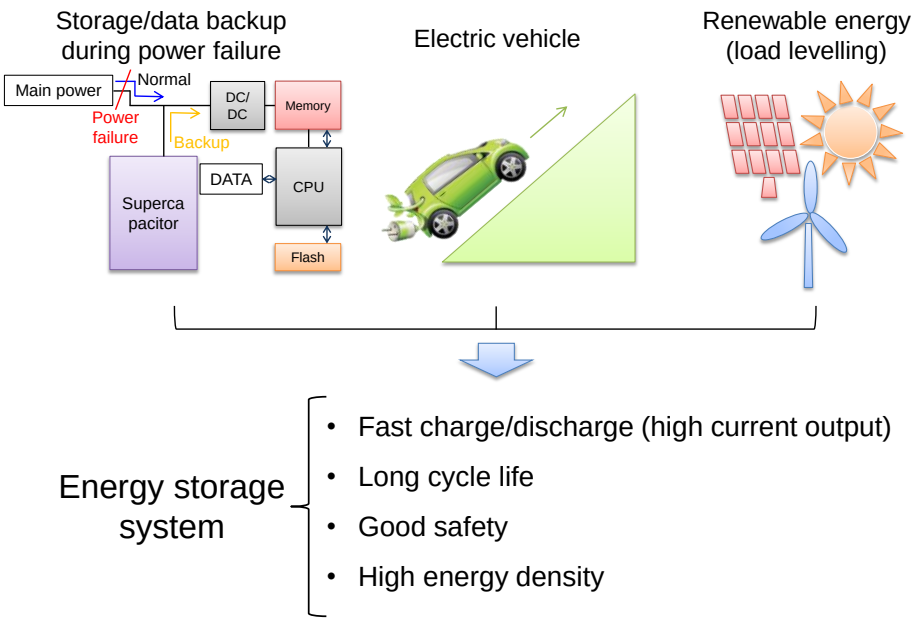

Figure 1.1 Many applications require the high performance of energy storage system for eco-friendly smart grid city. For examples, energy storage system is used as a backup source during power failure. Instead of fossil fuels, energy storage system acts as a power source for electric vehicle. Energy storage system is needed for intermittent nature of renewable energies.

Li-ion batteries have widely been used for a variety of applications such as portable electronic devices (*e.g.*, cellular phone, laptop, and camera) and electric vehicles.[11,12] Lithium has a light molecular weight and a low negative electrode potential (E = -3.04 V, Li^+/Li vs. standard hydrogen electrode).[13] Thus, commercial Li-ion batteries provide large energy density (> 200 Wh/kg).[14] Li-ion batteries operate via chemical reactions converting between chemical energy and electric energy where Li-ions are transferred between a cathode and an anode through an electrolyte. Li-ion batteries largely consist of the cathode, anode, electrolyte, and separator. As for commercial Li-ion batteries, metal oxides (*e.g.*, $LiCoO_2$)[15] and graphite[16] are widely used as active materials in the cathode and anode. Electrolyte plays critical role in transporting Li-ions, and separator acts as a membrane of Li-ion transport while blocking electrical short between the cathode and anode. As shown in **Figure 1.2**, Li-ions transport from the cathode (*e.g.*, $LiCoO_2$) to the anode (*e.g.*, graphite) through the electrolyte and separator during discharge process; on charge process, Li-ions flow reversely from the anode to cathode. Although Li-ion rechargeable batteries have been the most studied and widely commercialized as energy storage devices due to the high energy densities, their low power densities coming from low ionic conductivity and high Li-ion diffusion energy barrier in electrode limit further applications requiring high current output.

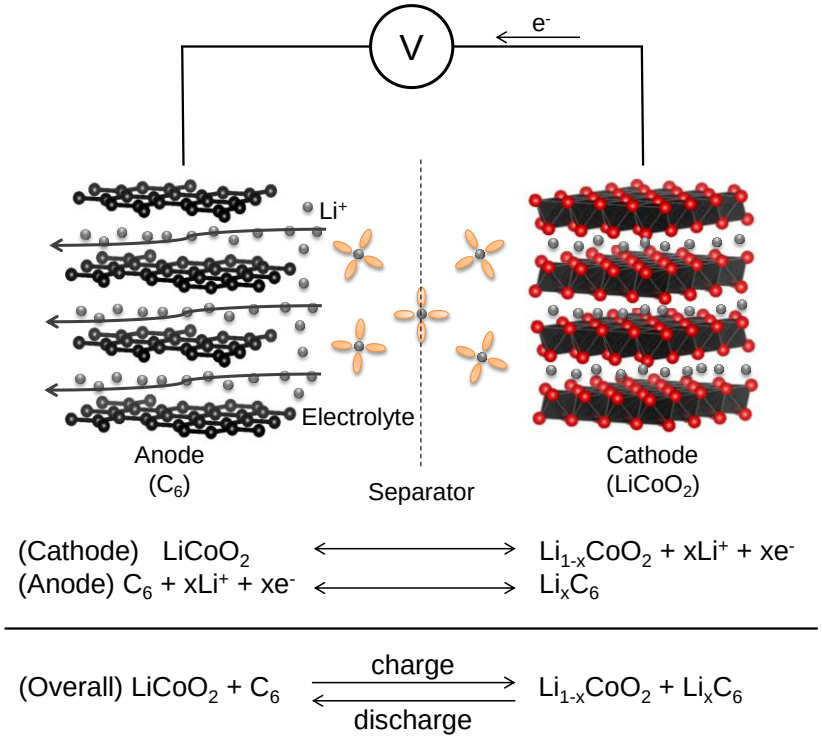

Figure 1.2 Schematic illustration of discharge process in Li-ion batteries. Chemical formula indicates chemical reactions between the cathode ($LiCoO_2$) and anode (graphite) during charge/discharge process.

Alternatively, electrical double-layer (EDL) capacitors have widely explored using materials with large specific surface area (*e.g.*, activated carbon). EDL is formed at the interface between electrode surface and adjacent electrolyte for neutralizing the charged electrode surface as shown in **Figure 1.3**. EDL is commonly divided to three regions[17,18]:

1. Inner Helmholtz plane: it comprises the absorbed solvent molecules and sometimes peculiarly absorbed ions on electrode surface due to chemical interactions.
2. Outer Helmholtz plane: counter-ions (charged opposite to the negatively or positively charged electrode surface) are closely packed by the electrostatic force.
3. Diffuse layer: it contains free ions (excess solvated cation and anions), which can be affected by the electrostatic force of the negatively or positively charged electrode surface.

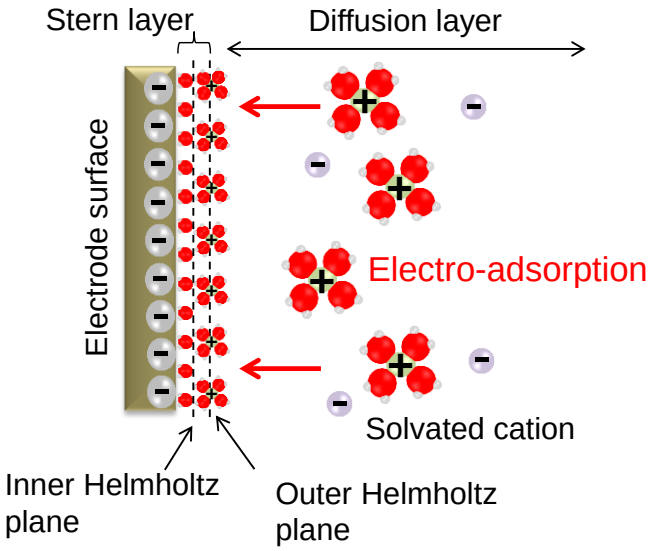

Figure 1.3 Schematic illustration of EDL formation during charge process. Solvated cations are electrochemically absorbed on the electrode surface.

EDL capacitance is generated at the interface between electrode surface and electrolyte. The first layer is formed with negatively (or positively) charged electrode surface and sometimes peculiarly absorbed ions on electrode surface due to chemical interactions. The second layer comprises counter-ions charged opposite to electrode surface. Generally, solvent molecules absorbed on electrode surface block the chemical interactions between electrode and solvated cations, which feature a dielectric of typical capacitors with the mechanism of electrochemical adsorption and desorption. Activated carbon has widely been used as an electrode for commercial EDL capacitors.[19,20] Although it provides fast charge/discharge capabilities, its capacitance is limited by specific surface area accessible to an electrolyte.[21,22]

Pseudocapacitors involve a faradaic charge-transfer reaction between electrode surface and electrolyte, unlike EDL capacitors in which charge storage occurs with an electrostatically adsorption through EDL formation. Pseudocapacitance materials have several types of reversible faradaic reaction mechanism: (1) underpotential deposition (UPD), (2) surface redox pseudocapacitance, and (3) intercalation pseudocapacitance. Underpotential deposition is a phenomenon that metal ions are electrochemically reduced on the substrate, generating an adsorbed monolayer of metal. As for surface redox pseudocapacitance, electrochemical adsorption of ions occurs with fast reversible faradaic redox reaction on electrode surface as shown in **Figure 1.4**.[23,24] Intercalation pseudocapacitance (*e.g.*, Nb_2O_5) involves the faradaic reaction in the bulk of the electrode materials.

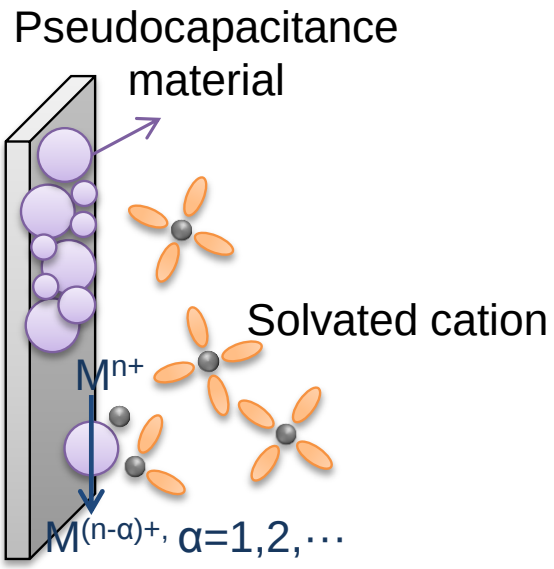

Figure 1.4 Schematic illustration of surface redox pseudocapacitance. Generally, oxidation state of transition-metal is changed by redox reaction between electrode and electrolyte.

Typically, redox pseudocapacitance provides even multiple redox couples, leading to the large capacitances. Transition-metal oxides and conducting polymers have been widely explored as pseudocapacitance electrode materials.[25-27] In particular, RuO_2-based materials[28] have the most studied due to their higher capacitance than commercial activated carbon and better electrochemical stability than conducting polymers. Since the discovery of the considerably enhanced capacitance of hydrous ruthenium oxide ($RuO_2 \cdot nH_2O$) with an amorphous phase (much larger than that of RuO_2), many studies have been focused on exploring the further high-performance of RuO_2-based materials and interpreting the material structure and electrochemical behavior.[29-31]

Although hydrous ruthenium oxide ($RuO_2 \cdot nH_2O$) as shown in **Figure 1.5b** gives capacitance ranges from 600 to 800 F/g much higher than that of anhydrous RuO_2 (**Figure 1.5a**), it has low electric conductivity, leading to low power density. W. Sugimoto *et al.* reported that a new layered ruthenic acid ($H_{0.2}RuO_{2.1} \cdot nH_2O$) as shown in **Figure 1.5c**, which provides high energy density (up to 390 F/g) as well as high power density.[32,33]

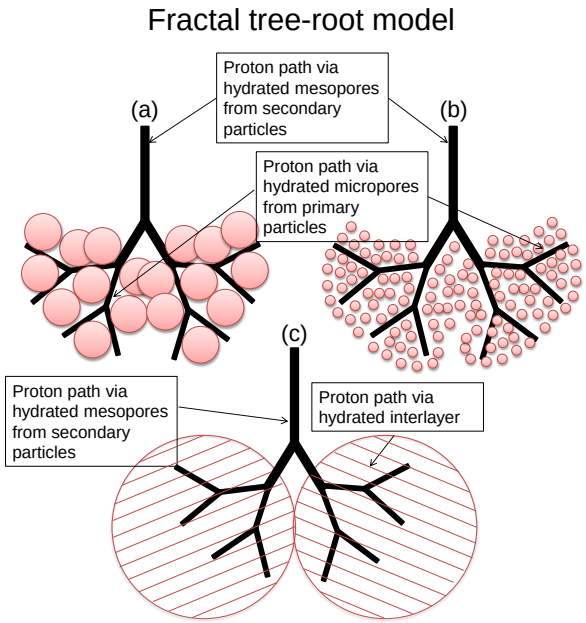

Figure 1.5 Schematic illustration of fractal tree-root model of (a) anhydrous RuO_2, (b) hydrous $RuO_2 \cdot nH_2O$, and (c) layered ruthenic acid ($H_{0.2}RuO_{2.1} \cdot nH_2O$) to understand the relationship between material structures and electrochemical performances.[33]

A fractal tree-root model (**Figure 1.5**) is employed to explain the relationship between material structures and electrochemical properties.[33] In this model, secondary particles are made by agglomeration of primary particles. Mesopores are formed between secondary particles, which can be described as the thick trunk root. The micropores between the primary particles can also be considered as the thin roots. Ionic conductivity increases with increased pore size due to low ionic resistance. Commonly, $RuO_2 \cdot nH_2O$ has the loosely-packed and 2 nm-scale primary particles, providing hydrated micropores (**Figure 1.5b**). On the other hand, anhydrous RuO_2 has the closely-packed 10-20 nm-scale primary particles, mostly forming mesopores (**Figure 1.5a**). $H_{0.2}RuO_{2.1} \cdot nH_2O$ has layered lamellar structure where proton-conducting hydrous layers (nH_2O) are interleaved between nano-sheets ($H_{0.2}RuO_{2.1}$) with high electrical conductivity. This structure with proton-conductive interlayer spacing (**Figure 1.5c**) offers intercalation psudocapacitance, which can utilize large amounts of active sites for charge storage, leading to high energy density (up to 390 F/g) without sacrificing power density. Mesopores are formed between secondary particles made by

stacking the layers. Large interlayer distance corresponds to the mesopores with low ionic resistance, and large planar interlayer spacing contributes to high energy density. Therefore, anhydrous RuO_2 provide high proton conductivity via hydrated mesopores from secondary particles while less amount of active sites for charge storage, leading to low energy density. Hydrous $RuO_2 \cdot nH_2O$ provides large amount of active sites for charge storage via hydrated micropores while it has poor electric conductivity and proton conductivity due to water content and high ionic resistance in the hydrated micropores, respectively. Layered ruthenic acid ($H_{0.2}RuO_{2.1} \cdot nH_2O$) has large interlayer spacing and distance, providing large amounts of active sites for charge storage as well as good electric conductivity and proton conductivity. However, critical drawback of ruthenium-based materials is very expensive because ruthenium is noble metal.

Two-dimensional (2D) materials (*e.g.*, graphene, MXene) similar to the structure of the layered ruthenic acid have been considered as promising candidates to enhance both energy and power densities for energy storage applications because they exhibit unique properties (*e.g.*, high electrical conductivity, low diffusion energy barrier) with large amounts of electrochemically-active sites.[34-36]

1.1 Two-dimensional materials

To enhance the ion accessibility between electrode surface and electrolyte, many dimensional types of materials have been reported such as nanoparticles (0D), nanotubes (1D), nano-sheets (2D), and mesoporous structures (3D).[37-39] These materials provide a large specific surface area and rapid charge transport, which are radically required for the high-performances of energy storage and conversion applications (*e.g.*, Li-ion rechargeable batteries, supercapacitors). As shown in **Figure 1.6**, different dimensional carbon-based nanomaterials (Fullerenes (0D), carbon nanotube (1D), graphene (2D), activated carbon and graphite (3D))[40] have widely been explored for improving the electrochemical performances of energy storage systems. For examples, Fullerenes (0D) have been used as coating agents for electrode materials with low stability in electrode/electrolyte interface, which offer the stable cycle ability.[41] Carbon nanotubes (CNTs) have 1D tubular structure with high electrical conductivity and large surface area, which make them to be served as the EDL charge storage host and conductive additives.[42,43] 3D activated carbon has been served as a super-capacitive material owing to its large specific surface area and hence they provide fast surface EDL capacitance and relatively higher energy density than conventional electrolytic capacitors.[44] In 2004, two-dimensional (2D) graphene was first discovered by the isolation from the three-dimensional (3D) graphite for the first time.[45] Graphene is crystalline carbon allotrope with an atomic-scale honeycomb lattice, which is composed of carbon atoms placed in a hexagonal structure. Each carbon

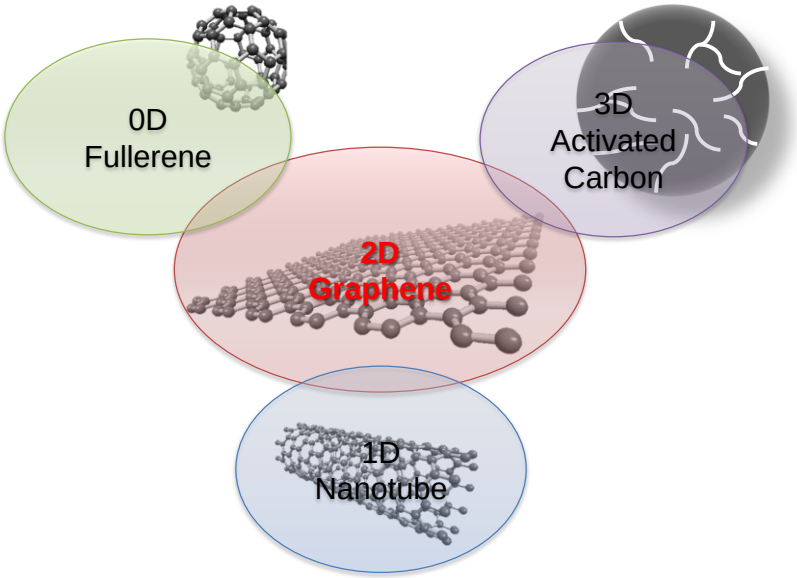

Figure 1.6 Schematic design of carbon-based materials in different dimensions: *i.e.*, 0D-fullerene, 1D-nanotube, 2D-graphene, and 3D-activated carbon

atom is connected each other with σ-bonds and delocalized π-bonds in the sp^2 honeycomb lattice.[46] Thanks to the 2D geometry and electronic structure of graphene, which takes advantages of good chemical stability, high electrical conductivity and excellent ion accessibility leading to a broad range of applications.[47] Since the discovery of graphene, numerous 2D materials such as hexagonal boron nitrides (*h*-BN),[48,49] transition-metal dichalcogenides (TMDCs),[50-52] metal oxides[53], hydroxides[54], MXenes, *etc.* have been explored as shown in **Figure 1.7** and **Table 1.1**.[55] The unique properties of 2D materials originated by their single layers, bulks, and layered counterparts promote to explore many types of 2D materials for a broad range of applications. 2D materials possess excellent properties such as high thermal and electrical conductivity, high mechanical strength, high mobility, high sensitivity, insulator behavior, *etc.*, which can be applied for energy storage, catalysts, water purifications, filters, semiconductors, and sensors.[56] In addition, 2D materials have versatile chemistry achieved by heterostructure, composite, doping, *etc.* which can provide new properties such as metallic character, semi-conductor, and insulator by controlling electronic structures. Since a variety of compositions can also offer favorable properties, novel 2D materials have been explored to synthesize: *e.g.*, MXene,[57] silicene,[58] germanene,[59] stanene,[60] and plumbene[61] were discovered in 2011, 2012, 2014, 2015, and 2019, respectively.

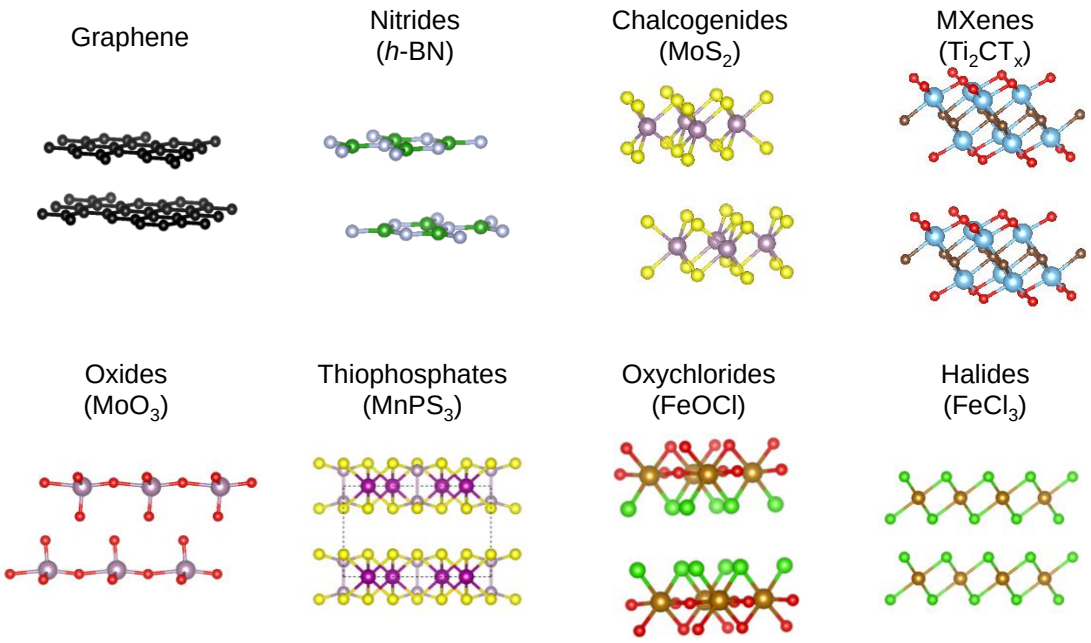

Figure 1.7 Examples of 2D layered materials.[55]

Table 1.1 Existent or potential 2D layered materials, which can provide unique properties for many applications.[55]

Group IV/V	**Dichalcogenides**	**Trichalcogenides**	**Oxides**	**Halides**	**Potential 2D Zintl Hosts**
Graphene C	VSe_2, $NbSe_2$,	Bi_2Se_3, Bi_2Te_3,	MoO_3, V_2O_5,	$FeCl_3$, $FeBr_3$,	
Graphane CH	TiS_2, ZrS_2, HfS_2,	Sb_2Te_3, Bi_2S_3,	WO_3, …	$CrCl_3$, $CrBr_3$,	$CaSi_2$,
Fluorographene CF	ReS_2, PtS_2,	In_2Se_3, As_2S_3,		$MoCl_3$, $MoBr_3$,	$CaGe_2$,
Silicene Si	$TiSe_2$, $ZrSe_2$,	As_2Se_3, $NbSe_3$,	**Nitrides**	$TiCl_3$, $TiBr_3$,	$Ca(Si_{1-x}Ge_x)_2$,
Germanane GeH	$HfSe_2$, $ReSe_2$,	TiS_3, ZrS_3, $ZrSe_3$,	*h*-BN	$InBr_3$, PbI_2,	$Ba_3Sn_4As_6$
	$PtSe_2$, $SnSe_2$,	$ZrTe_3$, HfS_3,		$AlCl_3$, $InBr_3$,	$CaMg_2N_2$
MXenes	$TiTe_2$, $MoTe_2$,	$HfSe_3$, $HfTe_3$,	**Oxychlorides**	$CrBr_3$, $FeCl_2$,	$CaIn_2$
$Ti_3C_2T_x$, Ti_2CT_x,	WTe_2, $CoTe_2$,	NbS_3, TaS_3,	BiOCl, FeOCl,	$MgCl_2$, $CoCl_2$,	$CaNi_2P_2$
Nb_2CT_x, Mo_2CT_x, …	$RhTe_2$, $IrTe_2$,	$TaSe_3$, …	HoOCl, ErOCl,	VCl_2, VBr_2,	CaAuGa, …
	$NiTe_2$, $PdTe_2$,		ErOCl, TmOCl,	VI_2, $CdCl_2$,	
	$PtTe_2$, $SiTe_2$,	**Mono-Chalcogenides**	YbOCl, LnOCl,	CdI_2, …	
	NbS_2, TaS_2,		…		
	MoS_2, WS_2,	GeSe, GeTe,	**Layered Silcate Minerals**	**Thiophosphates**	
	$TaSe_2$, $MoSe_2$,	GaSe, GaS		$FePS_3$, $MnPS_3$,	
	WSe_2, $MoTe_2$,		Egyptian Blue,	$NiPS_3$, …	
	$SnSe_2$, SnS_2, …		…		

2D materials have been considered as promising energy storage hosts because unique 2D layered structures offer many benefits such as rapid transportation of ions and electrons compared to complex 3D structures, and large amounts of active sites for charge storage as shown in **Figure 1.8**.[34] Indeed, many 3D electrode structures such as the spinel structure exhibit geometrically intrinsic problems (*e.g.*, high diffusion energy barrier in the electrode), leading to poor rate capabilities. To improve the performance such as energy density, power density, and cycling ability for batteries and supercapacitors, 2D structures may effectively be used for good charge storage hosts with fast charge transportation.

Energy density of 2D materials is determined by how much the amounts of charge can be accommodated in their interlayer spacing. 2D materials have a face to face planar structure, providing large amounts of electrochemically-active sites for charge storage. This large lateral size of the 2D materials can store large amounts of ions in interlayer spacing in parallel to charge storage on the surface, which can deliver higher energy density comparable to batteries.[62] In addition, 2D structures with large interlayer distance provide excellent ion accessibility and fast diffusion pathway in interlayers, resulting in high power density.

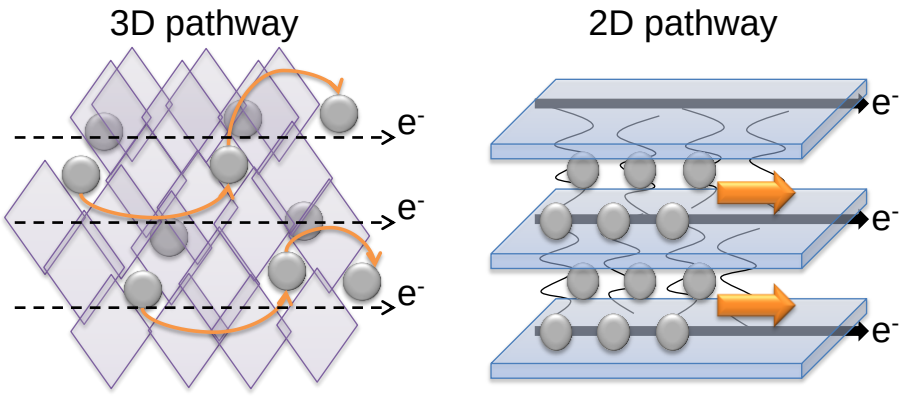

Figure 1.8 Schematic design for 3D and 2D pathway of ions and electrons.

Moreover, versatile chemistry[63,64] (*e.g.*, attachment of surface termination groups, insertion of intercalants as a pillar) of 2D materials grants new properties for the high-performances; for example, increased interlayer distance gives excellent ion accessibility with a low energy barrier of ion-transportation in the interlayer. Also, metallic and zero-band gap 2D materials with high electrical conductivity can be achieved by tuning of electronic structures.[65,66] Rich chemistry of 2D materials opens a new door for the synthesis of new materials, which can make them have favorable properties for energy storage applications.[67-69]

Figure 1.9 shows a schematic illustration of an ideal 2D supercapacitor with intercalation capacitance in the interlayers of 2D materials. During discharge process, solvated-ions in a 2D anode material transport to a 2D cathode material through an electrolyte while electrical current flows as the electrons move to cathode electrode. On the other hand, solvated-ions and electrons move backward during charge process. Owing to large interlayer distance and spacing, 2D materials provide fast charge transportation and large capacitance, which can be considered as alternatives to electrode materials for Li-ion batteries. Indeed, there have been many reported 2D materials for energy storage applications. Graphene has been the most studied due to their advantages of high electrical conductivity and large specific surface area.[70] In addition, many other types of 2D-based materials such as TMDCs, metal oxides, metal hydroxides, MXenes *etc.* have been used as active electrode materials for energy storage applications as listed in **Table 1.2**.

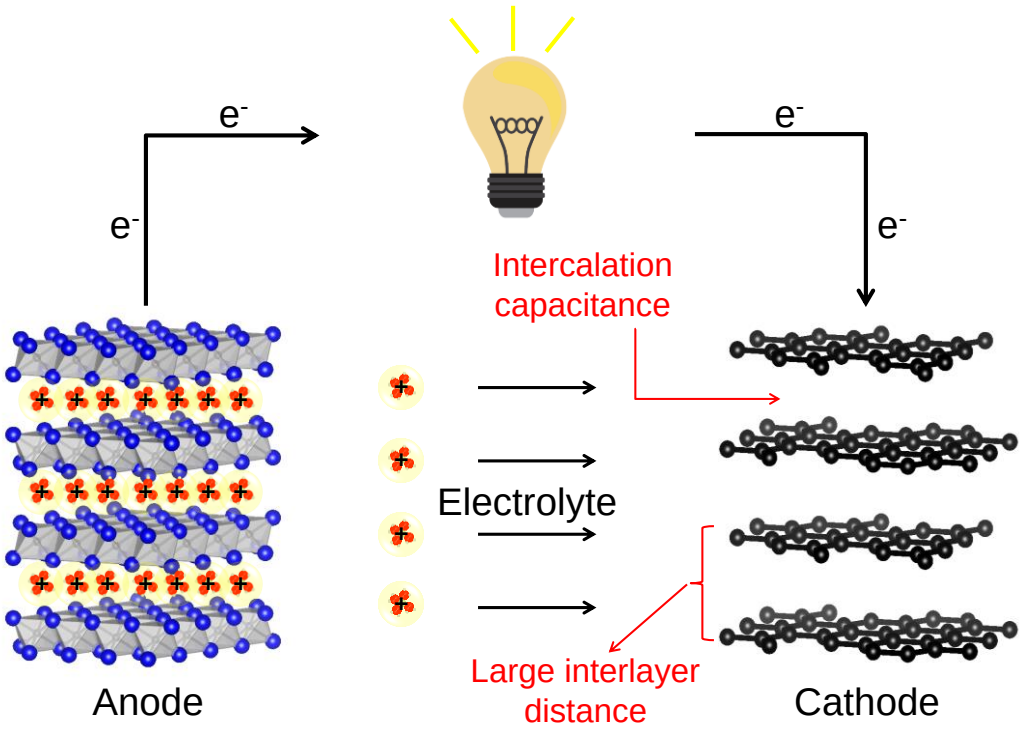

Figure 1.9 Schematic example of supercapacitor using 2D anode and cathode, which enable solvated-ion intercalation and deintercalation. During discharge process, solvated-ions move to cathode material and intercalate into interlayer while electrons transport to cathode side along to an electrical circuit. Conversely, solvated-ions and electrons move back to anode material during charge process. 2D supercapacitor system is considered as a promising candidate for future energy storage device due to relatively high capacitance and fast solvated-ion transportation. Solvated-ion intercalation without the desolvation facilitates fast charge/discharge in the absence of high desolvation energy barrier, typically featured in commercial Li-ion batteries.

Table 1.2 Various 2D materials for energy storage applications.

Material	**Description**	**Ref.**
Graphene sheet	Highly corrugated graphene sheets (HCGS) showed capacitance of 349 F/g in aqueous electrolyte.	71
MnO_2/chemically modified graphene	Capacitance of 389 F/g at a current rate of 1 A/g and superior capacitance retention of 97.7 % at a current rate of 35 A/g in aqueous electrolyte.	72
Graphene	Capacitance of 117 F/g in aqueous electrolyte.	73
Graphene oxide hydrogel	Graphene oxide hydrogel provided capacitance of 232 F/g in aqueous electrolyte.	74
Exfoliated graphene	Exfoliated Graphene exhibited capacitance of 120 F/g in organic electrolyte.	75
MoS_2/rGO	High concentrations of MoS_2 with RGO ($HCMoS_2$/RGO) showed capacitance of 148 F/g in aqueous electrolyte.	76
Fe_3O_4/rGO	Fe_3O_4@RGO nanocomposites exhibited superior capacitance (326 F/g) in aqueous electrolyte.	77
Boron-doped graphene	Boron-doped graphene showed 172.5 F/g at a current rate of 0.5 A/g in aqueous electrolyte.	78
200-μm MXene film	200-μm MXene film exhibited exceeding 200 F/g at a high scan rate of 2 V/s in aqueous electrolyte.	79

1.2 MXenes

MXenes are an emerging class of two-dimensional (2D) transition-metal carbides and nitrides. In 2011, M. Naguib *et al.*[57] have first discovered 2D graphene-like MXene obtained by the extraction of Al layers in a MAX phase Ti_3AlC_2 in hydrofluoric acid solution. MAX phases are ternary layered carbides and nitrides with general formula of $M_{n+1}AX_n$; *n*: 1, 2, or 3, M: early transition-metals, A: mostly 13A and 14A groups, X: C and/or N. More than 60 different members of pure MAX phases have been found as shown in **Figure 1.10**.[80-84] However, different combinations of M and X atoms could quite enlarge the number of MAX phases, which can make their intrinsic properties adjustable. All reported MAX phases have layered hexagonal structures with space group of $P6_3/mmc$ in which the $M_{n+1}X_n$ layers (the X atoms are filled in octahedral sites between the nearly close-packed M layers) are interleaved by the A layers.[85-89]

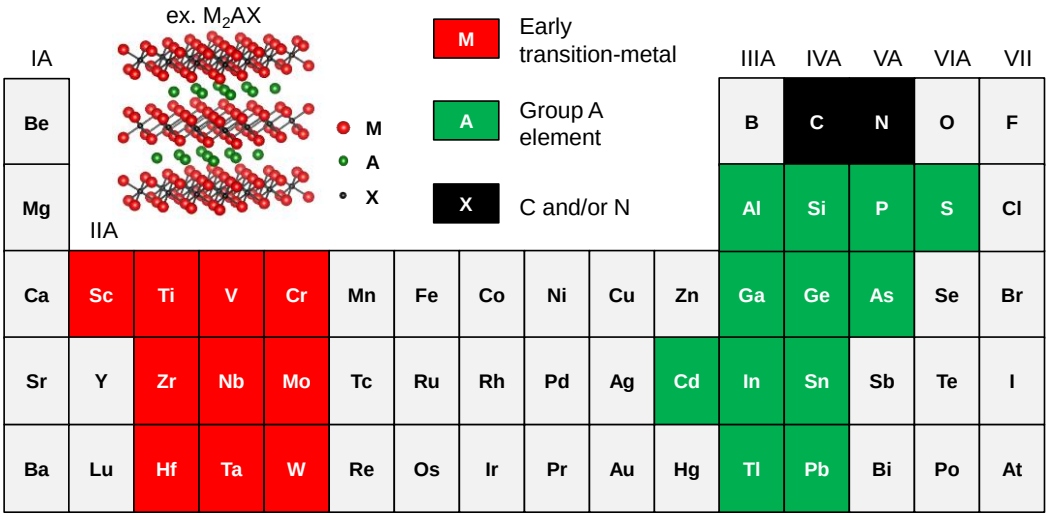

Figure 1.10 Reported MAX phases $M_{n+1}AX_n$ (*n*: 1, 2, or 3) in periodic table. Schematic chemical structure shows an example of MAX phase of M_2AX (hexagonal layered structure, $P6_3/mmc$).

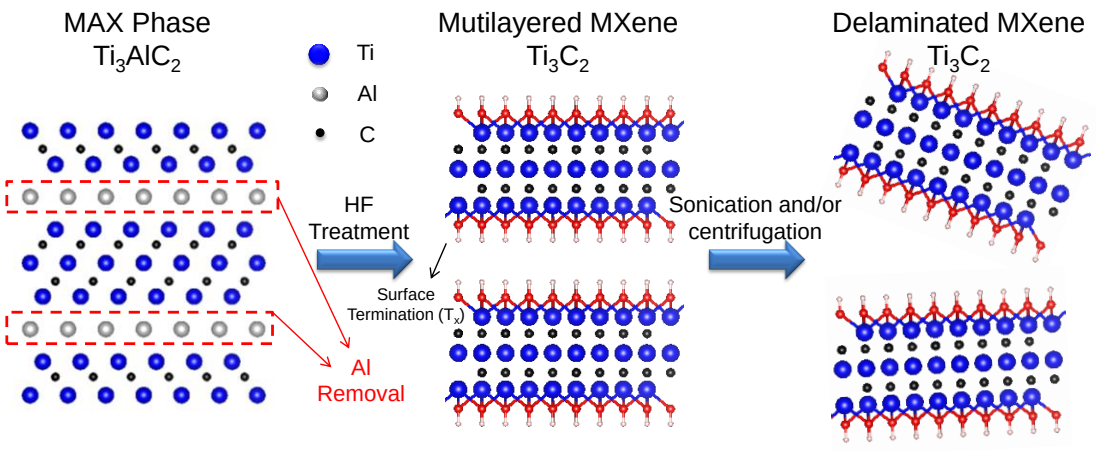

Figure 1.11 Schematic design of etching process of Al layers from Ti_2AlC to MXene $Ti_3C_2T_x$ (T_x: surface termination groups from etchant).

The $M_{n+1}X_n$ layers are chemically stable with a mixed covalent/metallic/ionic bonding stronger than a metallic bonding between M and A atom. Therefore, the A layers can be selectively extracted by an appropriate chemical treatment. A multilayered MXene $Ti_3C_2T_x$ (T_x: termination group from the etchant) have successfully been synthesized by the selective removal of Al layers from a MAX phase Ti_3AlC_2 in HF acid solution as described in **Figure 1.11**. Considering the etchant compounds of a HF aqueous solution, selectively etching process resulting in formation of $Ti_3C_2T_x$ (T_x: -OH, -O, -F) possibly occurs (**Equation 1.1-1.4**).[57, 90-92] Furthermore, delaminated 2D MXene (same structure with graphene) can be synthesized by sonication and centrifugation of the multilayered MXene $Ti_3C_2T_x$ due to weak van der Waals force between the layers as shown in **Figure 1.11**.[57]

(Equation 1.1) $Ti_3AlC_2 + 3HF = AlF_3 + 3/2H_2 + Ti_3C_2$

(Equation 1.2) $Ti_3C_2 + 2H_2O = Ti_3C_2(OH)_2 + H_2$

(Equation 1.3) $Ti_3C_2(OH)_2 = Ti_3C_2O + H_2O$

(Equation 1.4) $Ti_3C_2 + 2HF = Ti_3C_2F_2 + H_2$

As for etching process, the metallic bond of Ti-Al from Ti_3AlC_2 is weakened by the strong etchant of HF, leading to the formation of Ti_3C_2 as shown in **Equation 1.1**. Termination group (-OH, -O, -F) as described in **Equations 1.2-1.4** could be attached to Ti atoms confirmed by energy-dispersive X-ray (EDX) analysis.[57] MXenes can be also synthesized by the removal of A layers in a LiF/HCl aqueous solution. LiF/HCl treatment is so-called *in situ* HF formation method because HF is generated by reaction between LiF and HCl as a following **Equation 1.5**.[93]

As HF is an extremely dangerous chemical, LiF/HCl (*in situ* HF) treatment has widely been employed for etching process. In addition, this treatment takes several advantages by attachment of chloride termination groups as a following **Equation 1.6** and large lateral size of MXenes.[93,94]

(Equation 1.5) $LiF + HCl = HF + LiCl$

(Equation 1.6) $Ti_3C_2 + 2HCl = Ti_3C_2Cl_2 + H_2$

In LiF/HCl treatment, larger size of the chloride atom (1.75 Å) compared to that of fluoride atom (1.47 Å) provide enlarged interlayer distance of Ti_2CT_x (8.7 Å). Indeed, this value is larger than that of HF treatment of Ti_2CT_x (7.7 Å), providing higher capacitance of 300 F/g (Ti_2CT_x (LiF/HCl)) than 240 F/g (Ti_2CT_x (HF)) owing to superior ion accessibility in MXene interlayer in a non-aqueous electrolyte.[95] Moreover, LiF/HCl treatment was much milder than HF treatment, providing larger lateral flakes with low probability of nano-size defects, usually detected in HF-treated MXene materials. LiF/HCl treatment also takes advantages of high yields of MXene and high electrical conductivity (~1500 S/cm) achieved by non-defected, large lateral structure.[93]

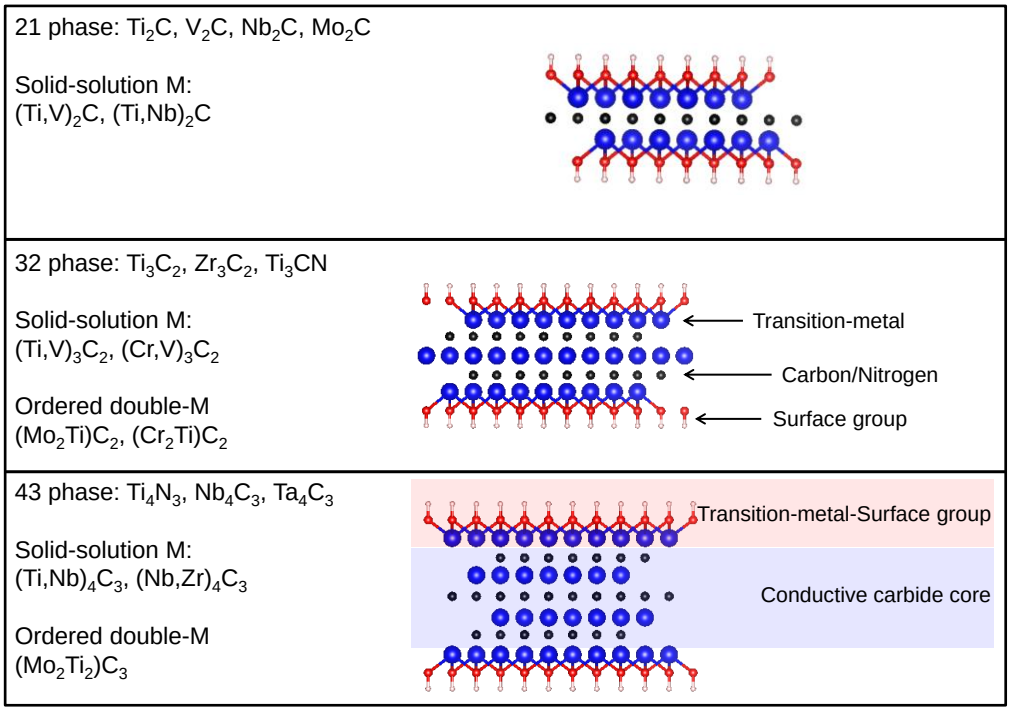

Figure 1.12 Reported MXene $M_{n+1}X_nT_x$ (M: transition-metal, X: carbon and/or nitrogen, *n*: 1, 2, or 3).

As shown in **Figure 1.12**,[96] MXenes ($M_{n+1}X_nT_x$, *n*: 1, 2, or 3) can be synthesized with different phases; M_2XT_x (21 phase), $M_3X_2T_x$ (32 phase), and $M_4X_3T_x$ (43 phase). They also have different

forms; ordered single-M (*e.g.*, Ti_2C, Ti_3C_2), a solid solution of transition-metal (*e.g.*, $(Ti,V)_2C$), ordered double-M (*e.g.*, $(Mo_2Ti)C_2$), and a solid solution of carbon and nitrogen (carbonitrides). Because a variety of MXenes have different chemical, physical properties, they might be promising candidates for appropriate applications.

In summary, MXenes are a new class of two-dimensional transition-metal carbides, carbonitrides, and nitrides. Their general formula is $M_{n+1}X_nT_x$; *n*: 1, 2, or 3, M: Ti, Nb, Mo, V, *etc.*, X: C and/or N, T_x (surface termination group from etchants): -OH, -O, -F, -Cl. Approximately 20 different MXenes have been successfully synthesized and characterized. Besides extant MXenes, the properties of new MXenes have also been computationally characterized and they have been challenged to synthesize. Exploration of new MXenes (*e.g.*, different M atoms, solid solution of M atoms, combination of C and N atoms, different surface termination groups) provides a great potential for tuning the properties.[97-99] Recently, many researchers have studied a variety of MXenes, which have been employed not only in energy storage applications but also in many field such as composites for strong mechanical strength, water purification, electro-catalyst for oxygen and hydrogen evolution, sensors, *etc.* (**Table 1.3**).

Table 1.3 MXenes for various applications other than energy storage.

Application	**Material**	**Description**	**Ref.**
Structural composite	$Ti_3C_2T_x$-PVA $Ti_3C_2T_x$-PDDA	Enhanced mechanical strength, hardness, and anti-friction properties.	100
Water purification	$Ti_3C_2(OH)_2$	Heavy metal filtration (*e.g.*, Pb).	101
Ion sieving	$Ti_3C_2T_x$	Membrane for filtering NaCl, $MgSO_4$, *etc.*	102
Oxygen evolution	$Ti_3C_2T_x$/graphitic C_3N_4	Freestanding oxygen electrode for rechargeable Zn-air batteries.	103
Hydrogen evolution	Mo_2CT_x	Hydrogen evolution in sulfuric acid.	104
Gas sensor	V_2C-PDMAEMA	CO_2 and temperature sensor.	105
Antibacterial material	$Ti_3C_2T_x$	98% bacterial cell viability loss.	106

1.3 Energy storage applications of MXenes

The chemical and structural versatility of 2D MXenes offers favorable properties such as high electrical conductivity and large interlayer distance providing excellent ion accessibility and large amounts of electrically-active sites. These features could lead to high energy and power density for energy storage applications.[96] M. R. Lukatskaya, *et al.*[107] reported intercalation of various ions (Li^+, Na^+, K^+, NH_4^+, Mg^{2+}, Al^{3+}) in $Ti_3C_2T_x$ MXene interlayers, opening the door of new 2D MXene electrodes for batteries and supercapacitors. Although $Ti_3C_2T_x$ was reported to have much lower surface area of 23 m^2/g than 2500 m^2/g of activated carbon, the capacitance of $Ti_3C_2T_x$ (80 F/g) is comparable with 100 F/g of activated carbon in Li_2SO_4 aqueous system, suggesting that different charge storage mechanism occurs other than surface EDL capacitance.[107] Because MXenes have large interlayer distance (> 10 Å), solvated-ions might be intercalated into MXene interlayer. Indeed, reversible shifts of 002 diffraction peak were observed during charge/discharge process, indicating expansion (charge) and shrinkage (discharge) of interlayer distance based on *ex situ* XRD.[108] Therefore, charge storage mechanism of MXenes generated by surface EDL capacitance on exfoliated surface and intercalation EDL capacitance in MXene interlayers could give large capacitance, despite such low specific surface area of 23 m^2/g as shown in **Figure 1.13**.[107,108]

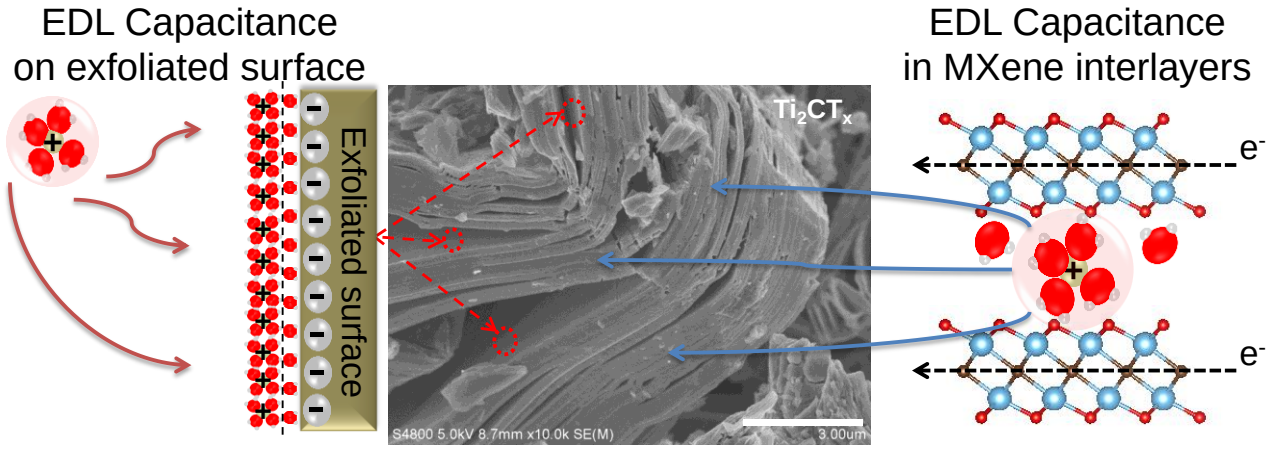

Figure 1.13 Scanning electron microscope (SEM) image of Ti_2CT_x. Solvated-ions can be not only electro-adsorbed on the exfoliated surface (surface EDL capacitance) but also intercalated in interlayers of MXenes (intercalation EDL capacitance) with aqueous system.

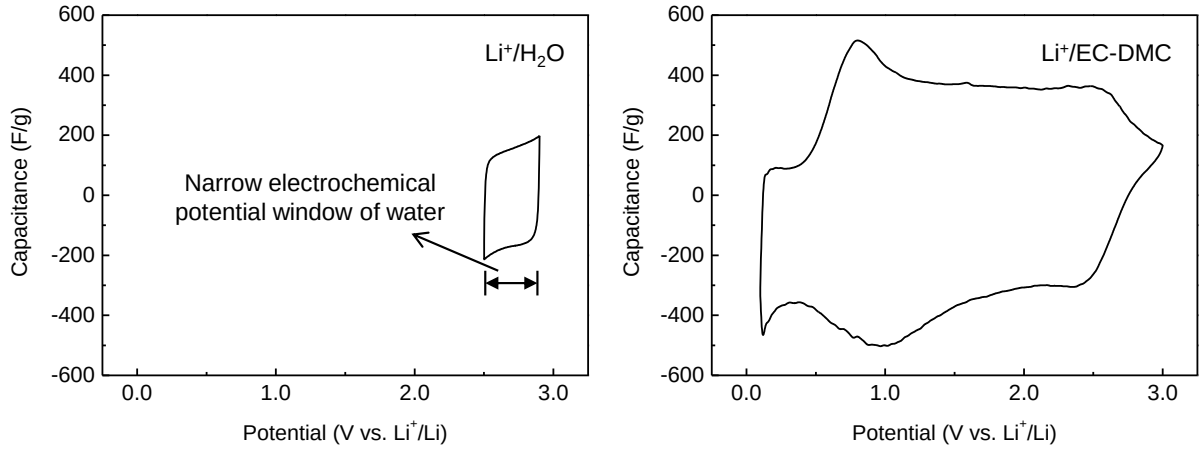

Figure 1.14 Cyclic voltammograms of LiF/HCl-treated Ti_2CT_x in a typical aqueous electrolyte 1 M Li_2SO_4 and a non-aqueous electrolyte 1 M $LiPF_6$ in EC/DMC (1/1, vol.%). Re-experimental data from ref. 108.

Figure 1.14 shows cyclic voltammograms (CV) of MXene Ti_2CT_x in aqueous and non-aqueous system. The CV in a commercial 1 M Li_2SO_4 aqueous electrolyte shows a rectangular shape, which is characteristic of a typical capacitor. In contrast, the CV in 1 M $LiPF_6$ in EC/DMC (1/1, vol.%) exhibits a distorted rectangular with larger capacitance, suggesting different charge storage mechanism with aqueous system.[108] The capacitance (163 F/g with a specific capacity of 20 mAh/g) of Ti_2CT_x with a 1 M Li_2SO_4 aqueous system[109] is much lower than that (320 F/g with a specific capacity of 250 mAh/g) with 1 M $LiPF_6$ in EC/DMC (1/1, vol.%).[95] In addition, M. Naguib *et al.* reported the high reversible capacities of 170 and 260 mAh/g for Nb_2CT_x and V_2CT_x with 1 M $LiPF_6$ in EC/DEC (1/1, wt.%).[110]

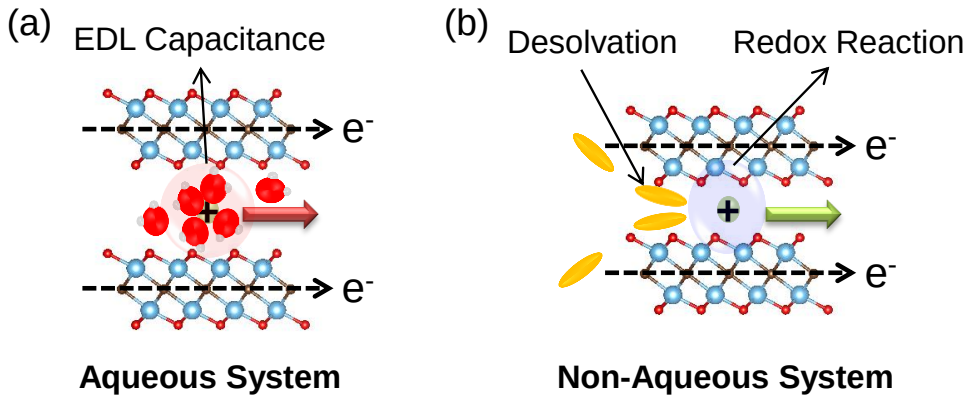

Figure 1.15 Schematic illustration of the different charge storage mechanisms in MXene interlayer with (a) aqueous and (b) non-aqueous electrolytes.

Here, M. Okubo, *et al.*[108] systematically investigated differences of charge storage mechanism in aqueous and non-aqueous systems as shown in **Figure 1.15**. Since cations in aqueous system

strongly coordinated with water molecules, hydrated-cations (*e.g.*, Li^+-$4H_2O$) can be intercalated in MXene interlayers without redox reaction between ions and surface terminations as shown in **Figure 1.15a**. Indeed, *ex situ* XRD of Ti_2CT_x with a Li_2SO_4 exhibited reversible shifts of 002 diffraction peak during charge/discharge process, indicating that hydrated-Li^+ are intercalated in MXene interlayers. As shown in **Figure 1.15b**, the cations in non-aqueous system are weakly coordinated with solvent molecules, resulting in an ease desolvation. Thus, orbitals of desolvated-cations can be hybridized with the orbitals of surface termination groups leading to redox reactions in MXene interlayer. These redox reactions cause the distorted CV in non-aqueous system (**Figure 1.14**), providing the higher capacitances than those of aqueous system.[108]

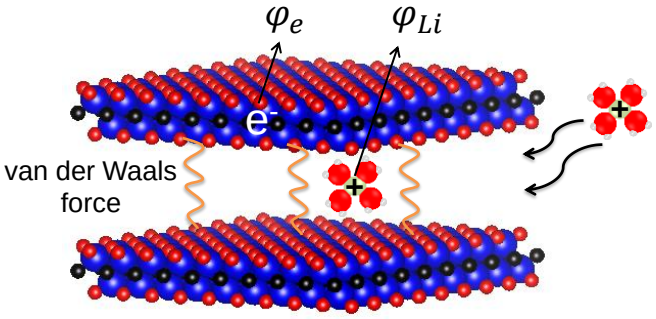

$$C = \frac{\Delta Q}{\Delta(\varphi_e - \varphi_{Li})}$$

C: specific capacitance
ΔQ: stored charge per electrode weight
$\Delta(\varphi_e - \varphi_{Li})$: change of inner potential difference between electron and lithium ion

Figure 1.16 Schematic illustration of solvated-ion intercalation in MXene interlayer with an equation of the specific capacitance (C) in aqueous system.

The specific capacitance (C) in MXene interlayers can be expressed as an equation in **Figure 1.16** in aqueous system. In aqueous system, ΔQ is small due to the narrow electrochemical potential window and hence $\Delta(\phi_e - \phi_{Li})$ is constant owing to no band-filling effect (ϕ_e is constant) and no chemical interaction of solvated-ions (ϕ_{Li} is constant). Thus, intercalation capacitance behaves like EDL capacitance with solvated-ions as shown in **Figure 1.3**, providing rectangular CV shape (**Figure 1.14**). Unlike the Li aqueous system, $Ti_3C_2T_x$ MXene in acidic aqueous electrolytes (*e.g.*, 1 M H_2SO_4) showed distorted CV shape, providing the faster charge/discharge capability and higher capacitance comparable to that of non-aqueous system.[79,111-113] In acidic atmosphere, M. Hu, *et al.*[114] demonstrated charge storage mechanism (faradaic reaction) that the change in transition-metal state is accompanied by fast protonation of oxygen surface termination group in MXene (*e.g.*, $Ti_3C_2T_x$) interlayers as a following **Equation 1.7**.[79]

(Equation 1.7) $Ti_3C_2O_a(OH)_bF_cCl_d + \delta e^- + \delta H^+ = Ti_3C_2O_{a-\delta}(OH)_{b+\delta}F_cCl_d$

Figure 1.17 shows schematic illustration of faradic reaction in the MXene interlayer. This rapid protonation of oxygen surface group in large lateral MXene interlayer gives faster charge/discharge capabilities and higher capacitances compared to those of other aqueous system (*e.g.*, Li, Na). In addition, designing MXene electrode architectures with enhanced ion accessibility to electrochemically active sites can further improve their electrochemical performances. Indeed, macroporous MXenes, MXene hydrogels, and MXene thin-film in the acidic electrolyte delivered high capacitances of exceeding 300 F/g below scan rate of 1 V/s and exceeding 200 F/g at 10 V/s.[79]

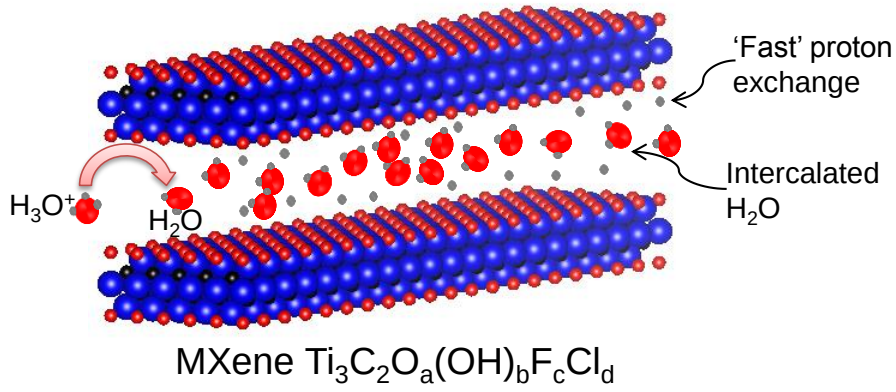

Figure 1.17 Schematic illustration of charge storage mechanism in MXene interlayer with acidic aqueous electrolyte.

Owing to favorable properties (*e.g.*, intercalation capacitance, high electric conductivity) of MXenes, many studies on MXenes have been conducted as electrode materials for supercapacitors. Furthermore, the versatile chemistry and chemical composition change of MXene provide the synthesis of new MXenes, which feature excellent electrical conductivity, superior ion accessibility, and large space of electrochemically active sites. First way to enhance electrochemical performances of MXenes is to tune the surface termination groups. S. Kajiyama *et al.*[95] reported enhanced ion accessibility in MXene interlayer by the substitution of surface groups from -O, -OH, -F (HF aqueous solution etching) to -O, -OH, -F, -Cl (LiF/HCl aqueous solution etching) due to increased interlayer distance coming from larger chloride atomic size as shown in **Figure 1.18**. Ti_2CT_x (LiF/HCl) showed the higher gravimetric and volumetric capacitance of 300 F/g and 130 F/cm^3 than 240 F/g and 100 F/cm^3 of Ti_2CT_x (HF) with 1 M $LiPF_6$ in EC/DMC (1/1 vol.%). Furthermore, Li-ion hybrid capacitor with Ti_2CT_x (LiF/HCl) and $LiNi_{1/3}Co_{1/3}Mn_{1/3}O_2$ provided an high energy density of 160 Wh/kg at 220 W/kg in 1 M $LiPF_6$ in EC/DMC (1/1 vol.%), which is comparable with those of commercial Li-ion batteries. This work suggested that larger surface termination groups (*e.g.*, -Br and –I) may further enhance electrochemical performances of MXenes.

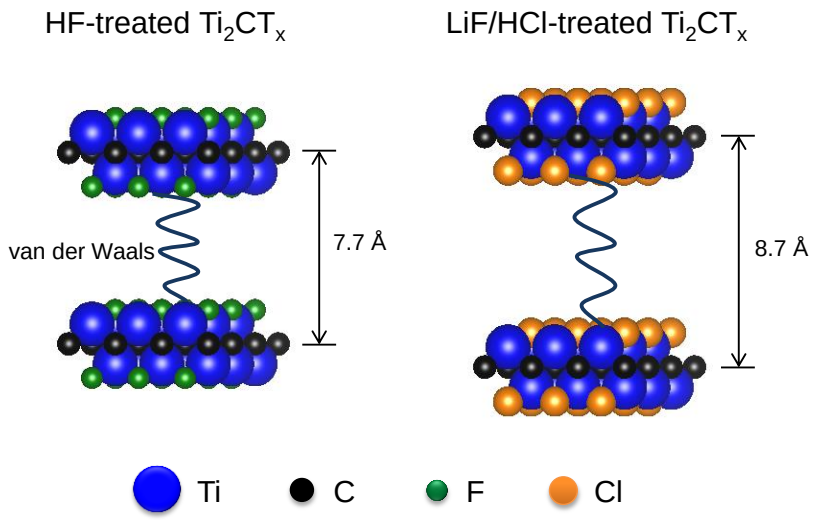

Figure 1.18 Schematic design for different interlayer distances of HF-treated Ti_2CT_x and LiF/HCl-treated Ti_2CT_x. Larger chloride atomic size provides increased interlayer distance, which can enhance ion accessibility.

Second approach to improve electrochemical behavior is to employ pre-intercalation of large molecules. Pre-intercalation of large organic molecules (dimethyl sulfoxide, urea, hydrazine, long-chain alkylamines, *etc.*) offers large interlayer distances, which facilitate the ion transport in MXene interlayers. For examples, cetyltrimethylammonium bromide (CTAB) pre-intercalation[115] in $Ti_3C_2T_x$ opens magnesium storage capability for Mg-ion batteries while magnesium ions cannot intercalate without CTAB as shown in **Figure 1.19**. And also, hydrazine pre-intercalation in $Ti_3C_2T_x$ enhanced the capacitance of 250 F/g with excellent rate capability compared to 100 F/g of pristine $Ti_3C_2T_x$ in 1 M H_2SO_4 aqueous electrolyte.[116]

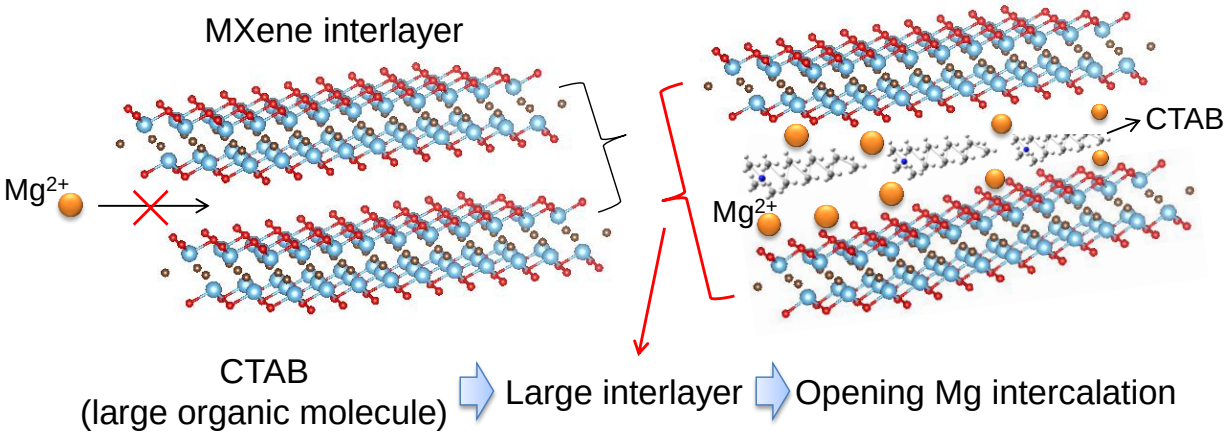

Figure 1.19 Schematic design for pristine MXene and CTAB-intercalated MXene interlayers. By virtue of increased interlayer distance of CTAB-intercalated MXene, it provides the pathway of Mg-ion intercalation.

Third way to increase energy and power densities is to synthesize delaminated-MXene films as a shown example of delamination process in **Figure 1.20**.[117-120] Because interlayers of MXenes are interacted with weak van der Waals force, MXenes can be easily delaminated by sonication (with/without intercalation of large organic molecule) and centrifugation, forming a colloidal MXene solution. After filtration of solutions of delaminated colloidal MXenes, a binder-free freestanding film can be obtained. Freestanding MXene films show high electrical conductivity, excellent ion accessibility, high packing density, and good flexibility, leading to high power density and large volumetric and gravimetric capacitances for flexible supercapacitors. MXene films have widely been studied for high-performance flexible supercapacitors; for an example, flexible MXene electrode shows high gravimetric capacitance of exceeding 300 F/g with excellent power density in a 2 M H_2SO_4 aqueous electrolyte.[79]

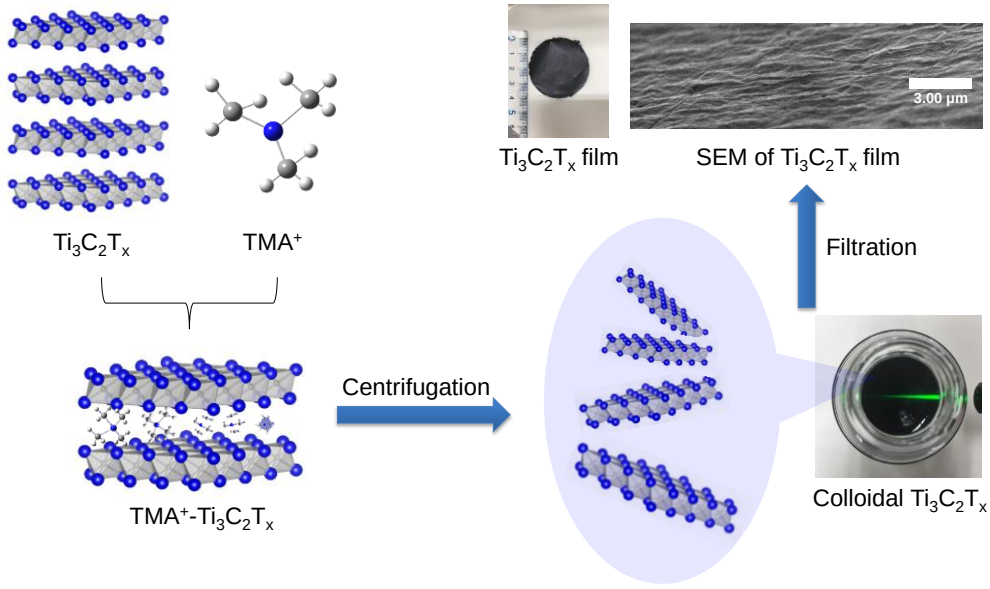

Figure 1.20 Schematic design for an example of delamination process of $Ti_3C_2T_x$ assisted by TMA^+ intercalation. Colloidal $Ti_3C_2T_x$ solution is obtained. After filtration, freestanding $Ti_3C_2T_x$ film is fabricated.

Other methods are to fabricate 2D heterostructures using MXene and other 2D materials (*e.g.*, graphene) and to make MXene composites with other compounds (*e.g.*, high capacitance materials with low electric conductivity) to produce synergy effects[121]; for examples, MXene/Si/SiO_x/C and MXene-supported Co_3O_4 quantum dots showed high lithium storage performance. In addition, MXene/graphene 2D heterostructure provides the fast charge/discharge capability and MXene/MoS_2 2D heterostructure gives high gravimetric capacitance.[122] In summary, a variety of combination of MXene, versatile chemistry of MXene, and MXene-based composites would be promising candidates for high-performance supercapacitors.

1.4 Purpose of this thesis

Energy storage devices are required to have eco-friendliness, cost-effectiveness, and excellent electrochemical performances for a variety of applications such as electric vehicles, renewable energy, and electronic devices. Aqueous supercapacitors have been considered as promising candidates owing to their fast charge/discharge capabilities, inexpensive price, and eco-friendliness. However, their energy densities have been confined by the narrow operating potential window of water (1.23 V). Herein, the author has concentrated on enhancing energy storage capabilities of aqueous supercapacitors with several strategies as illustrated in **Figure 1.21**; first is to use 2D transition-metal carbides (MXenes), which can provide high electric conductivity and high capacitance generated by surface EDL capacitance and intercalation EDL capacitance with large lateral size. Second is to employ a concentrated aqueous electrolyte called hydrate melt featuring wide electrochemical potential window (>3 V). Third is to challenge synthesis of novel 2D transition-metal borides (MBenes) for energy storage hosts with high electrochemical performances (*e.g.*, excellent electrical conductivity, superior charge storage capability) predicted by the first-principle calculation.[123]

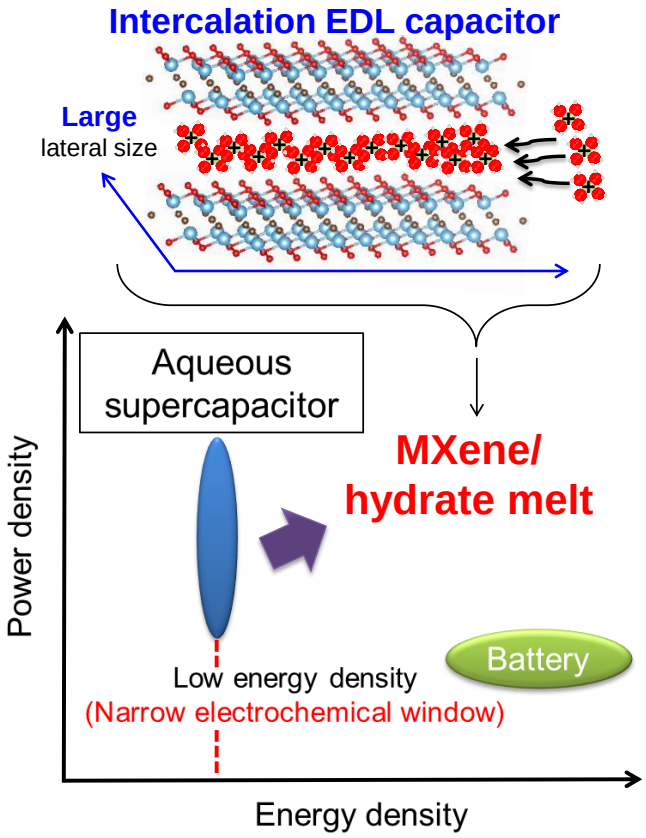

Figure 1.21 Target of high energy and power aqueous supercapacitor using 2D MXene electrodes and a concentrated electrolyte called hydrate melt.

The following is main topics covered in this thesis.

1. High energy and voltage MXene supercapacitor with a hydrate melt electrolyte.
2. Clarification of rate-determining step of ion transport on MXene electrodes in concentrated aqueous electrolytes.
3. Topochemical synthesis of phase-pure Mo_2AlB_2 through staging mechanism: A possible precursor for novel 2D transition-metal borides (MBenes).

Through systematic studies on 2D MXene/concentrated electrolyte systems and synthesis of potential 2D MBenes, their potential, problems and future perspectives will be handled in this thesis.

References

(1) Thackeray, M. M.; Wolverton, C.; Isaacs, E. D. Electrical Energy Storage for Transportation - Approaching the Limits of, and Going beyond, Lithium-Ion Batteries. *Energy Environ. Sci.* **2012**, *5*, 7854–7863.

(2) Scrosati, B.; Garche, J. Lithium Batteries: Status, Prospects and Future. *J. Power Sources* **2010**, *195*, 2419–2430.

(3) Ma, T.; Yang, H.; Lu, L. Development of Hybrid Battery-Supercapacitor Energy Storage for Remote Area Renewable Energy Systems. *Appl. Energy* **2015**, *153*, 56–62.

(4) Etxeberria, A.; Vechiu, I.; Baudoin, S.; Camblong, H.; Kreckelbergh, S. Control of a Vanadium Redox Battery and Supercapacitor Using a Three-Level Neutral Point Clamped Converter. *J. Power Sources* **2014**, *248*, 1170–1176.

(5) Hall, P. J.; Bain, E. J. Energy-Storage Technologies and Electricity Generation. *Energy Policy* **2008**, *36*, 4352–4355.

(6) Yoldaş, Y.; Önen, A.; Muyeen, S. M.; Vasilakos, A. V.; Alan, İ. Enhancing Smart Grid with Microgrids: Challenges and Opportunities. *Renew. Sustain. Energy Rev.* **2017**, *72*, 205–214.

(7) Chen, S.-M.; Ramachandran, R.; Mani, V.; Saraswathi, R. Recent Advancements in Electrode Materials for the High-Performance Electrochemical Supercapacitors: A Review. *Int. J. Electrochem. Sci.* **2014**, *9*, 4072–4085.

(8) Zhang, L. L.; Zhao, X. S. Carbon-Based Materials as Supercapacitor Electrodes. *Chem. Soc. Rev.* **2009**, *38*, 2520–2531.

(9) Kim, S.-W.; Seo, D.-H.; Ma, X.; Ceder, G.; Kang, K. Electrode Materials for Rechargeable Sodium-Ion Batteries: Potential Alternatives to Current Lithium-Ion Batteries. *Adv. Energy Mater.* **2012**, *2*, 710–721.

(10) Palacín, M. R. Recent Advances in Rechargeable Battery Materials: A Chemist's Perspective. *Chem. Soc. Rev.* 2009, *38*, 2565–2575.

(11) Etacheri, V.; Marom, R.; Elazari, R.; Salitra, G.; Aurbach, D. Challenges in the Development of Advanced Li-Ion Batteries: A Review. *Energy Environ. Sci.* **2011**, *4*, 3243–3262.

(12) Wang, Y.; Cao, G. Developments in Nanostructured Cathode Materials for High-Performance Lithium-Ion Batteries. *Adv. Mater.* **2008**, *20*, 2251–2269.

(13) Liu, C.; Neale, Z. G.; Cao, G. Understanding Electrochemical Potentials of Cathode Materials in Rechargeable Batteries. *Mater. Today* **2016**, *19*, 109–123.

(14) Zhang, X.; Tang, Y.; Zhang, F.; Lee, C.-S. A Novel Aluminum-Graphite Dual-Ion Battery. *Adv. Energy Mater.* **2016**, *6*, 1502588.

(15) Mizushima, K.; Jones, P. C.; Wiseman, P. J.; Goodenough, J. B. Li_xCoO_2 ($0<x<1$): A New Cathode Material for Batteries of High Energy Density. *Mat. Res. Bull.* **1980**, *15*, 783-789.

(16) Buqa, H.; Goers, D.; Holzapfel, M.; Spahr, M. E.; Novák, P. High Rate Capability of Graphite Negative Electrodes for Lithium-Ion Batteries. *J. Electrochem. Soc.* **2005**, *152*, A474-A481.

(17) Choi, N.-S.; Chen, Z.; Freunberger, S. A.; Ji, X.; Sun, Y.-K.; Amine, K.; Yushin, G.; Nazar, L. F.; Cho, J.; Bruce, P. G. Challenges Facing Lithium Batteries and Electrical Double-Layer Capacitors. *Angew. Chem. Int. Ed.* **2012**, *51*, 9994–10024.

(18) Qu, D.; Shi, H. Studies of Activated Carbons Used in Double-Layer Capacitors. *J. Power Sources* **1998**, *74*, 99-107.

(19) Xing, W.; Qiao, S. Z.; Ding, R. G.; Li, F.; Lu, G. Q.; Yan, Z. F.; Cheng, H. M. Superior Electric Double Layer Capacitors Using Ordered Mesoporous Carbons. *Carbon* **2006**, *44*, 216–224.

(20) Portet, C.; Yushin, G.; Gogotsi, Y. Electrochemical Performance of Carbon Onions, Nanodiamonds, Carbon Black and Multiwalled Nanotubes in Electrical Double Layer Capacitors. *Carbon* **2007**, *45*, 2511–2518.

(21) Zhang, Y.; Feng, H.; Wu, X.; Wang, L.; Zhang, A.; Xia, T.; Dong, H.; Li, X.; Zhang, L. Progress of Electrochemical Capacitor Electrode Materials: A Review. *Int. J. Hydrogen Energy* **2009**, *34*, 4889–4899.

(22) Zhong, C.; Deng, Y.; Hu, W.; Qiao, J.; Zhang, L.; Zhang, J. A Review of Electrolyte Materials and Compositions for Electrochemical Supercapacitors. *Chem. Soc. Rev.* **2015**, *44*, 7484–7539.

(23) Augustyn, V.; Simon, P.; Dunn, B. Pseudocapacitive Oxide Materials for High-Rate Electrochemical Energy Storage. *Energy Environ. Sci.* **2014**, *7*, 1597–1614.

(24) Shao, Y.; El-Kady, M. F.; Sun, J.; Li, Y.; Zhang, Q.; Zhu, M.; Wang, H.; Dunn, B.; Kaner, R. B. Design and Mechanisms of Asymmetric Supercapacitors. *Chem. Rev.* **2018**, *118*, 9233–9280.

(25) Lu, Q.; Chen, J. G.; Xiao, J. Q. Nanostructured Electrodes for High-Performance Pseudocapacitors. *Angew. Chem. Int. Ed.* **2013**, *52*, 1882–1889.

(26) Wang, Y.; Yu, S. F.; Sun, C. Y.; Zhu, T. J.; Yang, H. Y. MnO_2/Onion-Like Carbon Nanocomposites for Pseudocapacitors. *J. Mater. Chem.* **2012**, *22*, 17584–17588.

(27) Zhu, Y. G.; Wang, Y.; Shi, Y.; Huang, Z. X.; Fu, L.; Yang, H. Y. Phase Transformation Induced Capacitance Activation for 3D Graphene-CoO Nanorod Pseudocapacitor. *Adv. Energy Mater.* **2014**, *4*, 1301788.

(28) Balaya, P.; Li, H.; Kienle, L.; Maier, J. Fully Reversible Homogeneous and Heterogeneous Li Storage in RuO_2 with High Capacity. *Adv. Funct. Mater.* **2003**, *13*, 621–625.

(29) Sugimoto, W.; Yokoshima, K.; Murakami, Y.; Takasu, Y. Charge Storage Mechanism of Nanostructured Anhydrous and Hydrous Ruthenium-Based Oxides. *Electrochim. Acta* **2006**, *52*, 1742–1748.

(30) Hu, C.-C.; Chang, K.-H.; Lin, M.-C.; Wu, Y.-T. Design and Tailoring of the Nanotubular Arrayed Architecture of Hydrous RuO_2 for Next Generation Supercapacitors. *Nano Lett.* **2006**, *6*, 2690–2695.

(31) Yoshida, N.; Yamada, Y.; Nishimura, S.-I.; Oba, Y.; Ohnuma, M.; Yamada, A. Unveiling the Origin of Unusual Pseudocapacitance of $RuO_2 \cdot nH_2O$ from Its Hierarchical Nanostructure by Small-Angle X-Ray Scattering. *J. Phys. Chem. C* **2013**, *117*, 12003–12009.

(32) Sugimoto, W.; Iwata, H.; Yasunaga, Y.; Murakami, Y.; Takasu, Y. Preparation of Ruthenic Acid

Nanosheets and Utilization of Its Interlayer Surface for Electrochemical Energy Storage. *Angew. Chem. Int. Ed.* **2003**, *42*, 4092–4096.

(33) Sugimoto, W.; Iwata, H.; Yokoshima, K.; Murakami, Y.; Takasu, Y. Proton and Electron Conductivity in Hydrous Ruthenium Oxides Evaluated by Electrochemical Impedance Spectroscopy: The Origin of Large Capacitance. *J. Phys. Chem. B* **2005**, *109*, 7330–7338.

(34) Pomerantseva, E.; Gogotsi, Y. Two-Dimensional Heterostructures for Energy Storage. *Nat. Energy* **2017**, *2*, 17089.

(35) Liu, Y.; Wang, W.; Huang, H.; Gu, L.; Wang, Y.; Peng, X. The Highly Enhanced Performance of Lamellar WS_2 Nanosheet Electrodes upon Intercalation of Single-Walled Carbon Nanotubes for Supercapacitors and Lithium Ions Batteries. *Chem. Commun.* **2014**, *50*, 4485–4488.

(36) Stoller, M. D.; Park, S.; Zhu, Y.; An, J.; Ruoff, R. S. Graphene-Based Ultracapacitors. *Nano Lett.* **2008**, *8*, 3498–3502.

(37) Zhu, C.; Mu, X.; Aken, P. A. V.; Maier, J.; Yu, Y. Fast Li Storage in MoS_2-Graphene-Carbon Nanotube Nanocomposites: Advantageous Functional Integration of 0D, 1D, and 2D Nanostructures. *Adv. Energy Mater.* **2015**, *5*, 1401170.

(38) Romo-Herrera, J. M.; Terrones, M.; Terrones, H.; Dag, S.; Meunier, V. Covalent 2D and 3D Networks from 1D Nanostructures: Designing New Materials. *Nano Lett.* **2007**, *7*, 570–576.

(39) Tiwari, J. N.; Tiwari, R. N.; Kim, K. S. Zero-Dimensional, One-Dimensional, Two-Dimensional and Three-Dimensional Nanostructured Materials for Advanced Electrochemical Energy Devices. *Prog. Mater. Sci.* **2012**, *57*, 724–803.

(40) Ni, J.; Li, Y. Carbon Nanomaterials in Different Dimensions for Electrochemical Energy Storage. *Adv. Energy Mater.* **2016**, *6*, 1600278.

(41) Arie, A. A.; Song, J. O.; Lee, J. K. Structural and Electrochemical Properties of Fullerene-Coated Silicon Thin Film as Anode Materials for Lithium Secondary Batteries. *Mater. Chem. Phys.* **2009**, *113*, 249–254.

(42) Wang, Q.; Wen, Z.; Li, J. A Hybrid Supercapacitor Fabricated with a Carbon Nanotube Cathode and a TiO_2-B Nanowire Anode. *Adv. Funct. Mater.* **2006**, *16*, 2141–2146.

(43) Zhu, X.-D.; Tian, J.; Le, S.-R.; Zhang, N.-Q.; Sun, K.-N. Improved Electrochemical

Performance of $CuCrO_2$ Anode with CNTs as Conductive Agent for Lithium Ion Batteries. *Mater. Lett.* **2013**, *97*, 113–116.

(44) Obreja, V. V. N. On the Performance of Supercapacitors with Electrodes Based on Carbon Nanotubes and Carbon Activated Material-A Review. *Phys. E* **2008**, *40*, 2596–2605.

(45) Novoselov, K. S.; Geim, A. K.; Morozov, S. V.; Jiang, D.; Zhang, Y.; Dubonos, S. V.; Grigorieva, I. V. G.; Firsov, A. A. Electric Field Effect in Atomically Thin Carbon Films. *Science* **2004**, *306*, 666-669.

(46) Allen, M. J.; Tung, V. C.; Kaner, R. B. Honeycomb Carbon: A Review of Graphene. *Chem. Rev.* **2010**, *110*, 132-145.

(47) Lherbier, A.; Blase, X.; Niquet, Y.-M.; Triozon, F.; Roche, S. Charge Transport in Chemically Doped 2D Graphene. *Phys. Rev. Lett.* **2008**, *101*, 036808.

(48) Eichler, J.; Lesniak, C. Boron Nitride (BN) and BN Composites for High-Temperature Applications. *J. Eur. Ceram. Soc.* **2008**, *28*, 1105–1109.

(49) Liu, L.; Peng, Y. P.; Shen, Z. X. Structural and Electronic Properties of *h*-BN. *Phys. Rev. B* **2003**, *68*, 104102.

(50) Gao, Y.-P.; Wu, X.; Huang, K.-J.; Xing, L.-L.; Zhang, Y.-Y.; Liu, L. Two-Dimensional Transition Metal Diseleniums for Energy Storage Application: A Review of Recent Developments. *CrystEngComm.* **2017**, *19*, 404–418.

(51) McDonnell, S. J.; Wallace, R. M. Atomically-Thin Layered Films for Device Applications Based upon 2D TMDC Materials. *Thin Solid Films* **2016**, *616*, 482–501.

(52) Chhowalla, M.; Liu, Z.; Zhang, H. Two-Dimensional Transition Metal Dichalcogenide (TMD) Nanosheets. *Chem. Soc. Rev.* **2015**, *44*, 2584–2586.

(53) Takada, K.; Sakurai, H.; Takayama-Muromachi, E.; Izumi, F.; Dilanian, R. A.; Sasaki, T. Superconductivity in Two-Dimensional CoO_2 Layers. *Nature* 2003, *422*, 53–55.

(54) Ma, R.; Sasaki, T. Two-Dimensional Oxide and Hydroxide Nanosheets: Controllable High-Quality Exfoliation, Molecular Assembly, and Exploration of Functionality. *Acc. Chem. Res.* **2015**, *48*, 136–143.

(55) Koski, K. J.; Cui, Y. The New Skinny in Two-Dimensional Nanomaterials. *ACS Nano* **2013**, *7*, 3739-3743.

(56) Kim, S. J.; Choi, K.; Lee, B.; Kim, Y.; Hong, B. H. Materials for Flexible, Stretchable Electronics: Graphene and 2D Materials. *Annu. Rev. Mater. Res.* **2015**, *45*, 63–84.

(57) Naguib, M.; Kurtoglu, M.; Presser, V.; Lu, J.; Niu, J.; Heon, M.; Hultman, L.; Gogotsi, Y.; Barsoum, M. W. Two-Dimensional Nanocrystals Produced by Exfoliation of Ti_3AlC_2. *Adv. Mater.* **2011**, 4248–4253.

(58) Vogt, P.; Padova, P. D.; Quaresima, C.; Avila, J.; Frantzeskakis, E.; Asensio, M. C.; Resta, A.; Ealet, B.; Lay, G. L. Silicene: Compelling Experimental Evidence for Graphenelike Two-Dimensional Silicon. *Phys. Rev. Lett.* **2012**, *108*, 155501.

(59) Dávila, M. E.; Xian, L.; Cahangirov, S.; Rubio, A.; Lay, G. L. Germanene: A Novel Two-Dimensional Germanium Allotrope Akin to Graphene and Silicene. *New J. Phys.* **2014**, *16*, 095002.

(60) Zhu, F.-F.; Chen, W.-J.; Xu, Y.; Gao, C.-L.; Guan, D.-D.; Liu, C.-H.; Qian, D.; Zhang, S.-C.; Jia, J.-F. Epitaxial Growth of Two-Dimensional Stanene. *Nat. Mater.* **2015**, *14*, 1020–1025.

(61) Yuhara, J.; He, B.; Matsunami, N.; Nakatake, M.; Lay, G. L. Graphene's Latest Cousin: Plumbene Epitaxial Growth on a "Nano WaterCube." *Adv. Mater.* **2019**, 1901017.

(62) Muller, G. A.; Cook, J. B.; Kim, H.-S.; Tolbert, S. H.; Dunn, B. High Performance Pseudocapacitor Based on 2D Layered Metal Chalcogenide Nanocrystals. *Nano Lett.* **2015**, *15*, 1911–1917.

(63) Zhang, X.; Hou, L.; Ciesielski, A.; Samorì, P. 2D Materials Beyond Graphene for High-Performance Energy Storage Applications. *Adv. Energy Mater.* **2016**, *6*, 1600671.

(64) Zhou, S.; Yang, X.; Pei, W.; Liu, N.; Zhao, J. Heterostructures of MXenes and N-Doped Graphene as Highly Active Bifunctional Electrocatalysts. *Nanoscale* **2018**, *10*, 10876–10883.

(65) Yavari, F.; Kritzinger, C.; Gaire, C.; Song, L.; Gulapalli, H.; Borca-Tasciuc, T.; Ajayan, P. M.; Koratkar, N. Tunable Bandgap in Graphene by the Controlled Adsorption of Water Molecules. *Small* **2010**, *6*, 2535–2538.

(66) Song, S. H.; Kim, B. H.; Choe, D.-H.; Kim, J.; Kim, D. C.; Lee, D. J.; Kim, J. M.; Chang, K. J.;

Jeon, S. Bandgap Widening of Phase Quilted, 2D MoS_2 by Oxidative Intercalation. *Adv. Mater.* **2015**, *27*, 3152–3158.

(67) Augustyn, V.; Gogotsi, Y. 2D Materials with Nanoconfined Fluids for Electrochemical Energy Storage. *Joule* **2017**, *1*, 443–452.

(68) Yang, Y.; Liu, X.; Zhu, Z.; Zhong, Y.; Bando, Y.; Golberg, D.; Yao, J.; Wang, X. The Role of Geometric Sites in 2D Materials for Energy Storage. *Joule* **2018**, *2*, 1-20.

(69) Zhang, P.; Wang, F.; Yu, M.; Zhuang, X.; Feng, X. Two-Dimensional Materials for Miniaturized Energy Storage Devices: From Individual Devices to Smart Integrated Systems. *Chem. Soc. Rev.* **2018**, *47*, 7426–7451.

(70) Chen, D.; Tang, L.; Li, J. Graphene-Based Materials in Electrochemistry. *Chem. Soc. Rev.* **2010**, *39*, 3157–3180.

(71) Yan, J.; Liu, J.; Fan, Z.; Wei, T.; Zhang, L. High-Performance Supercapacitor Electrodes Based on Highly Corrugated Graphene Sheets. *Carbon* **2012**, *50*, 2179-2188.

(72) Choi, B. G.; Yang, M.; Hong, W. H.; Choi, J. W.; Huh, Y. S. 3D Macroporous Graphene Frameworks for Supercapacitors with High Energy and Power Densities. *ACS Nano* **2012**, *6*, 4020-4028.

(73) Vivekchand, S. R. C.; Rout, C. S.; Subrahmanyam, K. S.; Govindaraj, A.; Rao, C. N. R. Graphene-Based Electrochemical Supercapacitors. *J. Chem. Sci.* **2008**, *120*, 9-13.

(74) Luan, V. H.; Tien, H. N.; Hoa, L. T.; Hien, N. T. M.; Oh, E.-S.; Chung, J.; Kim, E. J.; Choi, W. M.; Kong, B.-S.; Hur, S.-H. Synthesis of a Highly Conductive and Large Surface Area Graphene Oxide Hydrogel and Its Use in a Supercapacitor. *J. Mater. Chem. A* **2013**, *1*, 208-211.

(75) Lv, W.; Tang, D.-M.;He, Y.-B.; You, C.-H.; Shi, Z.-Q.; Chen, X.-C.; Chen, C.-M.; Hou, P.-X.; Liu, C.; Yang, Q.-H. Low-Temperature Exfoliated Graphenes: Vacuum-Promoted Exfoliation and Electrochemical Energy Storage. *ACS Nano* **2009**, *3*, 3730–3736.

(76) Firmiano, E. G. D. S.; Rabelo, A. C.; Dalmaschio, C. J.; Pinheiro, A. N.; Pereira, E. C.; Schreiner, W. H.; Leite, E. R. Supercapacitor Electrodes Obtained by Directly Bonding 2D MoS_2 on Reduced Graphene Oxide. *Adv. Energy Mater.* **2014**, *4*, 1301380.

(77) Qu, Q.; Yang, S.; Feng, X. 2D Sandwich-like Sheets of Iron Oxide Grown on Graphene as High

Energy Anode Material for Supercapacitors. *Adv. Mater.* **2011**, *23*, 5574–5580.

(78) Niu, L.; Li, Z.; Hong, W.; Sun, J.; Wang, Z.; Ma, L.; Wang, J.; Yang, S. Pyrolytic Synthesis of Boron-Doped Graphene and Its Application as Electrode Material for Supercapacitors. *Electrochim. Acta* **2013**, *108*, 666–673.

(79) Lukatskaya, M. R.; Kota, S.; Lin, Z.; Zhao, M.-Q.; Shpigel, N.; Levi, M. D.; Halim, J.; Taberna, P.-L.; Barsoum, M. W.; Simon, P.; Gogotsi, Y. Ultra-High-Rate Pseudocapacitive Energy Storage in Two-Dimensional Transition Metal Carbides. *Nat. Energy* **2017**, *2*, 17105.

(80) Ivanovskii, A. L.; Enyashin, A. N. Graphene-Like Transition-Metal Nanocarbides and Nanonitrides. *Russ. Chem. Rev.* **2013**, *82*, 735–746.

(81) Liu, G.; Chen, K.; Zhou, H.; Guo, J.; Ren, K.; Ferreira, J. M. F. Layered Growth of Ti_2AlC and Ti_3AlC_2 in Combustion Synthesis. *Mater. Lett.* **2007**, *61*, 779–784.

(82) Jeong, G.-H.; Baek, G.-R.; Zhang, T. F.; Kim, K. H.; Kim, K.; Shin, H. Il; Kang, M.-C. MAX-Phase Ti_2AlC Ceramics: Syntheses, Properties and Feasibility of Applications in Micro Electrical Discharge Machining. *J. Ceram. Process. Res.* **2016**, *17*, 1116–1122.

(83) Li, Z.; Wang, L.; Sun, D.; Zhang, Y.; Liu, B.; Hu, Q.; Zhou, A. Synthesis and Thermal Stability of Two-Dimensional Carbide MXene Ti_3C_2. *Mater. Sci. Eng. B* **2015**, *191*, 33–40.

(84) Eklund, P.; Beckers, M.; Jansson, U.; Högberg, H.; Hultman, L. The $M_{n+1}AX_n$ Phases: Materials Science and Thin-Film Processing. *Thin Solid Films* **2010**, *518*, 1851–1878.

(85) Barsoum, M. W.; El-Raghy, T. The MAX Phases: Unique New Carbide and Nitride Materials. *Am. Sci.* **2001**, *89*, 334-343.

(86) Dong, Y.; Mallineni, S. S. K.; Maleski, K.; Behlow, H.; Mochalin, V. N.; Rao, A. M.; Gogotsi, Y.; Podila, R. Metallic MXenes: A New Family of Materials for Flexible Triboelectric Nanogenerators. *Nano Energy* **2018**, *44*, 103–110.

(87) Naguib, M.; Gogotsi, Y. Synthesis of Two-Dimensional Materials by Selective Extraction. *Acc. Chem. Res.* **2015**, *48*, 128–135.

(88) Maleski, K.; Mochalin, V. N.; Gogotsi, Y. Dispersions of Two-Dimensional Titanium Carbide MXene in Organic Solvents. *Chem. Mater.* **2017**, *29*, 1632–1640.

(89) Sun, W.; Li, Y.; Wang, B.; Jiang, X.; Katsnelson, M. I.; Korzhavyi, P.; Eriksson, O.; Marco, I. D. A New 2D Monolayer BiXene, M_2C (M = Mo, Tc, Os). *Nanoscale* **2016**, *8*, 15753–15762.

(90) Naguib, M.; Mochalin, V. N.; Barsoum, M. W.; Gogotsi, Y. 25^{th} Anniversary Article: MXenes : A New Family of Two-Dimensional Materials. *Adv. Mater.* **2014**, *26*, 992–1005.

(91) Naguib, M.; Mashtalir, O.; Carle, J.; Presser, V.; Lu, J.; Hultman, L.; Gogotsi, Y.; Barsoum, M. W. Two-Dimensional Transition Metal Carbides. *ACS Nano* **2012**, *6*, 1322-1331.

(92) Mashtalir, O.; Naguib, M.; Dyatkin, B.; Gogotsi, Y.; Barsoum, M. W. Kinetics of Aluminum Extraction from Ti_3AlC_2 in Hydrofluoric Acid. *Mater. Chem. Phys.* **2013**, *139*, 147–152.

(93) Ghidiu, M.; Lukatskaya, M. R.; Zhao, M.-Q.; Gogotsi, Y.; Barsoum, M. W. Conductive Two-Dimensional Titanium Carbide 'Clay' with High Volumetric Capacitance. *Nature* **2014**, *516*, 78-82.

(94) Alhabeb, M.; Maleski, K.; Anasori, B.; Lelyukh, P.; Clark, L.; Sin, S.; Gogotsi, Y. Guidelines for Synthesis and Processing of Two-Dimensional Titanium Carbide ($Ti_3C_2T_x$ MXene). *Chem. Mater.* **2017**, *29*, 7633-7644.

(95) Kajiyama, S.; Szabova, L.; Iinuma, H.; Sugahara, A.; Gotoh, K.; Sodeyama, K.; Tateyama, Y.; Okubo, M.; Yamada, A. Enhanced Li-Ion Accessibility in MXene Titanium Carbide by Steric Chloride Termination. *Adv. Energy Mater.* **2017**, *7*, 1601873.

(96) Anasori, B.; Lukatskaya, M. R.; Gogotsi, Y. 2D Metal Carbides and Nitrides (MXenes) for Energy Storage. *Nat. Rev. Mater.* **2017**, *2*, 16098.

(97) Römer, F. M.; Wiedwald, U.; Strusch, T.; Halim, J.; Mayerberger, E.; Barsoum, M. W.; Farle, M. Controlling the Conductivity of Ti_3C_2 MXenes by Inductively Coupled Oxygen and Hydrogen Plasma Treatment and Humidity. *RSC Adv.* **2017**, *7*, 13097–13103.

(98) Ghidiu, M.; Kota, S.; Halim, J.; Sherwood, A. W.; Nedfors, N.; Rosen, J.; Mochalin, V. N.; Barsoum, M. W. Alkylammonium Cation Intercalation into Ti_3C_2 (MXene): Effects on Properties and Ion-Exchange Capacity Estimation. *Chem. Mater.* **2017**, *29*, 1099–1106.

(99) Zhang, Y.; Zha, X.-H.; Luo, K.; Qiu, N.; Zhou, Y.; He, J.; Chai, Z.; Huang, Z.; Huang, Q.; Liang, Y.; Du, S. Tuning the Electrical Conductivity of Ti_2CO_2 MXene by Varying the Layer Thickness and Applying Strains. *J. Phys. Chem. C* **2019**, *123*, 6802-6811.

(100) Ling, Z.; Ren, C. E.; Zhao, M.-Q.; Yang, J.; Giammarco, J. M.; Qiu, J.; Barsoum, M. W.; Gogotsi, Y. Flexible and Conductive MXene Films and Nanocomposites with High Capacitance. *Proc. Natl. Acad. Sci.* **2014**, *111*, 16676–16681.

(101) Guo, J.; Peng, Q.; Fu, H.; Zou, G.; Zhang, Q. Heavy-Metal Adsorption Behavior of Two-Dimensional Alkalization-Intercalated MXene by First-Principles Calculations. *J. Phys. Chem. C* **2015**, *119*, 20923–20930.

(102) Ren, C. E.; Alhabeb, M.; Byles, B. W.; Zhao, M.-Q.; Anasori, B.; Pomerantseva, E.; Mahmoud, K. A.; Gogotsi, Y. Voltage-Gated Ions Sieving through 2D MXene $Ti_3C_2T_x$ Membranes. *ACS Appl. Nano Mater.* **2018**, *1*, 3644–3652.

(103) Ma, T. Y.; Cao, J. L.; Jaroniec, M.; Qiao, S. Z. Interacting Carbon Nitride and Titanium Carbide Nanosheets for High-Performance Oxygen Evolution. *Angew. Chem. Int. Ed.* **2016**, *55*, 1138–1142.

(104) Seh, Z. W.; Fredrickson, K. D.; Anasori, B.; Kibsgaard, J.; Strickler, A. L.; Lukatskaya, M. R.; Gogotsi, Y.; Jaramillo, T. F.; Vojvodic, A. Two-Dimensional Molybdenum Carbide (MXene) as an Efficient Electrocatalyst for Hydrogen Evolution. *ACS Energy Lett.* **2016**, *1*, 589-594.

(105) Chen, J.; Chen, K.; Tong, D.; Huang, Y.; Zhang, J.; Xue, J.; Huang, Q.; Chen, T. CO_2 and Temperature Dual Responsive "Smart" MXene Phases. *Chem. Commun.* **2015**, *51*, 314–317.

(106) Rasool, K.; Helal, M.; Ali, A.; Ren, C. E.; Gogotsi, Y.; Mahmoud, K. A. Antibacterial Activity of $Ti_3C_2T_x$ MXene. *ACS Nano* **2016**, *10*, 3674–3684.

(107) Lukatskaya, M. R.; Mashtalir, O.; Ren, C. E.; Agnese, Y. D.; Rozier, P.; Taberna, P. L.; Naguib, M.; Simon, P.; Barsoum, M. W.; Gogotsi, Y. Cation Intercalation and High Volumetric Capacitance of Two-Dimensional Titanium Carbide. *Science* **2013**, *341*, 1502-1505.

(108) Okubo, M.; Sugahara, A.; Kajiyama, S.; Yamada, A. MXene as a Charge Storage Host. *Acc. Chem. Res.* **2018**, *51*, 591-599.

(109) Sugahara, A.; Ando, Y.; Kajiyama, S.; Yazawa, K.; Gotoh, K.; Otani, M.; Okubo, M.; Yamada, A. Negative Dielectric Constant of Water Confined in Nanosheets. *Nat. Commun.* **2019**, *10*, 850.

(110) Naguib, M.; Halim, J.; Lu, J.; Cook, K. M.; Hultman, L.; Gogotsi, Y.; Barsoum, M. W. New Two-Dimensional Niobium and Vanadium Carbides as Promising Materials for Li-Ion Batteries. *J.*

Am. Chem. Soc. **2013**, *135*, 15966-15969.

(111) Agnese, Y. D.; Lukatskaya, M. R.; Cook, K. M.; Taberna, P.-L.; Gogotsi, Y.; Simon, P. High Capacitance of Surface-Modified 2D Titanium Carbide in Acidic Electrolyte. *Electrochem. commun.* **2014**, *48*, 118–122.

(112) Xia, Y.; Mathis, T. S.; Zhao, M.-Q.; Anasori, B.; Dang, A.; Zhou, Z.; Cho, H.; Gogotsi, Y.; Yang, S. *Nature* **2018**, *557*, 409-414.

(113) Lukatskaya, M. R.; Bak, S.-M.; Yu, X.; Yang, X.-Q.; Barsoum, M. W.; Gogotsi, Y. Probing the Mechanism of High Capacitance in 2D Titanium Carbide Using in Situ X-Ray Absorption Spectroscopy. *Adv. Energy Mater.* **2015**, *5*, 1500589.

(114) Hu, M.; Li, Z.; Hu, T.; Zhu, S.; Zhang, C.; Wang, X. High-Capacitance Mechanism for $Ti_3C_2T_x$ MXene by *in Situ* Electrochemical Raman Spectroscopy Investigation. *ACS Nano* **2016**, *10*, 11344–11350.

(115) Xu, M.; Lei, S.; Qi, J.; Dou, Q.; Liu, L.; Lu, Y.; Huang, Q.; Shi, S.; Yan, X. Opening Magnesium Storage Capability of Two-Dimensional MXene by Intercalation of Cationic Surfactant. *ACS Nano* **2018**, *12*, 3733–3740.

(116) Mashtalir, O.; Lukatskaya, M. R.; Kolesnikov, A. I.; Raymundo-Piñero, E.; Naguib, M.; Barsoum, M. W.; Gogotsi, Y. The Effect of Hydrazine Intercalation on the Structure and Capacitance of 2D Titanium Carbide (MXene). *Nanoscale* **2016**, *8*, 9128–9133.

(117) Mashtalir, O.; Lukatskaya, M. R.; Zhao, M.-Q.; Barsoum, M. W.; Gogotsi, Y. Amine-Assisted Delamination of Nb_2C MXene for Li-Ion Energy Storage Devices. *Adv. Mater.* **2015**, *27*, 3501–3506.

(118) Zhao, M.-Q.; Ren, C. E.; Ling, Z.; Lukatskaya, M. R.; Zhang, C.; Aken, K. L. V.; Barsoum, M. W.; Gogotsi, Y. Flexible MXene/Carbon Nanotube Composite Paper with High Volumetric Capacitance. *Adv. Mater.* **2015**, *27*, 339–345.

(119) Zhang, X.; Liu, Y.; Dong, S.; Yang, J.; Liu, X. Flexible Electrode Based on Multi-Scaled MXene ($Ti_3C_2T_x$) for Supercapacitors. *J. Alloys Compd.* **2019**, *790*, 517–523.

(120) Mashtalir, O.; Naguib, M.; Mochalin, V. N.; Agnese, Y. D.; Heon, M.; Barsoum, M. W.; Gogotsi, Y. Intercalation and Delamination of Layered Carbides and Carbonitrides. *Nat. Commun.* **2013**, *4*, 1716.

(121) Yang, J.; Bao, W.; Jaumaux, P.; Zhang, S.; Wang, C.; Wang, G. MXene-Based Composites: Synthesis and Applications in Rechargeable Batteries and Supercapacitors. *Adv. Mater. Interfaces* **2019**, 1802004.

(122) Chen, C.; Xie, X.; Anasori, B.; Sarycheva, A.; Makaryan, T.; Zhao, M.; Urbankowski, P.; Miao, L.; Jiang, J.; Gogotsi, Y. MoS_2-on-MXene Heterostructures as Highly Reversible Anode Materials for Lithium-Ion Batteries. *Angew. Chem. Int. Ed.* **2018**, *57*, 1846–1850.

(123) Guo, Z.; Zhou, J.; Sun, Z. New Two-Dimensional Transition Metal Borides for Li Ion Batteries and Electrocatalysis. *J. Mater. Chem. A Mater.* **2017**, *5*, 23530–23535.

Chapter 2: General experimental procedures

In this chapter, detailed experimental information on synthesis of MAX/MXene and MAB/MBene, and characterization is described. Moreover, electrode and electrolyte preparation, electrochemical measurement methods, and data interpretation are provided.

2.1 Synthesis

Ti_2CT_x and $Ti_3C_2T_x$ MXenes have mostly been used in this thesis. For exploring electrochemical behavior of other MXenes, Mo_2CT_x and Nb_2CT_x have been partially investigated as well.

Synthesis of MAX Phase Ti_2AlC and Ti_2CT_x

A mixture of Ti (High Purity Chemicals, Japan), Al (High Purity Chemicals, Japan), and TiC (High Purity Chemicals, Japan) was poured into a ball milling pod in a molar ratio of 1.2:1.2:1 followed by zirconia-ball milling for 1 h at 200 rpm. After ball milling, the obtained powder was pelletized under 30 MPa pressure and heated in a high-frequency induction furnace at 1350 ˚C for 1 h with a temperature increase rate of 10 ˚C/min under Ar flow. The heated pellet was crushed with a metal mortar and ball-milled again for 1 h at 200 rpm to obtain a uniform Ti_2AlC powder.

A Ti_2CT_x powder was prepared by an acid treatment of Ti_2AlC with LiF and HCl. A 0.709 g (0.9 M) portion of LiF (Wako Chemicals, Japan) was added to 30 mL of 6 M HCl (Kanto Chemicals, Japan) followed by the addition of 0.5 g of Ti_2AlC into the PTFE flask. The mixture was stirred for 15 h in a 40 ˚C water bath. After the acid treatment, the Ti_2CT_x slurry was filtered and washed with deionized water until the pH of the filtrate becomes neutral. Then, the filtered Ti_2CT_x was vacuum-dried at 60 ˚C for 12 h.[1,2]

Synthesis of MAX Phase Ti_3AlC_2 and $Ti_3C_2T_x$

The precursor Ti_2AlC was obtained by following above procedures. For synthesis of Ti_3AlC_2, Ti_2AlC and TiC powders were well-mixed in a molar ratio of 1:1 by ball-milling for 1 h at 200 rpm. The obtained mixture was pressed in a pellet form at 30 MPa and heated at 1350 ˚C for 1 h under Ar flow. The heated pellet was crushed and ball-milled for 1h at 200 rpm.

For synthesis of $Ti_3C_2T_x$, 2.3 g (3 M) portion of LiF was added to 30 mL of 10 M HCl followed by the addition of 0.5 g of Ti_3AlC_2 into the PTFE flask. The mixture was continuously stirred for 15 h at 40 ˚C in a water bath. After washing the obtained slurry with 1 M HCl, the $Ti_3C_2T_x$ slurry was

filtered and dried at 60 ˚C overnight under vacuum.[3]

Synthesis of MAX phase Nb_2AlC and Nb_2CT_x

A mixture of Nb (High Purity Chemicals, Japan), Al (High Purity Chemicals, Japan), and NbC (High Purity Chemicals, Japan) was poured into a ball milling pod in a molar ratio of 1.1:1.2:1 followed by zirconia-ball milling for 1 h at 200 rpm. After ball milling, the obtained powder was pelletized under 30 MPa pressure and heated in a high-frequency induction furnace at 1500 ˚C for 1 h with a temperature increase rate of 10 ˚C/min under Ar flow. The heated pellet was crushed with a metal mortar and ball-milled again for 1 h at 200 rpm to obtain a uniform Nb_2AlC powder.

For synthesis of Nb_2CT_x, 2.3 g (3 M) portion of LiF was added to 30 mL of 12 M HCl followed by the addition of 1.0 g of Nb_2AlC into the PTFE flask. The mixture was continuously stirred for 6 days at 55 ˚C in an oil bath. After washing the obtained slurry with 1 M HCl, the Nb_2CT_x slurry was filtered and dried at 60 ˚C overnight under vacuum.[4]

Synthesis of MAX phase Mo_2Ga_2C and Mo_2CT_x

A mixture of Mo_2C (High Purity Chemicals, Japan) and Ga (High Purity Chemicals, Japan) was well-mixed in a molar ratio of 1:8 and poured in the quartz tube. Under the vacuum, quartz tube was sealed, placed in the furnace, and heated at 850 ˚C for 48 h. A sintered mixture was extracted from the quartz tube and placed in 12 M HCl solution to dissolve excess amount of Ga. After drying, the prepared mixture was sealed in quartz tube and re-heated at 850 ˚C for 24 h in the same manner as above. After crushing the obtained mixture, pure Mo_2Ga_2C powder was obtained.[5]

For synthesis of Mo_2CT_x, 1.0 g of Mo_2Ga_2C powder was slowly poured into a solution consisting of 1.56 g (3 M) of LiF and 20 mL of 12 M HCl. The mixture was continuously stirred for a week at 55 ˚C in an oil bath. The resulting precipitate was stirred in 1 M HCl solution, filtered, and washed with deionized water until the pH reaches to neutral. The separated slurry was dried at 60 ˚C for 12 h under vacuum.

Synthesis of MAB phase MoAlB and phase pure Mo_2AlB_2

The mixture of MoB (High Purity Chemicals, Japan) and Al (High Purity Chemicals, Japan) in a molar ratio of 1:1.15 was pelletized under 40 MPa pressure and heated to 1200 ˚C for 1 h under Ar atmosphere using a high-frequency induction furnace. The heated pellet was powdered by milling with zirconia balls to obtain a uniform MoAlB powder.[6,7]

For synthesis of phase pure Mo_2AlB_2, 0.5 g of MoAlB powder was slowly poured into a solution

consisting of 2.3 g (3 M) of LiF (Wako Chemicals, Japan) and 30 mL of 10 M HCl (Kanto Chemicals, Japan). The mixture was continuously stirred for 48 h at 40 ˚C. The resulting precipitate was stirred in a 1 M HCl solution, then filtered, and washed with deionized water until the pH reaches to neutral. The separated powder was dried at 60 ˚C for 12 h under vacuum.

2.2 Characterization

The crystalline structure of obtained materials was analyzed by *X-ray diffraction* (XRD, Rigaku, RINT-TTR III) with Cu Kα radiation. XRD data were recorded in the 2θ range of 3-80° with a step size of 0.02°. Morphologies of obtained materials were observed with a *scanning electron microscope* (SEM, Hitachi, S-4800). TEM images of the MoAlB and Mo_2AlB_2 were collected using *transmission electron microscopy* (TEM, JEOL, JEM-2100). Chemical composition was evaluated by *energy-dispersive X-ray spectroscopy* (EDX, JEOL, JEM-6510LA). For the structure of electrolytes and salts, *Raman spectroscopy* (JASCO, NRS-5100) was measured using a 532 nm laser in the wave number range of 300-4000 cm^{-1}. The surface was analyzed by X-ray photoelectron spectroscopy (XPS, PHI 5000 VersaProbeII, ULVAC-PHI) with a monochromatic Al Kα radiation.

2.3 Electrochemistry

Electrode preparation

To prepare an electrode film (of Ti_2CT_x or activated carbon), the active material was well mixed in a mortar with acetylene black (AB), and PTFE binder in the weight ratio of active material:AB:PTFE of 8:1:1. The prepared film was rolled using a glass stick with a loading of ~5.0 mg/cm^2 for the MXene electrodes and ~2.5 mg/cm^2 for activated carbon electrode and finally pressed on a mesh.

To investigate full-cell performance, active material Ti_2CT_x (or activated carbon) was mixed with acetylene black and polyvinylidene fluoride (PVDF) in weight ratio of 8:1:1 in appropriate amount of N-methylpyrrolidone (Kanto Chemical). Obtained slurries were pasted on Al foil (for Ti_2CT_x, hydrate melt) or Ti foil (for the others) with a loading of ~1.2 mg/cm^2 for Ti_2CT_x and ~2.0 mg/cm^2 for activated carbon, and then dried overnight at 120 ˚C under vacuum. After drying, the prepared electrodes were used as the anode (MXene electrodes) and cathode (activated carbon electrode).

Electrolyte preparation

Lithium bis-(trifluoro methane sulfonyl) imide (LiTFSI) and lithium bis-(pentafluoro ethane sulfonyl) imide (LiBETI) were purchased from Kishida Chemicals, Japan. To obtain a hydrate melt

($Li(TFSI)_{0.7}(BETI)_{0.3}\cdot 2H_2O$) electrolyte, an appropriate amount of LiTFSI and LiBETI salts were dissolved in ultrapure water (Kanto Chemicals, Japan). For various concentrations of LiTFSI aqueous electrolyte, a proper amount of LiTFSI salt (1.0, 3.0, 5.2 M) was dissolved in ultrapure water. Note that 5.2 M LiTFSI aqueous electrolyte equals to 21 m LiTFSI well-known as water-in-salt. And 1.0 M $Li_2SO_4\cdot H_2O$ electrolyte was prepared by dissolving proper amount (1.0 M) of $Li_2SO_4\cdot H_2O$ (Wako Chemicals, Japan) in ultrapure water.

Electrochemical cell configuration

Electrochemical measurements were conducted in a three-electrode cell and a 2032-type two-electrode coin cell as illustrated in **Figure 2.3**. For a three-electrode cell, electrochemical active materials (MXenes or activated carbon) were used as working electrodes, excess amounts of activated carbon or Pt (for linear sweep voltammetry of current collector) were served as counter electrodes, and Ag/AgCl (in 3 M KCl) was employed as a reference electrode. For a 2032-type two-electrode coin cell, MXene electrode, activated carbon, and glass-fiber (GF/F, Whatman) were used as a working (anode), counter electrode (cathode), and separator, respectively to evaluate full-cell performances.

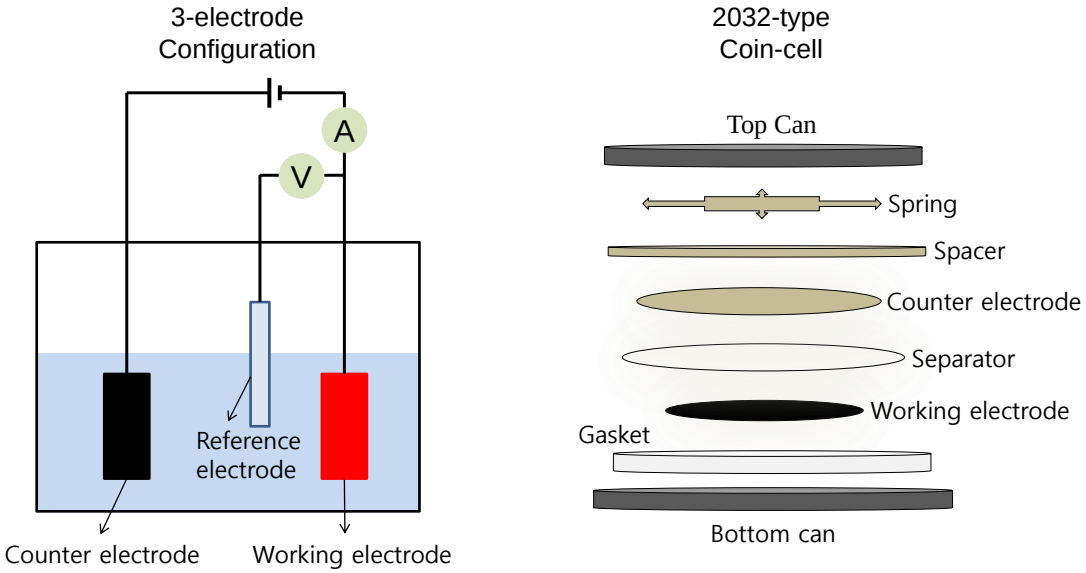

Figure 2.3 Schematic design of 3-electrode configuration and 2032-type 2-electrode coin cell.

Electrochemical measurements

Linear sweep voltammetry (LSV, VMP3 potentiostat, BioLogic) of current collectors was conducted at a scan rate of 0.1 mV/s. *Chronoamperometry* (CA, VMP3 potentiostat, BioLogic) was

recorded at various applied potentials until reaching a steady state to determine a electrochemical potential window. *Cyclic voltammetry* (CV, VMP3 potentiostat, BioLogic) was performed with a specific scan rate. *Charge/discharge test* (TOSCAT-3100, Tokyo System) was conducted with a specific current rate. *Electrochemical impedance spectroscopy* (EIS, VMP3 potentiostat, BioLogic) was recorded with an amplitude of 10 mV in the frequency range of 10 mHz to 200 kHz.

Data interpretation

Averaged capacitance and activation energies can be calculated by theoretical equations based on experimental results.

Calculation of averaged capacitance (*C*)

Averaged capacitance *C* (F/g) can be obtained by integrating a cyclic voltammogram. Given that V is potential, ΔV is operating potential range ($2\Delta V$ is operating potential range for round sweep), m is mass of active material in the electrode, and s is scan rate, and $\int i(V)dV$ is total current obtained by integration of positive and negative sweep in CV, averaged capacitance can be expressed as:

$$C = \frac{\int i(V)dV}{2\Delta V m s}$$

Calculation of activation energy (E_A) of charge transfer based on EIS

Activation energy (E_A) of charge transfer can be calculated by Arrhenius equation. Given that R_s (or R_i) is resistance of charge transfer in bulk electrolyte (or interface) served as the value of rate coefficient, A is frequency factor, E_A is activation energy, R is gas constant, and T is absolute temperature, Arrhenius equation can be transformed as:

$$\ln R_s^{-1} \text{ (or } \ln R_i^{-1}) = \ln A + \frac{-E_A}{1000R}\left(\frac{1000}{T}\right)$$

References

(1) Kajiyama, S.; Szabova, L.; Iinuma, H.; Sugahara, A.; Gotoh, K.; Sodeyama, K.; Tateyama, Y.; Okubo, M.; Yamada, A. Enhanced Li-Ion Accessibility in MXene Titanium Carbide by Steric Chloride Termination. *Adv. Energy Mater.* **2017**, *7*, 1601873.

(2) Wang, X.; Kajiyama, S.; Iinuma, H.; Hosono, E.; Oro, S.; Moriguchi, I.; Okubo, M.; Yamada, A. Pseudocapacitance of MXene Nanosheets for High-Power Sodium-Ion Hybrid Capacitors. *Nat.*

Commun. **2015**, *6*, 6544.

(3) Kajiyama, S.; Szabova, L.; Sodeyama, K.; Iinuma, H.; Morita, R.; Gotoh, K.; Tateyama, Y.; Okubo, M.; Yamada, A. Sodium-Ion Intercalation Mechanism in MXene Nanosheets. *ACS Nano* **2016**, *10*, 3334–3341.

(4) Naguib, M.; Halim, J.; Lu, J.; Cook, K. M.; Hultman, L.; Gogotsi, Y.; Barsoum, M. W. New Two-Dimensional Niobium and Vanadium Carbides as Promising Materials for Li-Ion Batteries. *J. Am. Chem. Soc.* **2013**, *135*, 15966-15969.

(5) Halim, J.; Kota, S.; Lukatskaya, M. R.; Naguib, M.; Zhao, M.-Q.; Moon, E. J.; Pitock, J.; Nanda, J.; May, S. J.; Gogotsi, Y.; Barsoum, M. W. Synthesis and Characterization of 2D Molybdenum Carbide (MXene). *Adv. Funct. Mater.* **2016**, *26*, 3118-3127.

(6) Alameda, L. T.; Holder, C. F.; Fenton, J. L.; Schaak, R. E. Partial Etching of Al from MoAlB Single Crystals to Expose Catalytically Active Basal Planes for the Hydrogen Evolution Reaction. *Chem. Mater.* **2017**, *29*, 8953–8957.

(7) Alameda, L. T.; Moradifar, P.; Metzger, Z. P.; Alem, N.; Schaak, R. E. Topochemical Deintercalation of Al from MoAlB: Stepwise Etching Pathway, Layered Intergrowth Structures, and Two-Dimensional MBene. *J. Am. Chem. Soc.* **2018**, *140*, 8833–8840.

Chapter 3: Dense charge accumulation in MXene with hydrate-melt electrolyte

3.1 Introduction

Renewable energy systems are in urgent demand; however, integration of renewable energy into electrical grids requires rapid load-leveling of abrupt power spikes/drops and a wide distribution of high-power energy storage devices represents the most promising solution. However, current electrochemical energy storage devices do not meet all the requirements for grid-scale use, particularly because of slow charge/discharge rates caused by limited ion transport.[1-4]

Supercapacitors have rapid operation owing to the formation of an electric double-layer (EDL) at the electrode surface, which contributes to a higher power density and longer cycle lifetime than achievable in conventional batteries.[5-8] In particular, supercapacitors based on aqueous electrolytes are attractive because of their low cost, high ion conductivity, non-flammability, and eco-friendliness[9-11] However, the energy density of such devices is severely limited by the narrow potential window of water (1.23 V).[12-14]

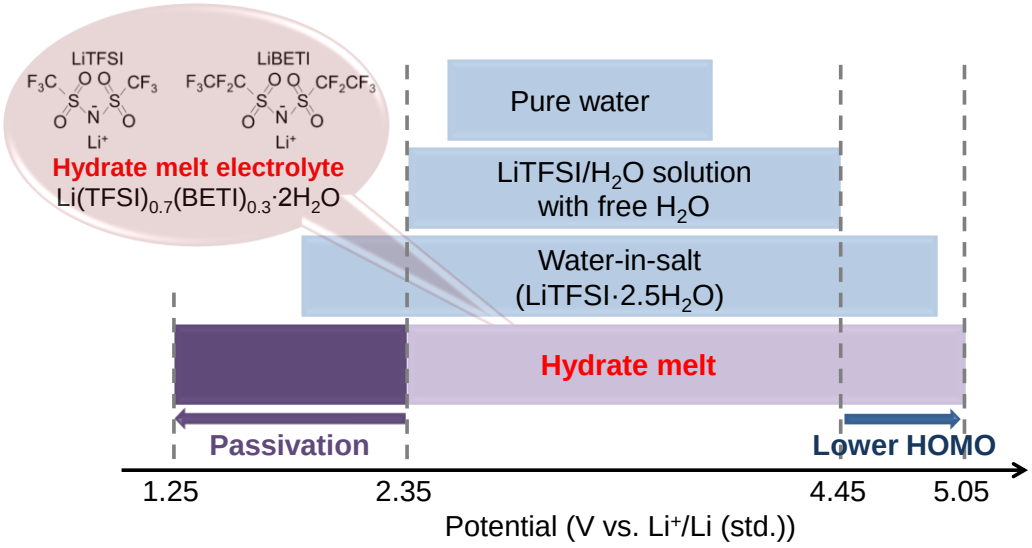

Figure 3.1 Electrochemical potential window of pure water, LiTFSI/H_2O solution with free H_2O, and a hydrate melt aqueous electrolytes.[15,16]

To overcome this obstacle, I focus on a highly-concentrated aqueous electrolyte known as a hydrate melt ($Li(TFSI)_{0.7}(BETI)_{0.3}\cdot 2H_2O$, TFSI: bis(trifluoromethanesulfonyl)imide, BETI: bis(pentafluoroethanesulfonyl)imide), providing wide electrochemical potential window as shown in **Figure 3.1**.[15] Unlike highly-concentrated aqueous electrolytes called water-in-salt ($LiTFSI\cdot 2.5H_2O$) with more than 10% of free water molecules,[16] hydrate melts are defined as liquids in which all water molecules are independent of each other but interact with other species without forming a hydrogen

bonding network. Owing to their unique local coordination structure, a hydrate melt shows an exceptionally wide electrochemical potential window (> 3 V), which far exceeds the thermodynamic hydrogen/oxygen evolution limits of water (1.23 V).[15-18] Even though water-in-salt offers a better electrochemical stability than those of dilute LiTFSI system and pure water, it shows narrower electrochemical potential window (3.0 V) than that of a hydrate melt (3.8 V) as shown in **Figure 3.1**.[15,16] In particular, the notable difference with water-in-salt and hydrate melt is cathodic electrochemical stability because solid electrolyte interphase (SEI) film on a negative electrode plays critical role of suppressing hydrogen evolution reaction (HER). As shown in **Figure 3.2**, $Li_2(TFSI)(H_2O)_x$ (or $Li_2(BETI)(H_2O)_x$) complexes are formed in concentrated electrolytes, which become reductively unstable below 2.90 V vs. Li^+/Li. Therefore, anions are first decomposed before hydrogen evolution (2.63 V vs. Li^+/Li) and anion-derived SEI film suppresses water decomposition.[15,16] Here, hydrate melt offers more stable SEI formation than water-in-salt, because how much super-concentration promotes anion decomposition in competition with hydrogen evolution. Also, SEI in hydrate melt without any free water molecules is well maintained because anion-derived SEI compounds are well-known as water-soluble. As for anodic electrochemical stability in concentrated electrolytes, lower HOMO (highest occupied molecular orbital) level of oxygen atom in a water molecule (or dissociated OH^-), which donates its electron to the Li^+, enhances the oxidation potential.[15] Hydrate melt in which all water molecules are coordinated to Li^+ shows slightly wider anodic potential window than that of water-in-salt as shown in **Figure 3.1**.

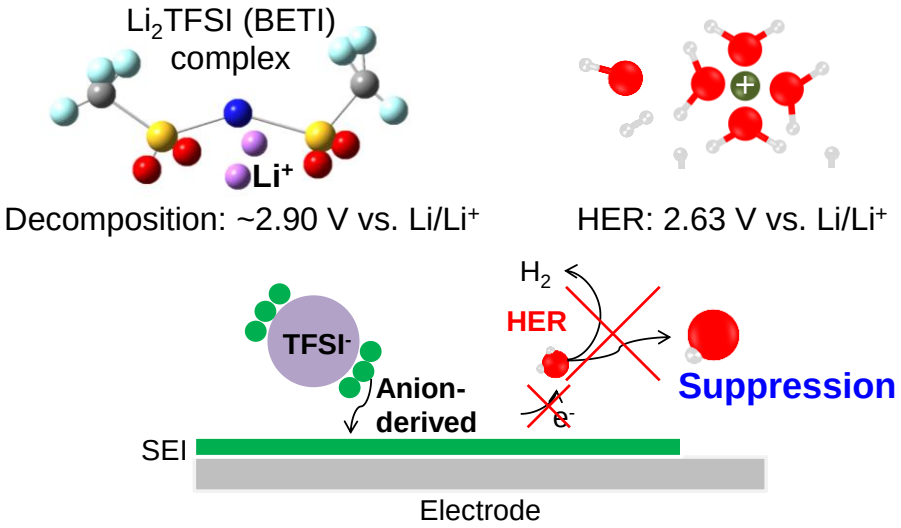

Figure 3.2 Schematic design of atmosphere of chemical species in concentrated aqueous electrolytes. Concentrated electrolytes provide stable anion-based SEI film suppressing hydrogen evolution, while free waters can easily decomposed evolving hydrogen gas in dilute system with no stable SEI film.

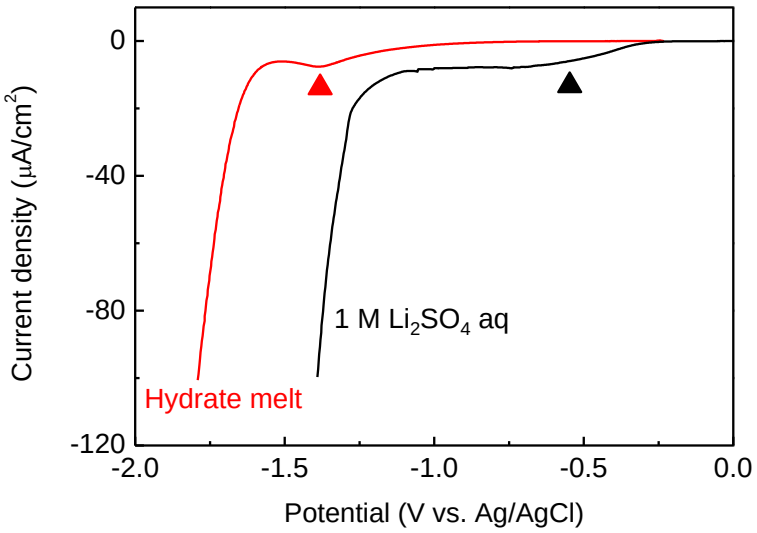

Figure 3.3 Cathodic linear sweep voltammetry of a 1 M Li_2SO_4 aqueous electrolyte and a hydrate melt electrolyte with a Ti electrode at a sweep rate of 0.1 mV/s. Red and black triangles indicate cathodic current flow due to solid-electrolyte formation before hydrogen evolution.

For example, cathodic linear sweep voltammetry indicates that hydrogen evolution reaction with a hydrate melt electrolyte is suppressed down to -1.6 V vs. Ag/AgCl, which is considerably lower than that with a 1 M Li_2SO_4 aqueous electrolyte (**Figure 3.3**). Aqueous supercapacitors based on a hydrate-melt electrolyte are expected to realize much higher voltage operation and hence much higher energy densities with an appropriate choice of electrode materials. Indeed, some research groups have reported high-voltage aqueous energy storage systems using concentrated aqueous electrolytes as shown in **Figure 3.4**.[19-24] L. Suo *et al.*[16] reported a full Li-ion battery with a $LiMn_2O_4$ and Mo_6S_8 in water-in-salt, displaying an operating voltage of 2.3 V. Using a 4.6 V $Ni^{2+}/^{3+}$ redox, F. Wang *et al.* reported full $Mo_6S_8/LiNi_{0.5}Mn_{1.5}O_4$ Li-ion battery in water-in-salt with an operating voltage of 2.5 V. Using water-in-salt, M. Zhang *et al.*[22] reported a 2.0 V aqueous supercapacitor with an activated carbon and MnO_2. A hydrate melt aqueous electrolyte[15] showed full $Li_4Ti_5O_{12}/LiNi_{0.5}Mn_{1.5}O_4$ Li-ion battery with an operation voltage of 3.1 V. Beyond water-in-salt and a hydrate melt, M.R. Lukatskaya *et al.*[25] discovered another concentrated aquoues electrolyte ($Li_{0.2}K_{0.8}OAc \cdot 1.3H_2O$), which can operate full *c*-$TiO_2/LiMn_2O_4$ Li-ion battery operation with a voltage window of 2.5 V.

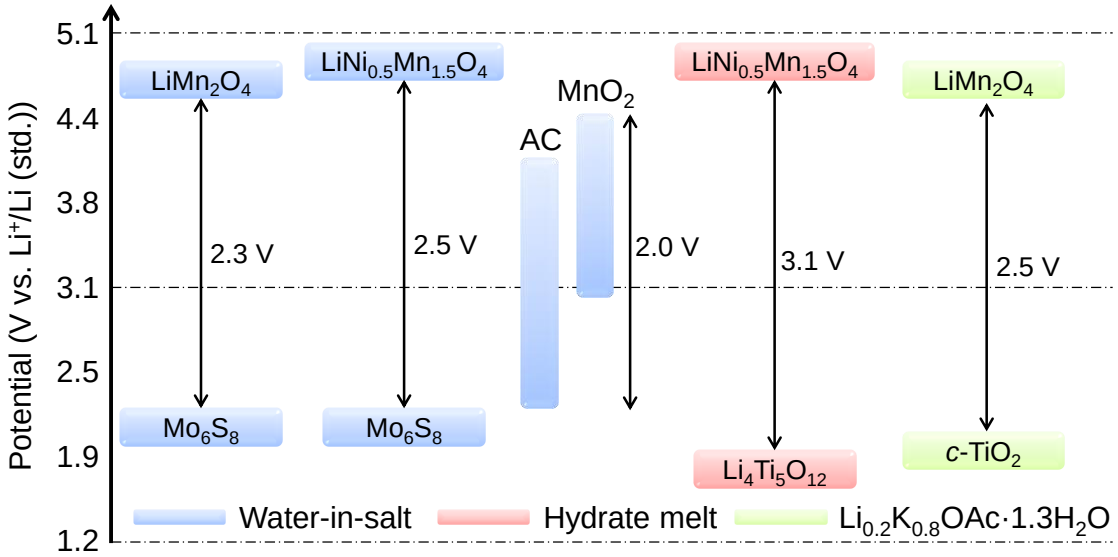

Figure 3.4 Applications of concentrated electrolytes (water-in-salt, hydrate melt, and $Li_{0.2}K_{0.8}OAc{\cdot}1.3H_2O$). All concentrated electrolytes provide high operation potential over 2 V, far exceeding limit of water decomposition.

As an electrode material that can maximize use of the wide electrochemical window provided by hydrate-melt electrolytes, I used transition-metal carbides MXene $M_{n+1}X_nT_x$ (M: Ti, Nb, Mo, V, *etc.*; X: C; *n*: 1, 2, or 3; T_x: surface termination group (OH, O, F, Cl)). MXene is an emerging class of two-dimensional nanosheets obtained by removing A layers from MAX phases (general formula: $M_{n+1}AX_n$, A: Al, Ga, Si, Ge, *etc.*).[26-36] Because MXenes are reported to provide a large specific capacitance greater than 300 F/g in conventional aqueous electrolytes,[37] their combination with a hydrate-melt electrolyte should realize a much higher energy density.

In this work, I focus on Ti_2CT_x that can deliver a large capacitance in aqueous Li^+ electrolyte due to its light molecular weight.[38] Although Ti_2CT_x (especially when delaminated) is prone to be oxidized in air or in aqueous solution,[39] stable anion-based solid-electrolyte interphase formed in a hydrate-melt system could work as a protective surface layer against this oxidation instability.[15] Furthermore, as recently demonstrated using experimental and computational methods, the hydration shell of strong Lewis acid Li^+ confined in the interlayer space of MXene has a negative dielectric constant to reduce a potential difference between an MXene electrode and charged ion, leading to the largest capacitance among various aqueous electrolytes of alkali ions (Li^+, Na^+, K^+, and Rb^+).[40]

Here, I demonstrate the high-voltage operation of an aqueous supercapacitor consisting of an MXene Ti_2CT_x electrode and a hydrate melt $Li(TFSI)_{0.7}(BETI)_{0.3}{\cdot}2H_2O$ electrolyte. Also, I examine the charge storage mechanism of peculiar high-density charge storage in Mxenes with a hydrate melt by *ex situ* XRD at different states of charge.

3.2 Synthesis and characterization of MAX phases and MXenes

Figure 3.5 shows an example of the etching process converting from the precursor Ti_2AlC MAX phase to Ti_2CT_x. The precursor MAX phase Ti_2AlC was prepared using a high-frequency induction furnace at 1350 ˚C for 1 h. Ti_2AlC have layered hexagonal structures where the Ti_2C layers (the C atoms are filled in octahedral sites between the nearly close-packed Ti layers) are interleaved by the Al layers. As Ti-C bonds are stronger than Ti-Al bonds, MXene Ti_2CT_x was synthesized by selectively removing Al layers from Ti_2AlC in LiF/HCl aqueous solution.

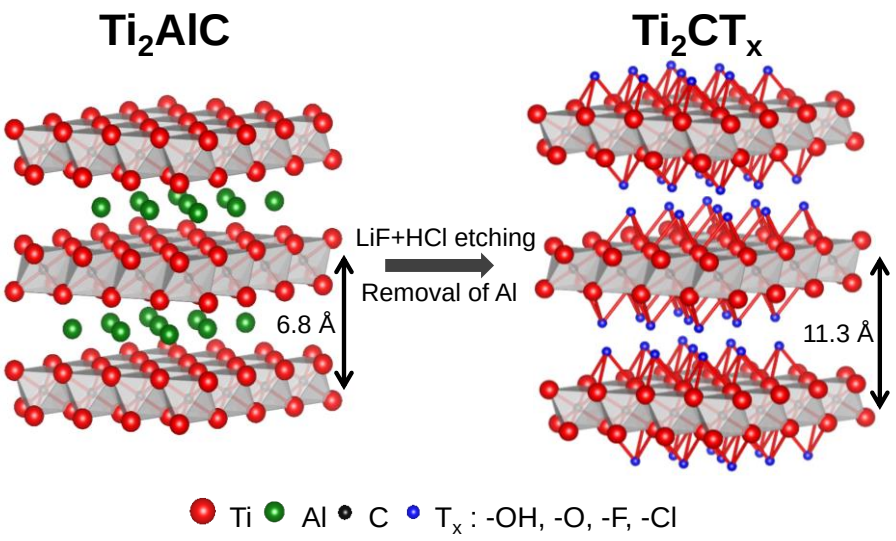

Figure 3.5 Schematic illustration of the synthesis of Ti_2CT_x. LiF/HCl treatment removes Al layer from Ti_2AlC, and a remaining Ti_2C layer is functionalized by surface termination groups such as -F, -Cl, -OH, or -O.

The X-ray diffraction (XRD) patterns of Ti_2AlC and Ti_2CT_x (**Figure 3.6a**) indicate the expansion of the interlayer distance (d_{inter}) from 6.8 (Ti_2AlC) to 11.3 Å (Ti_2CT_x) owing to surface functionalization (-OH, -O, -F, and -Cl) of the Ti_2C layer and the existence of water in the interlayer space.[41] To explore other MXenes for excellent electrochemical performances, the precursor MAX phases Nb_2AlC and Mo_2Ga_2C were first synthesized by heating at 1500 ˚C for 1 h under Ar flow (Nb_2AlC) and 850 ˚C for 48 h under vacuum-quartz (Mo_2Ga_2C), receptively. MXene Nb_2CT_x and Mo_2CT_x were synthesized by the extraction of Al layers (Nb_2AlC) and Ga layers (Mo_2Ga_2C) in LiF/HCl aqueous solutions.

Figure 3.6b shows XRD patterns of MAX phases (Nb_2AlC, Mo_2Ga_2C) and MXenes (Nb_2CT_x, Mo_2CT_x). MAX phases Nb_2AlC and Mo_2Ga_2C have well-ordered hexagonal layered structures and 020 diffraction peaks of MXenes Nb_2CT_x and Mo_2CT_x clearly shift to lower angle after the etching process, indicating the expansion of d_{inter} from 6.9 Å (Nb_2AlC) and 9.0 Å (Mo_2Ga_2C) to 10.9 Å (Nb_2CT_x) and 10.5 Å (Mo_2CT_x).

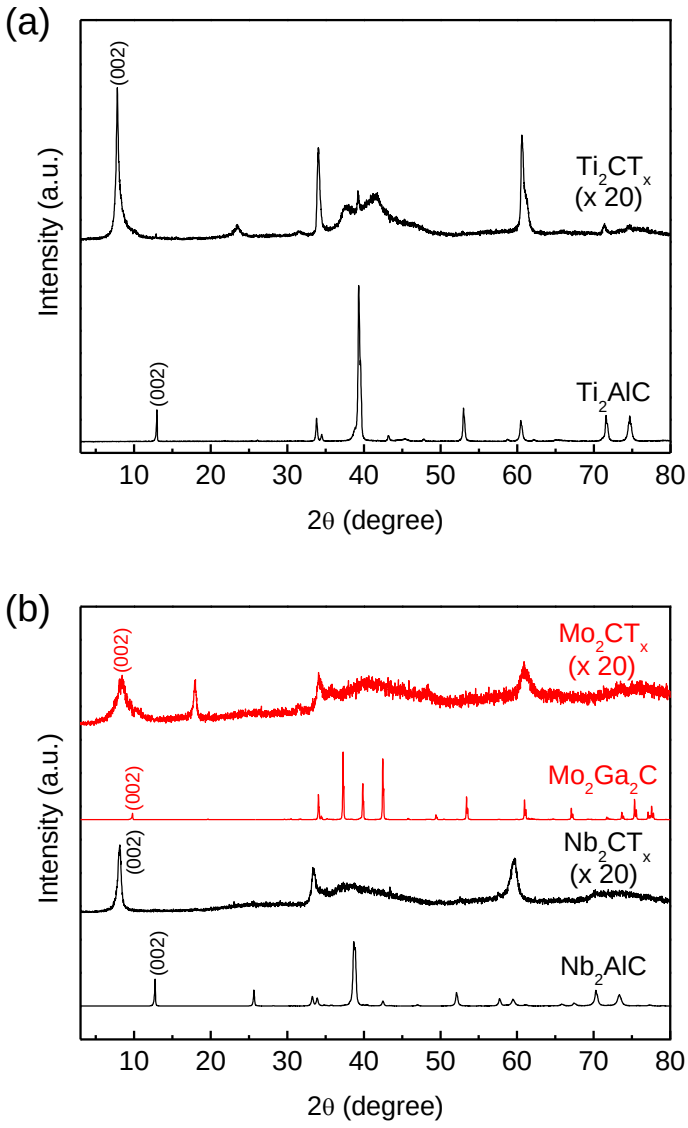

Figure 3.6 (a) XRD patterns of MAX phase Ti_2AlC and MXene Ti_2CT_x. (b) XRD patterns of MAX phases (Nb_2AlC, Mo_2Ga_2C) and MXenes (Nb_2CT_x, Mo_2CT_x). The interlayer distance increases after the transformation from MAX phases to MXenes due to the attachment of the surface termination groups.

Scanning electron microscopy indicates that MXenes (Ti_2CT_x, Nb_2CT_x, and Mo_2CT_x) have partially exfoliated morphology (**Figure 3.7**). Energy dispersive X-ray spectroscopy (EDX) analysis provides the chemical composition of MXenes (Ti_2CT_x, Nb_2CT_x, and Mo_2CT_x), indicating successful selective etching of Al layers (**Table 3.1**). All these features (XRD, SEM, and EDX) are consistent with those reported in previous literature,[31,41] supporting the successful synthesis of MXenes Ti_2CT_x, Nb_2CT_x, and Mo_2CT_x.

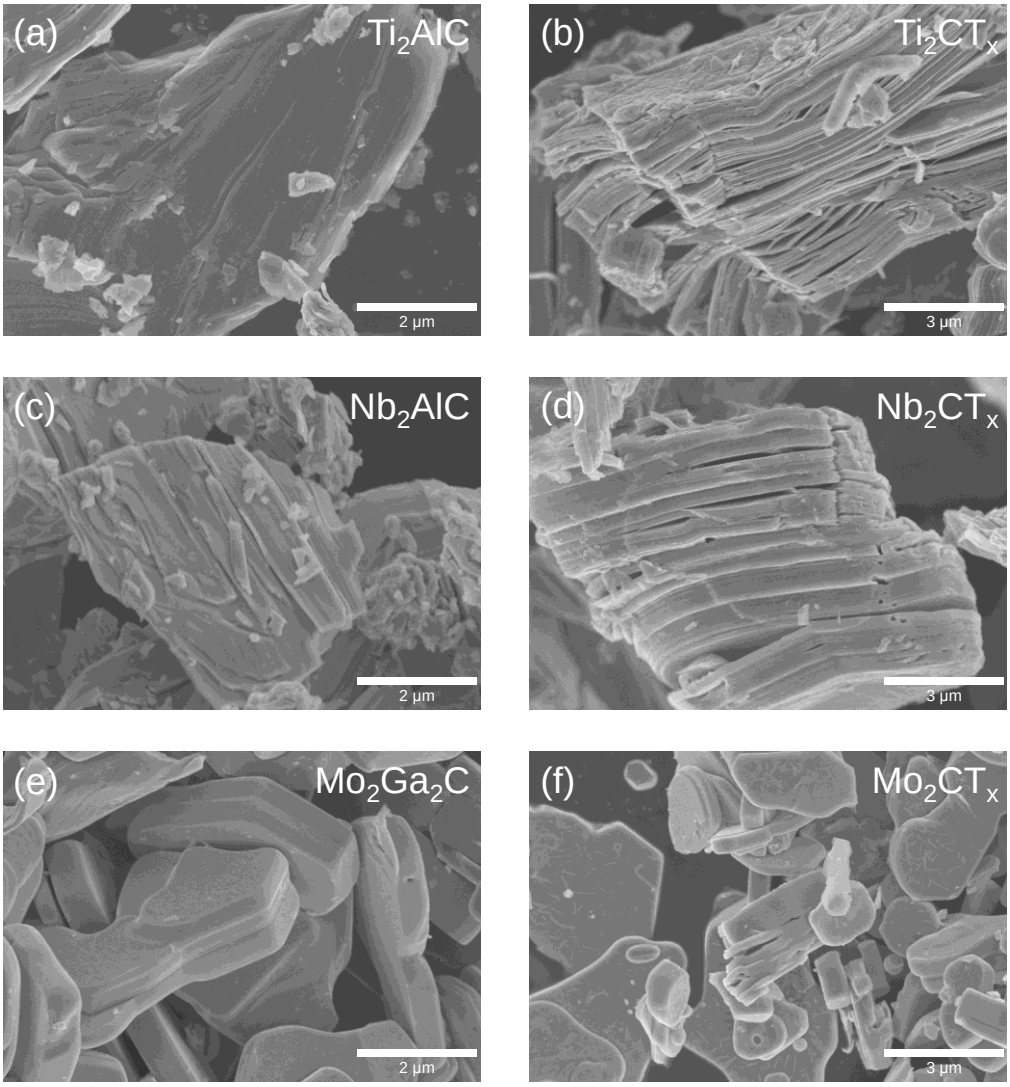

Figure 3.7 SEM images of (a) Ti_2AlC, (b) Ti_2CT_x, (c) Nb_2AlC, (d) Nb_2CT_x, (e) Mo_2Ga_2C, and (f) Mo_2CT_x. The particulate morphology of MAX phases (Ti_2AlC, Nb_2AlC, and Mo_2Ga_2C) is transformed to stacked-nanosheet morphology after LiF/HCl treatment.

Table 3.1 Energy dispersive X-ray spectroscopy analysis of MXenes (Ti_2CT_x, Nb_2CT_x, and Mo_2CT_x).

	Ti/Nb/Mo atomic%	Al/Ga atomic%	C atomic%
Ti_2CT_x	64.7	0.8	34.5
Nb_2CT_x	63.4	0.4	36.2
Mo_2CT_x	63.3	1.8	34.9

3.3 MXene electrodes with hydrate melt

The electrochemical properties of Ti_2CT_x were first examined with a conventional 1.0 M Li_2SO_4 aqueous electrolyte. Note that a hydrate-melt electrolyte with Ti and Al electrodes was reported to exhibit a low cathodic potential limit due to the formation of anion-based solid-electrolyte interphase (**Figure 3.3**).[15] Therefore, I employed the combination of Al or Ti current collector with aqueous electrolytes in this work. Chronoamperometry, **Figure 3.8**, shows a steady-state cathodic current < –10 μA/cm^2 under the applied potential of –0.9 V vs. Ag/AgCl, which indicates the electrode is already outside of the stable potential window.

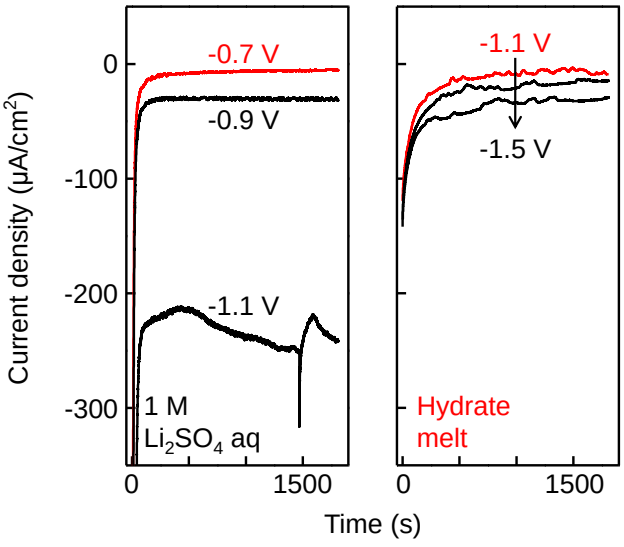

Figure 3.8 Chronoamperometry at various applied potentials vs. Ag/AgCl in a 1 M Li_2SO_4 aqueous electrolyte and a hydrate-melt electrolyte with Ti_2CT_x. Red lines indicate negligible steady-state cathodic current smaller than -10 μA/cm^2, which determines a cut-off voltage for each system.

Indeed, cathodic scan below –0.7 V in cyclic voltammetry (CV) causes an irreversible current flow due to hydrogen evolution reaction (black line in **Figure 3.9**). On the other hand, the Ti_2CT_x electrode in a hydrate-melt electrolyte showed more tolerance to the cathodic potential; it was a potential below –1.3 V that begins to induce cathodic current < –10 μA/cm^2 (**Figure 3.8**). Therefore, CV at a scan rate of 0.5 mV/s stably exhibits a distorted rectangular CV curve in a much wider electrochemical window down to −1.1 V vs. OCP (red line in **Figure 3.9**). The averaged gravimetric capacitance of the hydrate-melt electrolyte is 168 F/g, which is slightly greater than that of the 1.0 M Li_2SO_4 aqueous electrolyte (158 F/g). The slight difference between the CV curve shapes should arise from the difference in a rate-determining step (*e.g.*, low conductivity/slow ion diffusion of hydrate melt for a hydrate-melt system while low electronic conductivity/slow ion diffusion of Ti_2CT_x for a 1.0 M Li_2SO_4 system). Note that viscosities were 1.5 and 202.5 mPa·s for 1.0 M Li_2SO_4 and hydrate melt, and ionic conductivities were 61.2 and 2.8 mS/cm for 1.0 M Li_2SO_4 and hydrate melt.

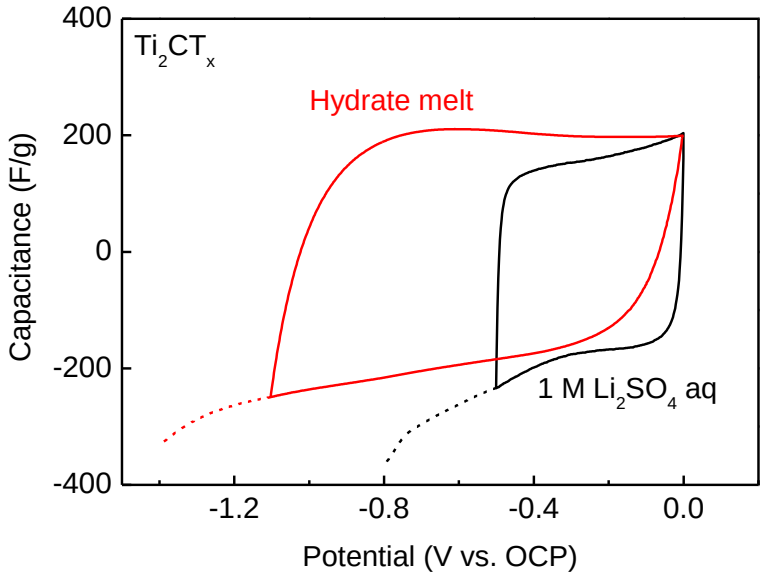

Figure 3.9 Cyclic voltammogram of Ti_2CT_x with a 1.0 M Li_2SO_4 aqueous electrolyte (black line) and a hydrate-melt electrolyte (red line) at a scan rate of 0.5 mV/s. Open circuit potentials (OCP) are −0.2 V vs. Ag/AgCl for a 1.0 M Li_2SO_4 aqueous electrolyte and 0.0 V vs. Ag/AgCl for a hydrate melt electrolyte, respectively. Dotted lines show linear sweep voltammetry curves for a cathodic scan exceeding the stable electrochemical window.

Cyclic voltammetry curves of Nb_2CT_x and Mo_2CT_x with a 1 M Li_2SO_4 and a hydrate melt aqueous electrolytes have also been screened as shown in **Figure 3.10**. Nb_2CT_x and Mo_2CT_x electrodes in a hydrate-melt electrolyte showed wider electrochemical potential windows than those of 1 M Li_2SO_4 aqueous electrolyte. The averaged gravimetric capacitances of the hydrate-melt electrolyte are 106 F/g (Nb_2CT_x) and 82 F/g (Mo_2CT_x), which are slightly greater than those of the 1.0 M Li_2SO_4 aqueous electrolyte (101 F/g for Nb_2CT_x and 80 F/g for Mo_2CT_x). Finally, Ti_2CT_x/hydrate-melt system with the highest gravimetric capacitance was decided for further studies.

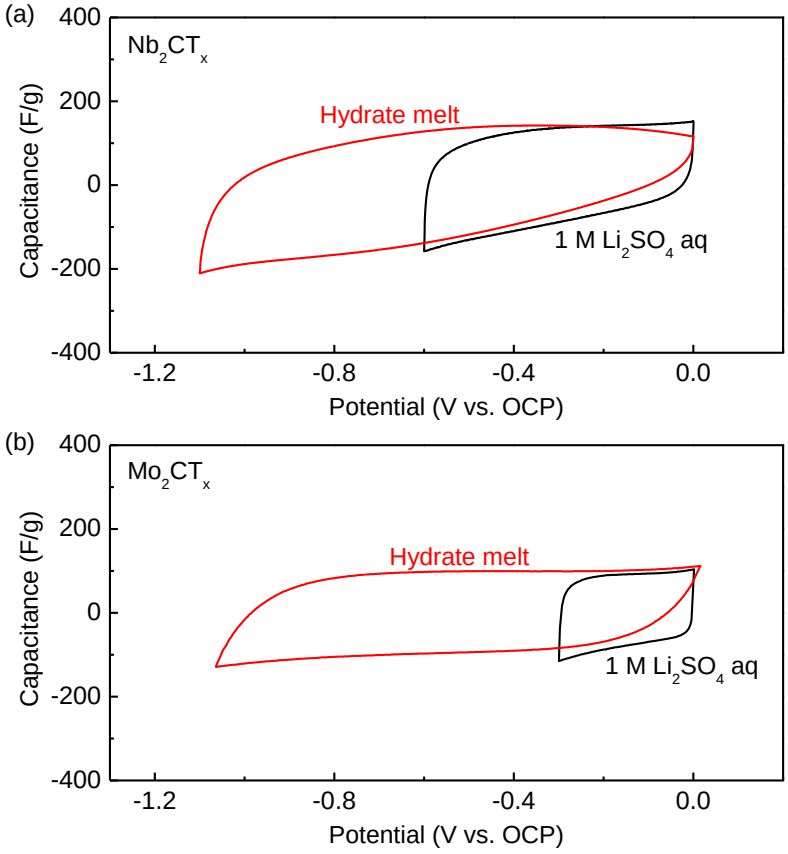

Figure 3.10 Cyclic voltammograms of (a) Nb_2CT_x and (b) Mo_2CT_x with a 1.0 M Li_2SO_4 aqueous electrolyte (black line) and a hydrate-melt electrolyte (red line) at a scan rate of 0.5 mV/s. Open circuit potentials (OCP) are −0.1 V (Nb_2CT_x) and -0.2 V (Mo_2CT_x) vs. Ag/AgCl for a 1.0 M Li_2SO_4 aqueous electrolyte and 0.2 V (Nb_2CT_x) and 0.5 V (Mo_2CT_x) vs. Ag/AgCl for a hydrate melt electrolyte, respectively.

To further evaluate the charge storage ability of the Ti_2CT_x/hydrate-melt system, I conducted galvanostatic charge/discharge experiments at various specific currents of 0.1−1.0 A/g (**Figure 3.11**). The Ti_2CT_x electrodes with the two types of aqueous electrolytes exhibit sloping potential profiles (**Figures 3.11 and 3.12**), which are consistent with the rectangular CV curves.

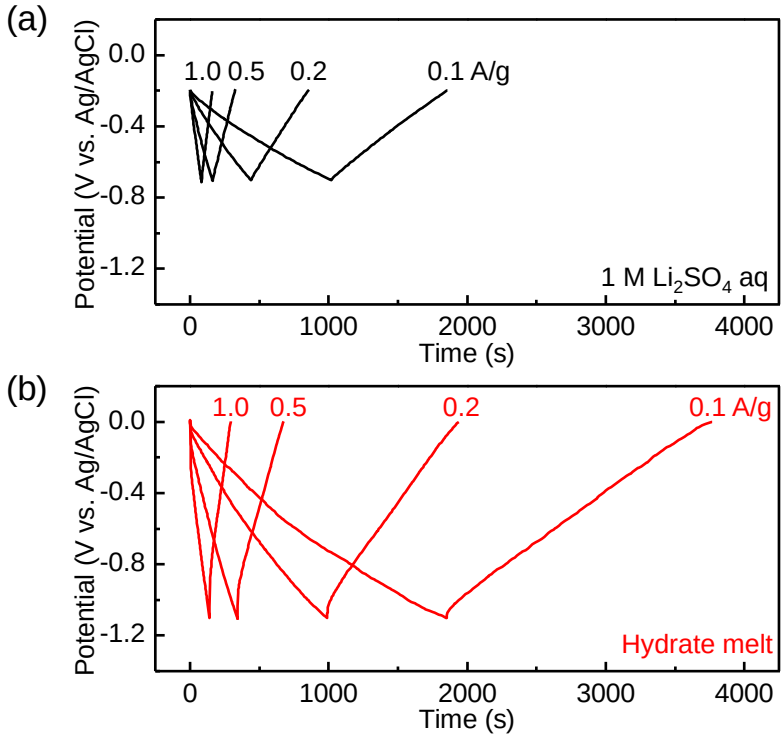

Figure 3.11 Galvanostatic charge/discharge curves of Ti_2CT_x at various specific currents of 0.1–1.0 A/g with (a) a 1.0 M Li_2SO_4 aqueous electrolyte, and (b) a hydrate-melt electrolyte.

However, owing to the wide electrochemical window, the reversible capacity with a hydrate melt electrolyte exceeds 45 mAh/g at a specific current of 200 mA/g, which is much larger than that with a 1.0 M Li_2SO_4 aqueous electrolyte (20 mAh/g) as shown in **Figure 3.12**. More than 99 % of this large capacity is retained after 100 cycles for the hydrate-melt system, while the coulombic efficiency exceeds 99 % throughout the cycling. These results suggest stable operation of the Ti_2CT_x/hydrate-melt system with minimum occurrence of side reactions, such as hydrogen evolution.

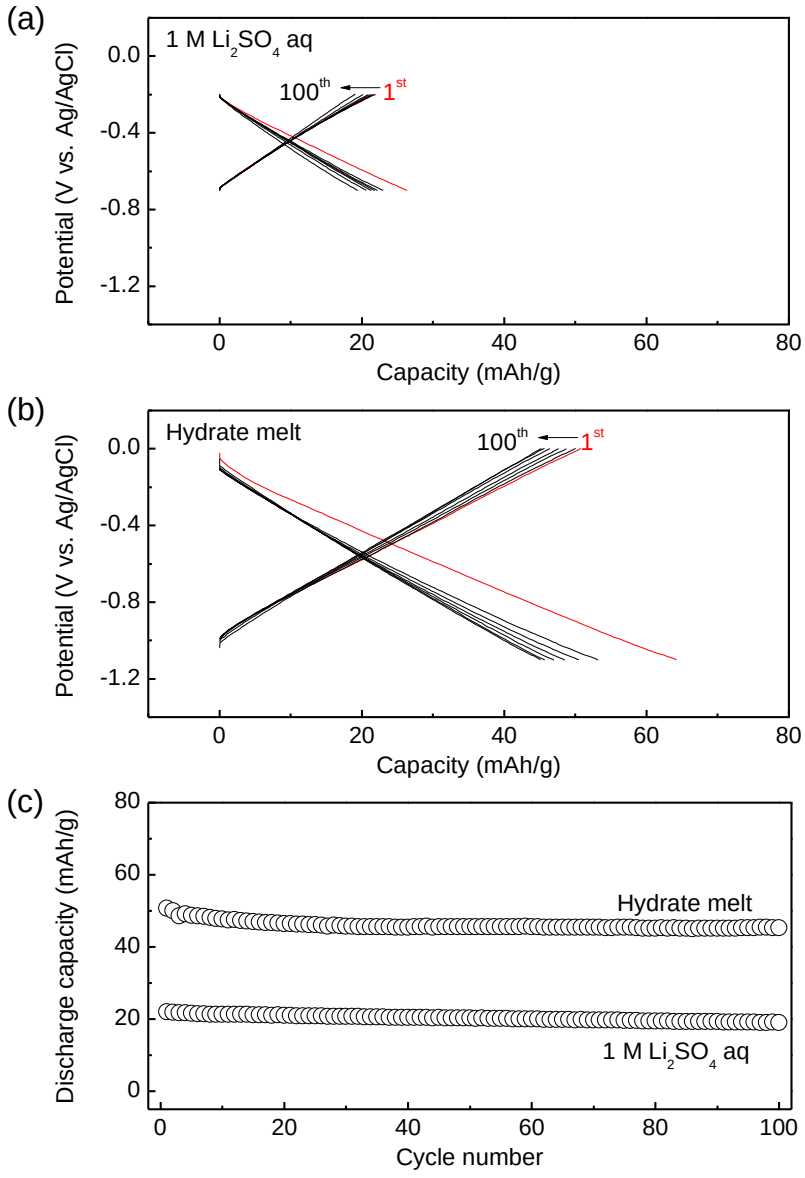

Figure 3.12 Galvanostatic charge/discharge curves of Ti_2CT_x with (a) 1.0 M Li_2SO_4 aqueous electrolyte and (b) a hydrate melt at a current rate of 0.2 A/g during 100 cycles. (c) Cycle stability of Ti_2CT_x with a 1.0 M Li_2SO_4 aqueous electrolyte and a hydrate-melt electrolyte at a specific current of 0.2 A/g.

As shown in **Figure 3.12**, initial cycle with a hydrate melt electrolyte shows a large irreversible capacity presumably due to anion-derived ($TFSI^-$ or $BETI^-$) SEI formation which can suppress the hydrogen evolution, leading to the wide cathodic potential window. Indeed, electrochemical impedance spectroscopy (**Figure 3.13a**) shows that hydrated Li^+ transfer resistance increases with cycling presumably due to SEI formation on the electrode surface. Also, anion-derived compounds (*e.g.*, LiF, Li_2S_x, SO_x, NO_x) are observed on the electrode surface after the cycling (**Figure 3.13b**). These features support the SEI formation after cycling with hydrate melt.

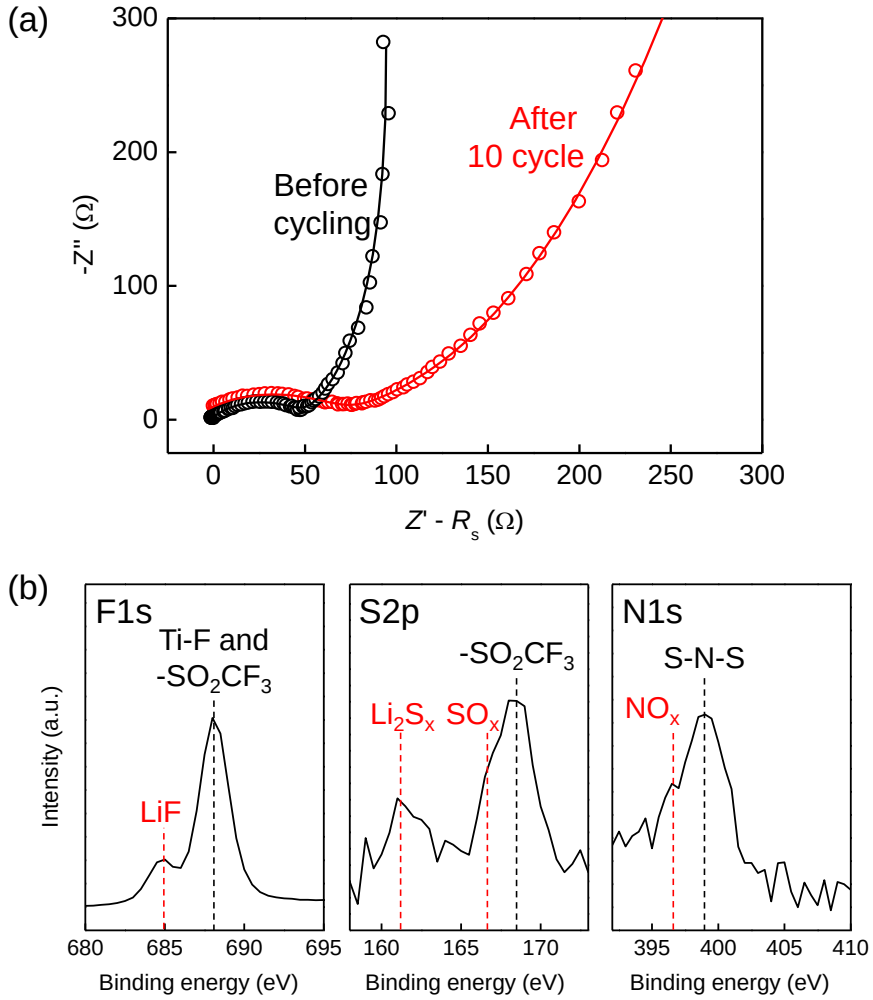

Figure 3.13. (a) Nyquist plots for Ti_2CT_x with a hydrate-melt electrolyte before cycling and after 10 cycles. Empty circles: experimental, solid lines: fitting. (b) XPS spectra of F1s, S2p, and N1s for Ti_2CT_x electrode after 10 cycles.

Anion-derived SEI suppresses the hydrogen evolution by blocking the donation of electrons from the exfoliated surface of MXene to water molecules. Besides, the electrochemical stability of a water molecule (isolated or coordinated) in the interlayer of MXene should also be considered. As shown in **Figure 3.14**, possible explanations of the enhanced electrochemical stability of the water molecules in MXene interlayer are: (1) lower electric conductivity in basal plane (transition-metal-surface group (-F, -Cl, -O, and -OH)) than on edge (transition-metal carbide core), (2) high electronegativity of surface group (*e.g.*, -F), and (3) thin SEI formation by the reaction between surface group and intercalated-Li ion (*e.g.*, LiF, Li_2O). Indeed, many researchers reported that edge sites play a critical role for the HER.[42] In addition, it was reported that HER is suppressed with higher electronegativity of the surface group.[43]

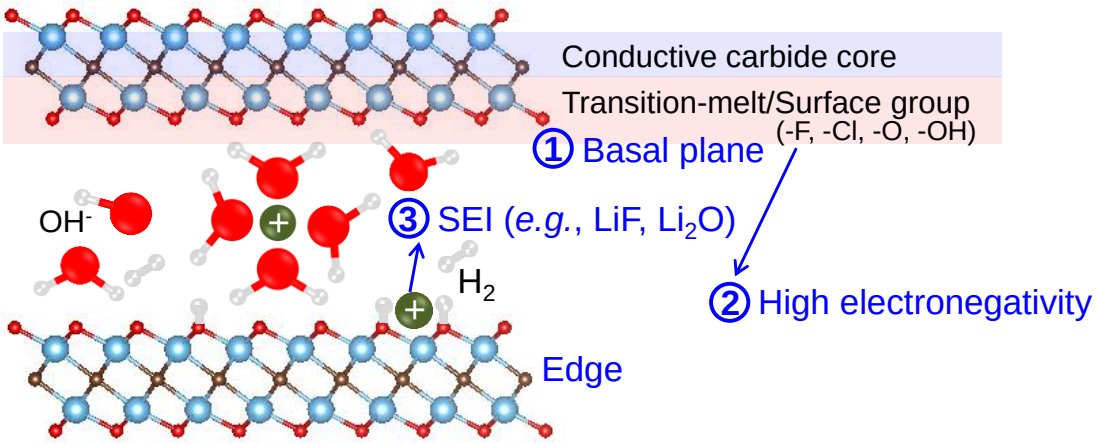

Figure 3.14. Schematic design of MXene interlayer. Electrochemical stability of water molecules in MXene interlayer can be enhanced by: (1) low electric conductivity of basal plane, (2) high electronegativity of surface group, and (3) SEI formation.

Based on the capacities at slow current rate of 30 mA/g as shown in **Figure 3.15a**, the intercalation amounts of Li^+ were calculated; hydrate melt provides $0.33Li^+$ intercalation in $Ti_2CT_x \cdot nH_2O$ while 1 M Li_2SO_4 aqueous electrolyte offers $0.11Li^+$ in $Ti_2CT_x \cdot nH_2O$. For comparison, theoretical capacity of $Ti_2CT_x \cdot nH_2O$ was predicted, assuming that hydrated Li^+ are close-packed (no Coulombic force each other) in MXene interlayer as shown in **Figure 3.15b**. Lattice parameters of $Ti_2CT_x \cdot nH_2O$ were obtained from XRD analysis and radius of hydrate (4-coordinated) Li^+ is 2.082 Å.[44] Theoretical capacity of $Ti_2CT_x \cdot nH_2O$ with hydrated Li^+ exhibits $Li_{0.46}Ti_2CT_x \cdot nH_2O$ (80 mAh/g), which is slightly higher than the experimental value with a hydrate melt ($Li_{0.33}Ti_2CT_x \cdot nH_2O$ (60 mAh/g)). It should be noted that this theoretical value is reasonable, considering that Coulombic force occurs between hydrated Li^+. Therefore, a hydrate melt with wide cathodic potential window could provide dense charge accumulation in MXene electrode.

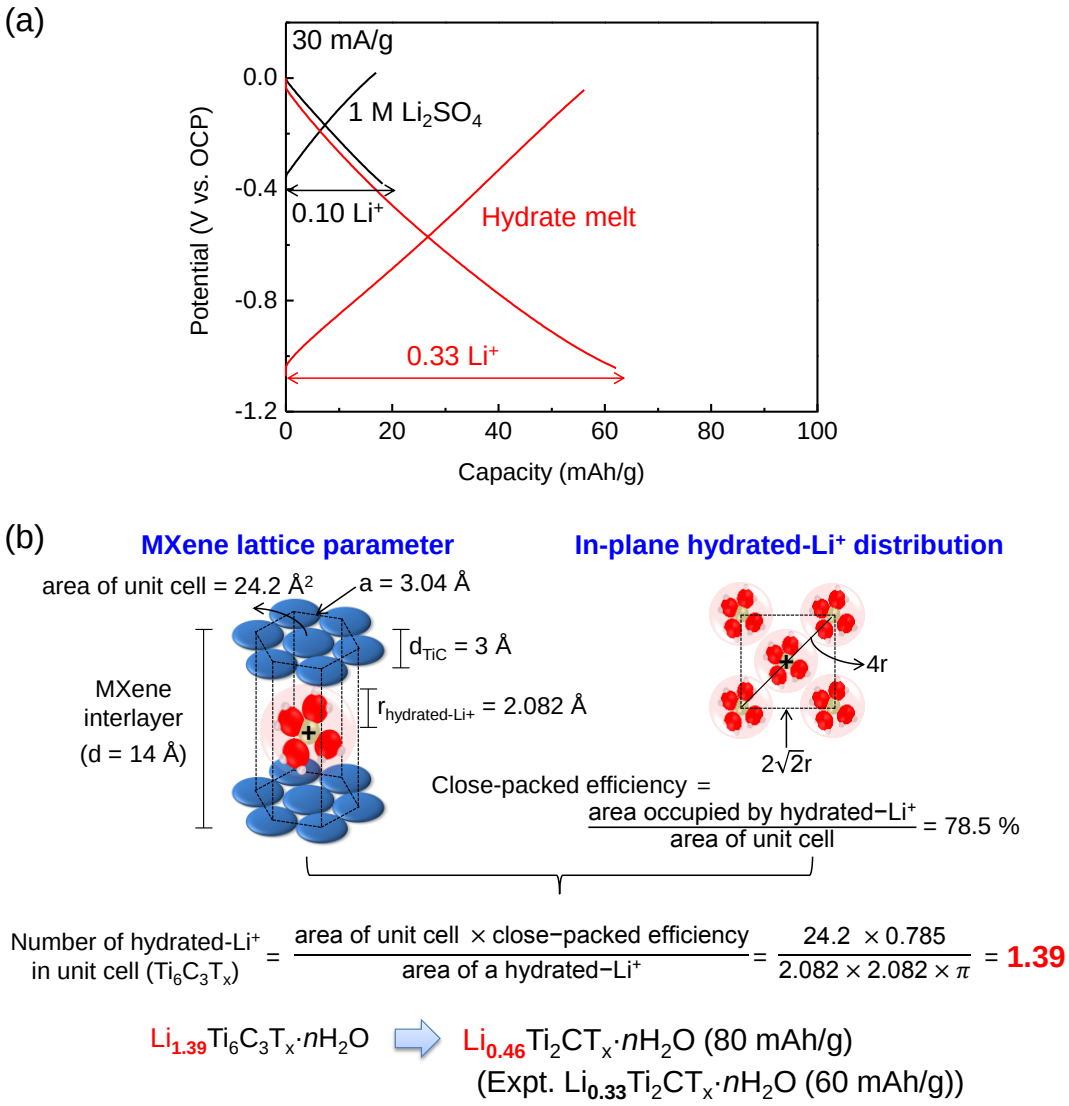

Figure 3.15. (a) Charge/discharge curves of Ti_2CT_x at a slow current rate of 30 mA/g and (b) approximate calculation of theoretical capacity of $Ti_2CT_x \cdot nH_2O$ with close-packed hydrated Li^+.

3.4 Charge storage of MXene

Having demonstrated the wide electrochemical window and the large specific capacity of the Ti_2CT_x/hydrate-melt system, I investigated the charge storage mechanism by considering the EDL structure of an MXene electrode as shown in **Figure 3.16**. The specific capacitance (C) of an EDL capacitor electrode is defined as $C = \Delta Q/\Delta E$, where ΔE is the voltage change of the electrode versus a reference electrode, and ΔQ is the stored charge per the unit weight of the electrode. As discussed above, hydrated Li^+ is intercalated into the interlayer space to form an EDL upon charging. Assuming constant chemical potentials for lithium-ion and electron in MXene, which is the case for a typical EDL capacitor electrode, C should have a linear dependence on the inverse magnitude of $(\phi_e - \phi_{Li})$, where ϕ_e and ϕ_{Li} are the inner potentials at the positions of stored electrons and Li^+, respectively.[38]

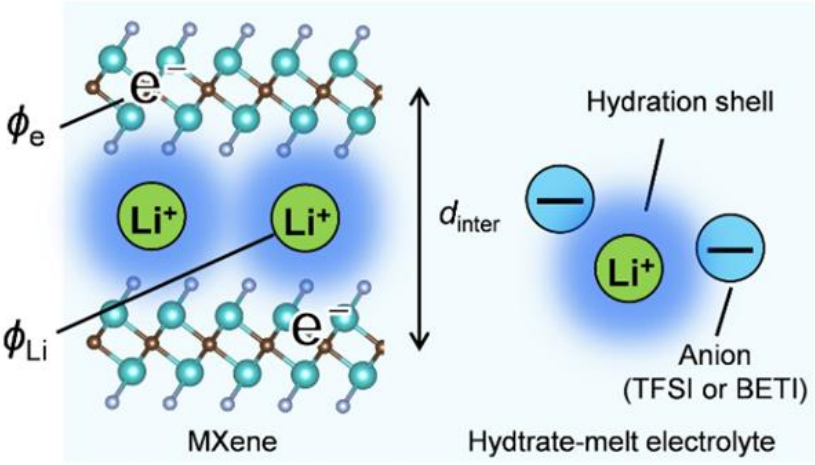

Figure 3.16 Schematic illustration of Li^+ intercalation to form an electric double-layer in MXene.

To clarify structural changes during charging and discharging, *ex-situ* XRD patterns were collected at different charge of states. The 002 diffraction pattern of Ti_2CT_x with a 1.0 M Li_2SO_4 aqueous electrolyte show a reversible shift and a reversible increase/decrease of d_{inter} by Li^+ intercalation/deintercalation (**Figure 3.17**).

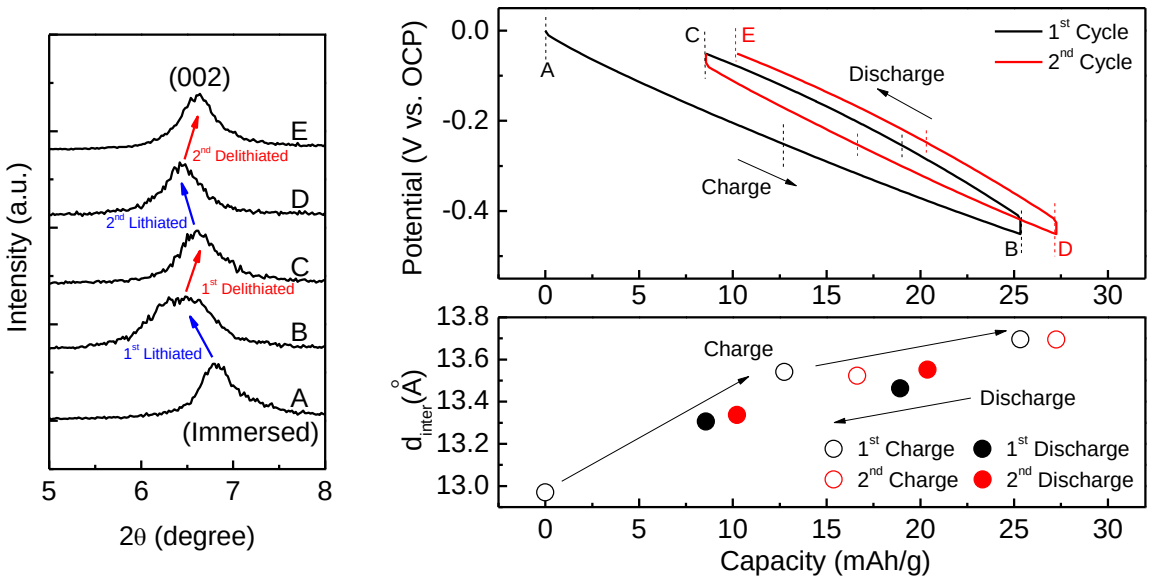

Figure 3.17 Ex-situ XRD patterns (Left), and the interlayer distance d_{inter} (right) of Ti_2CT_x upon charging/discharging with a 1.0 M Li_2SO_4 aqueous electrolyte during the first and second cycles.

The variation of d_{inter} measured with the hydrate-melt electrolyte was similar to that with the aqueous electrolyte and reversible (**Figure 3.18**). The value of d_{inter} was in the range of 13.7-14.1 Å during charge/discharge, which is much larger than the value for dehydrated Ti_2CT_x (d_{inter} = 8.7 Å). Thus, the intercalation species are not bare Li^+ but hydrated species, which form an EDL at the interlayer of MXene sheets.[38,40] These results are consistent with a report by Shpigel *et al.*[45] who observed intercalation of hydrated Li^+ into $Ti_3C_2T_x$ by *in situ* hydrodynamic spectroscopy.

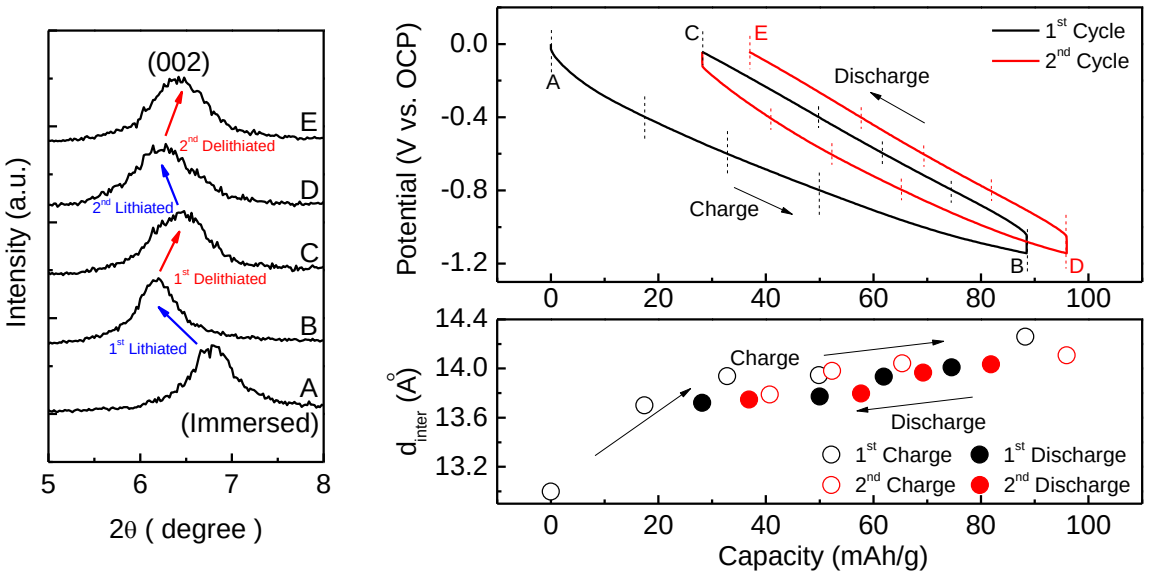

Figure 3.18 Ex-situ XRD patterns (Left), and the interlayer distance d_{inter} (right) of Ti_2CT_x upon charging/discharging with a hydrate-melt electrolyte during the first and second cycles.

3.5 MXene supercapacitor with hydrate melt

Finally, I designed high-voltage aqueous supercapacitors based on a Ti_2CT_x negative electrode, an activated carbon (AC) positive electrode, and a hydrate-melt electrolyte. Before evaluation of full-cell (Ti_2CT_x/AC), electrochemical performances of activated carbon were investigated a conventional 1.0 M Li_2SO_4 and a hydrate-melt aqueous electrolyte. Both electrolytes with a Ti current collector give no considerable current flow below 1.3 V vs. Ag/AgCl in anodic linear sweep voltammetry (**Figure 3.19a**). Therefore, I employed the Ti current collector with aqueous electrolytes for positive electrodes. Chronoamperometry (**Figure 3.19b**) shows a negligible steady-state anodic current under the applied potential of 0.4 V (1 M Li_2SO_4) and 0.9 V (hydrate melt) vs. Ag/AgCl, which indicates the stable potential window. A steady-state anodic current under anodic polarization is significantly suppressed on the activated carbon electrode by using a hydrate-melt electrolyte as compared to that observed in a 1.0 M Li_2SO_4 aqueous electrolyte.

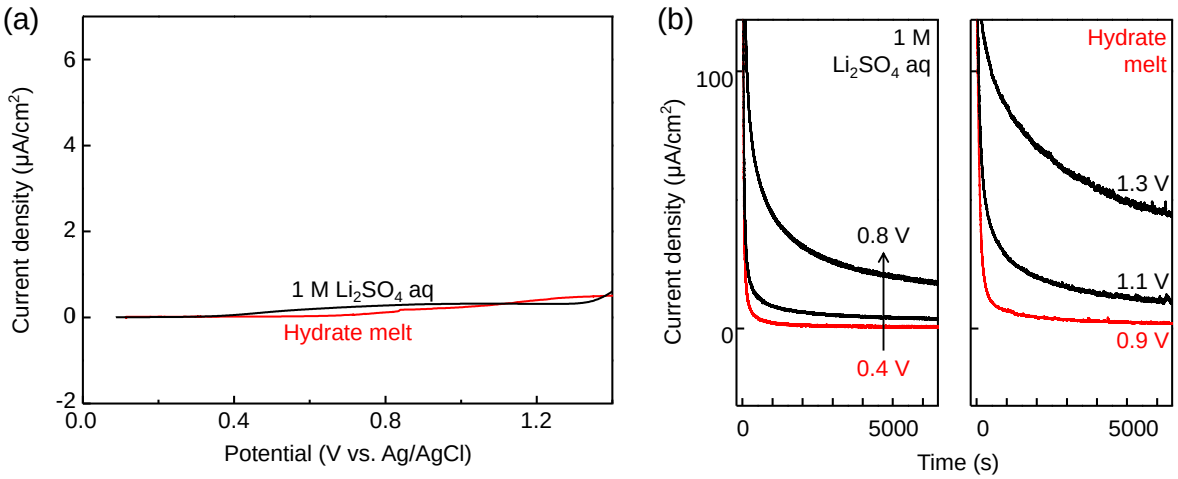

Figure 3.19 (a) Anodic linear sweep voltammetry of a 1 M Li_2SO_4 aqueous electrolyte and a hydrate-melt electrolyte with a Ti electrode at a sweep rate of 0.1 mV/s. (b) Chronoamperometry at various applied potentials vs. Ag/AgCl in a 1 M Li_2SO_4 aqueous electrolyte and a hydrate-melt electrolyte with activated carbon. Red lines indicate negligible steady-state anodic current, which determines a cut-off voltage for each system.

The hydrate-melt electrolyte also improves the anodic limit of an activated carbon electrode from 0.25 V (1.0 M Li_2SO_4 aqueous electrolyte) to 0.9 V vs. OCP (**Figure 3.20**) to ensure the stable cycle operation. The averaged gravimetric capacitance of activated carbon with the hydrate-melt electrolyte is 127 F/g, which is slightly smaller than that of the 1.0 M Li_2SO_4 aqueous electrolyte presumably due to low ionic conductivity of the hydrate-melt electrolyte (138 F/g).

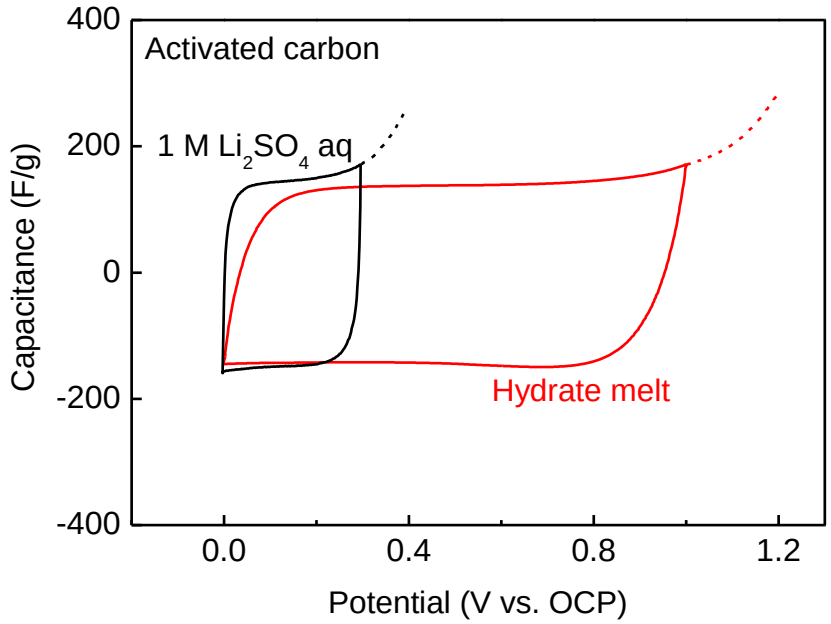

Figure 3.20 Cyclic voltammetry curves of activated carbon with a 1.0 M Li_2SO_4 aqueous electrolyte (black line) and a hydrate-melt electrolyte (red line) at a scan rate of 0.5 mV/s. Open circuit potentials (OCP) are 0.15 V vs. Ag/AgCl for a 1.0 M Li_2SO_4 aqueous electrolyte and −0.05 V vs. Ag/AgCl for the hydrate-melt electrolyte, respectively. Dotted lines are linear sweep voltammetry curves for a cathodic scan exceeding a stable electrochemical window.

Owing to this wide electrochemical window, the AC/hydrate-melt positive electrode system delivers a specific capacity of 38 mAh/g at a specific current of 30 mA/g, which is much larger than that obtained for the activated carbon/1.0 M Li_2SO_4 system (**Figures 3.21**).

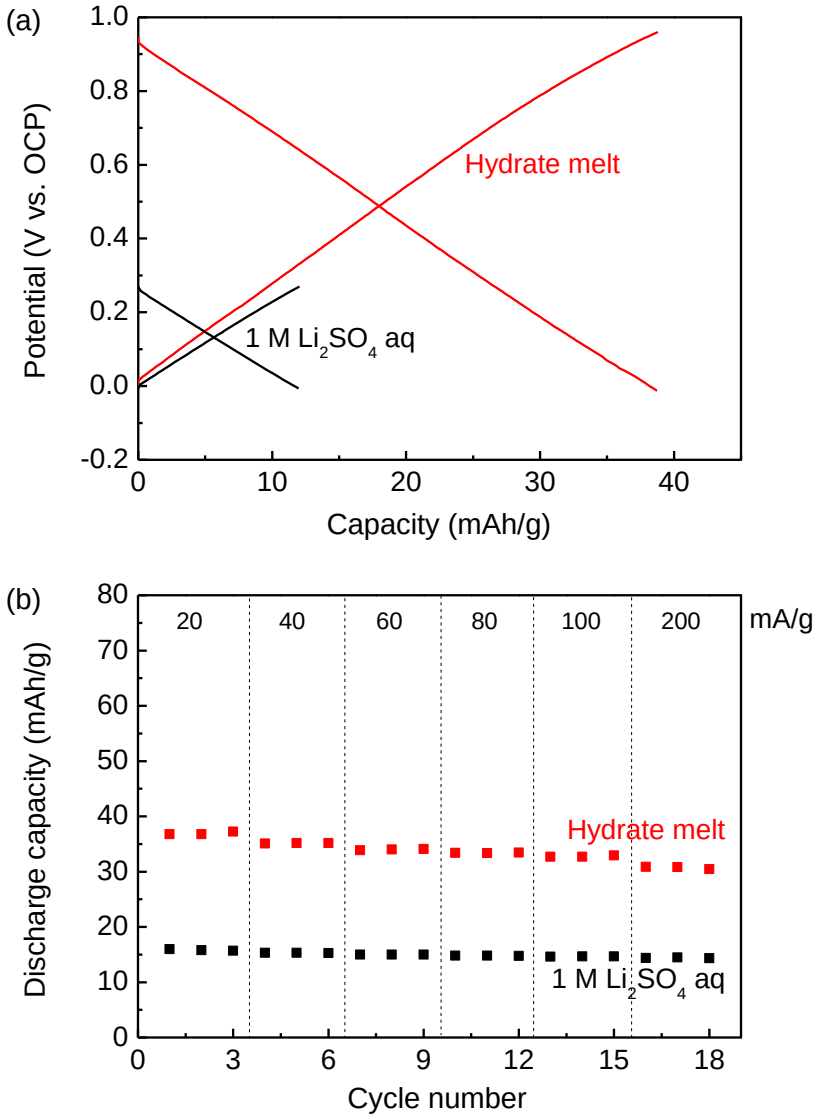

Figure 3.21 (a) Galvanostatic charge/discharge curves of activated carbon at a constant specific current of 30 mA/g with a 1.0 M Li_2SO_4 aqueous electrolyte (black lines), and with a hydrate-melt electrolyte (red lines). (b) Rate capability of activated carbon at various specific currents of 20-200 mA/g with a 1.0 M Li_2SO_4 aqueous electrolyte (black) and with a hydrate-melt electrolyte (red).

Then, I fabricated a full cell (Ti_2CT_x|hydrate melt|AC) with a capacity-balanced configuration (**Figure 3.22a**). As shown in **Figure 3.22b**, after a small irreversible capacity during initial cycles, the full cell delivers a specific capacity of 45 mAh/g and a high averaged coulombic efficiency over 99 % at a current rate of 100 mA/g for 1000 cycles. Stable operation is achieved at a maximum voltage of 2 V.

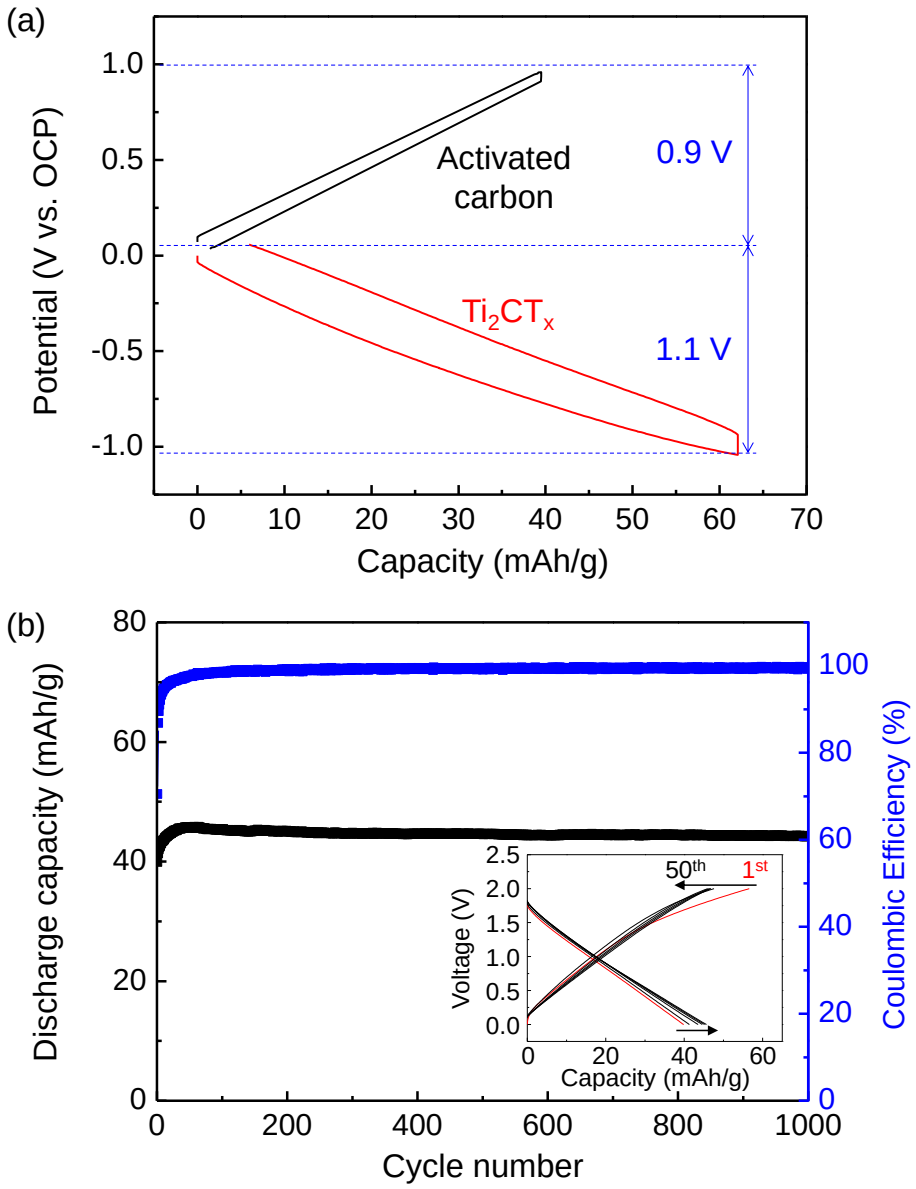

Figure 3.22 (a) Potential profiles of activated carbon and Ti_2CT_x in a hydrate-melt electrolyte at a specific current of 30 mA/g during the second cycle. (b) Voltage profiles of a capacity-balanced full-cell consisting of a Ti_2CT_x negative electrode and an activated carbon positive electrode with a hydrate-melt electrolyte. Cell was cycled at a specific current of 100 mA/g in the voltage range of 2.0 – 0.0 V. Inset shows the cycle stability during 1000 cycles. The capacity value of full-cell is based on the weight of Ti_2CT_x.

The rate capability tests for the full cell (**Figure 3.23**) show that the application of a hydrate-melt electrolyte to a suitable electrode can greatly enhance the total performance of capacitor devices. Although the performance (*ca.*, 10 Wh/kg at 100 W/kg) is limited in part due to the small capacitance of the AC electrode and the low conductivity of the electrolyte and is less than those of aqueous capacitors reported previously (*e.g.*, 104 Wh/kg at 1.27 kW/kg for $NiMoO_4$|2.5 M KOH/H_2O|FeOOH or 40 Wh/kg at 17.4 kW/kg for Mn_5O_8|0.1 M Na_2SO_4/H_2O|Mn_5O_8, 30 Wh/kg at 100 W/kg for $Ti_3C_2T_x$|1.0 M Li_2SO_4/H_2O|$LiMn_2O_4$, or 15 Wh/kg at 1 kW/kg for AC|31.3 m LiTFSI/H_2O|AC),[21,46-48] the use of a hydrate-melt electrolyte can expand the materials candidate that would otherwise cause hydrogen/oxygen generation at less reductive/oxidative conditions and could be a general strategy toward improving the performance of aqueous supercapacitors.

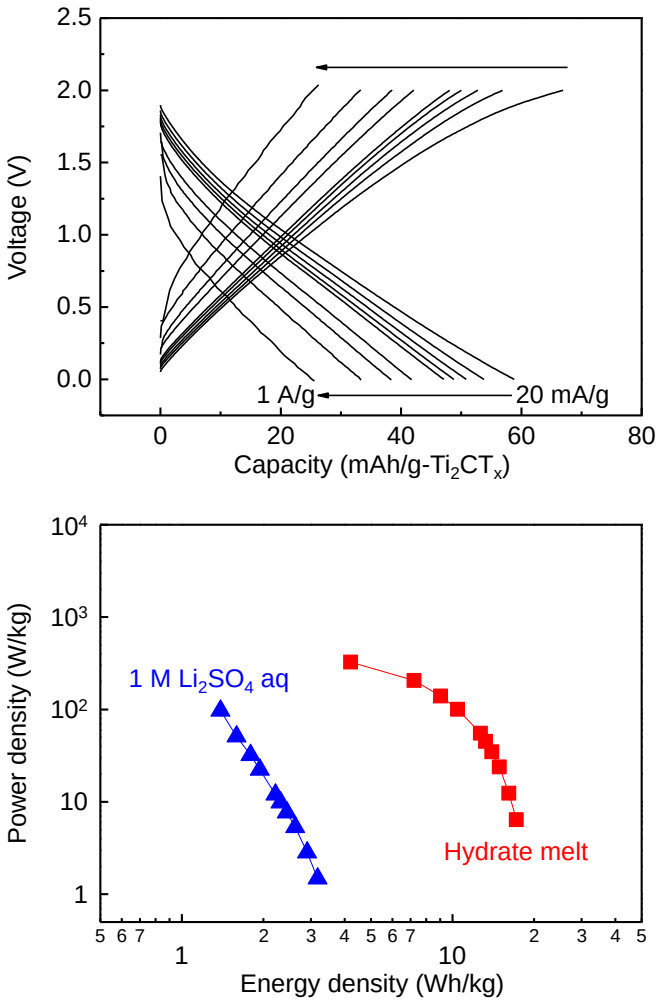

Figure 3.23 (a) Rate capability with various specific currents. The capacity value is based on the weight of Ti_2CT_x. (b) Ragone plots of the Ti_2CT_x/AC full-cell with a hydrate-melt electrolyte (empty squares) and a 1.0 M Li_2SO_4 aqueous electrolyte (filled circles). The energy and power density values are based on the weight of total active materials (Ti_2CT_x and activated carbon).

3.6 Conclusion

To realize high energy and power aqueous supercapacitors, electrochemical properties of MXene electrode were investigated with a hydrate melt electrolyte, which can provide exceptionally wide electrochemical window of -1.1 V vs. Ag/AgCl. MXene electrode with a hydrate melt exhibited a capacity of 60 mAh/g at a current rate of 30 mA/g three times higher than that of a commercial 1 M Li_2SO_4 aqueous electrolyte. Capacity retention of Ti_2CT_x with a hydrate-melt system showed more than 99 % after 100 cycles, while the coulombic efficiency exceeds 99 % throughout the cycling. These results of the Ti_2CT_x/hydrate-melt system suggest wider potential operation to the cathodic direction with minimum occurrence of side reactions such as hydrogen evolution, compared to other references (*e.g.*, AC/0.5 M Na_2SO_4, AC/2.0 M Li_2SO_4, and RuO_2/1.0 M Na_2SO_4) as shown in **Figure 3.24**.[13,49,50]

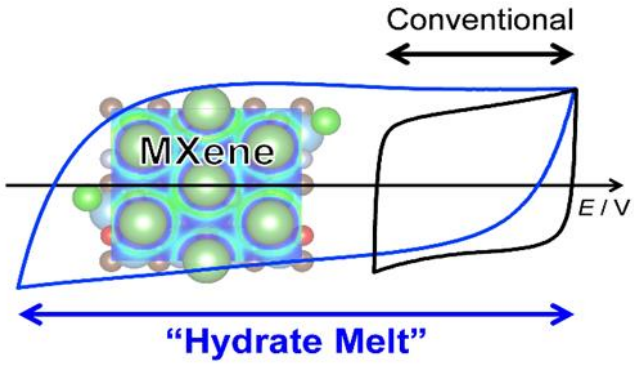

Figure 3.24 Schematic design of wide electrochemical potential window obtained from CV for a MXene/hydrate melt system.

The wide potential window of a hydrate melt electrolyte realizes unprecedented high-density intercalation of hydrated Li^+ in the interlayer space of MXene, where the hydration shells of neighboring Li^+ ions are closely packed and overlap with each other. Such a high-density charge accumulation can induce an anomalous pseudocapacitance of Ti_2CT_x at the lower potential region. The electrochemical performance of a full cell (Ti_2CT_x|hydrate melt|AC) showed a capacity of 45 mAh/g at a current rate of 100 mA/g while cycle retention presented approximately 100 % after 1000 cycles. To further enhance energy density, high-performance cathode materials (*e.g.*, MnO_2) are suggested. This work demonstrates that the application of hydrate-melt electrolytes can provide a new platform for designing advanced energy storage systems.

Reference

(1) Simon, P.; Gogotsi, Y. Materials for Electrochemical Capacitors. *Nat. Mater.* **2008**, *7*, 845-854.

(2) Wang, G.; Zhang, L.; Zhang, J. A Review of Electrode Materials for Electrochemical Supercapacitors. *Chem. Soc. Rev.* **2012**, *41*, 797-828.

(3) González, A.; Goikolea, E.; Barrena J. A.; Mysyk R. Review on Supercapacitors: Technologies and Materials. *Renew. Sust. Energ. Rev.* **2016**, *58*, 1189-1206.

(4) Chen, S.-M.; Ramachandran, R.; Mani, V.; Saraswathi, R. Recent Advancements in Electrode Materials for the High-Performance Electrochemical Supercapacitors: A Review. *Int. J. Electrochem. Sci.* **2014**, *9*, 4072-4085.

(5) Zhang, L. L.; Zhao, X. S. Carbon-Based Materials as Supercapacitor Electrodes. *Chem. Soc. Rev.* **2009**, *38*, 2520-2531.

(6) Simon, P.; Gogotsi Y.; Dunn, B. Where Do Batteries End and Supercapacitors Begin?. *Science* **2014**, *343*, 1210-1211.

(7) Liu, C.; Yu, Z.; Neff, D.; Zhamu, A.; Jang, B. Z. Graphene-Based Supercapacitor with an Ultrahigh Energy Density. *Nano Lett.* **2010**, *10*, 4863-4868.

(8) Qi, D.; Liu, Y.; Liu, Z.; Zhang, L.; Chen, X. Design of Architectures and Materials in In-Plane Micro-Supercapacitors: Current Status and Future Challenges. *Adv. Mater.* **2017**, *29*, 1602802.

(9) Kötz, R.; Carlen, M. Principles and Applications of Electrochemical Capacitors. *Electrochim. Acta* **2000**, *45*, 2483-2498.

(10) Chang, Z.; Yang, Y.; Li, M.; Wang, X.; Wu, Y. Green Energy Storage Chemistries Based on Neutral Aqueous Electrolytes. *J. Mater. Chem. A* **2014**, *2*, 10739-10755.

(11) Zhong, C.; Deng, Y.; Hu, W.; Qiao, J.; Zhang, L.; Zhang, J. A Review of Electrolyte Materials and Compositions for Electrochemical Supercapacitors. *Chem. Soc. Rev.* **2015**, *44*, 7484-7539.

(12) Wang, Y.; Yi, J.; Xia, Y. Recent Progress in Aqueous Lithium-Ion Batteries. *Adv. Energy Mater.* **2012**, *2*, 830-840.

(13) Demarconnay, L.; Raymundo-Piñero, E.; Béguin, F. A Symmetric Carbon/Carbon Supercapacitor Operating at 1.6 V by Using a Neutral Aqueous Solution. *Electrochem. Commun.*

2010, *12*, 1275-1278.

(14) Demarconnay, L.; Raymundo-Piñero, E.; Béguin, F. Adjustment of Electrodes Potential Window in an Asymmetric Carbon/MnO_2 Supercapacitor. *J. Power Sources* **2011**, *196*, 580-586.

(15) Yamada, Y.; Usui, K.; Sodeyama, K.; Ko, S.; Tateyama, Y.; Yamada, A. Hydrate-Melt Electrolytes for High-Energy-Density Aqueous Batteries. *Nat. Energy* **2016**, *1*, 16129.

(16) Suo, L.; Borodin, O.; Gao, T.; Olguin, M.; Ho, J.; Fan, X.; Luo, C.; Wang, C.; Xu, K. "Water-in-Salt" Electrolyte Enables High-Voltage Aqueous Lithium-Ion Chemistries. *Science* **2015**, *350*, 938-943.

(17) Wang, F.; Suo, L.; Liang, Y.; Yang, C.; Han, F.; Gao, T.; Sun, W.; Wang, C. Spinel $LiNi_{0.5}Mn_{1.5}O_4$ Cathode for High-Energy Aqueous Lithium-Ion Batteries. *Adv. Energy Mater.* **2017**, *7*, 1600922.

(18) Suo, L.; Borodin, O.; Sun, W.; Fan, X.; Yang, C.; Wang, F.; Gao, T.; Ma, Z.; Schroeder, M.; Cresce, A. V.; Russell, S. M.; Armand, M.; Angell, A.; Xu, K.; Wang, C. Advanced High-Voltage Aqueous Lithium-Ion Battery Enabled by "Water-In-Bisalt" Electrolyte. *Angew. Chem.* **2016**, *128*, 7252-7257.

(19) Sheng, K.; Sun, Y.; Li, C.; Yuan, W.; Shi, G. Ultrahigh-Rate Supercapacitors Based on Electrochemically Reduced Graphene Oxide for Ac Line-Filtering, *Sci. Rep.* **2012**, *2*, 247.

(20) Hasegawa, G.; Kanamori, K.; Kiyomura, T.; Kurata, H.; Abe, T.; Nakanishi, K. Hierarchically Porous Carbon Monoliths for High-Voltage Aqueous Supercapacitors. *Chem. Mater.* **2016**, *28*, 3944-3950.

(21) Lannelongue, P.; Bouchal, R.; Mourad, E.; Bodin, C.; Olarte, M.; le Vot, S.; Favier, F.; Fontaine, O. "Water-In-Salt" for Supercapacitors: A Compromise between Voltage, Power Density, Energy Density and Stability. *J. Electrochem. Soc.* **2018**, *165*, A657-A663.

(22) Zhang, M.; Makino, S.; Mochizuki, D.; Sugimito, W. High-Performance Hybrid Supercapacitors Enabled by Protected Lithium Negative Electrode and "Water-In-Salt" Electrolyte. *J. Power Sources* **2018**, *396*, 498-505.

(23) Krummacher, J.; Balducci, A. $Al(TFSI)_3$ as a Conducting Salt for High-Voltage Electrochemical Double-Layer Capacitors. *Chem. Mater.* **2018**, *30*, 4857-4863.

(24) Dou, Q.; Lei, S.; Wang, D. W.; Zhang, Q.; Xiao, D.; Guo, H.; Wang, A.; Yang, H.; Li, Y.; Shi, S.; Yan, X. Safe and High-Rate Supercapacitors Based on An "Acetonitrile/Water-In-Salt" Hybrid Electrolyte. *Energy Environ. Sci.* **2018**, *11*, 3212-3219.

(25) Lukatskaya, M. R.; Feldblyum, J. I.; Mackanic, D. G.; Lissel, F.; Michels, D. L.; Cui, Y.; Bao, Z. Concentrated Mixed Cation Acetate "Water-In-Salt" Solutions as Green and Low-Cost High Voltage Electrolytes for Aqueous Batteries. *Energy Environ. Sci.* **2018**, *11*, 2876-2883.

(26) Naguib, M.; Kurtoglu, M.; Presser, V.; Lu, J.; Niu, J.; Heon, M.; Hultman, L.; Gogotsi, Y.; Barsoum, M. W. Two-Dimensional Nanocrystals Produced by Exfoliation of Ti_3AlC_2. *Adv. Mater.* **2011**, *23*, 4248-4253.

(27) Naguib, M.; Come, J.; Dyatkin, B.; Presser, V.; Taberna, P.-L.; Simon, P.; Barsoum, M. W.; Gogotsi, Y. MXene: A Promising Transition Metal Carbide Anode for Lithium-Ion Batteries. *Electrochem. Commun.* **2012**, *16*, 61-64.

(28) Naguib, M.; Mashtalir, O.; Carle, J.; Presser, V.; Lu, J.; Hultman, L.; Gogotsi, Y.; Barsoum, M. W. Two-Dimensional Transition Metal Carbides. *ACS Nano* **2012**, *6*, 1322-1331.

(29) Lukatskaya, M. R.; Mashtalir, O.; Ren, C. E.; Dall'Agnese, Y.; Rozier, P.; Taberna, P. L.; Naguib, M.; Simon, P.; Barsoum, M. W.; Gogotsi, Y. Cation Intercalation and High Volumetric Capacitance of Two-Dimensional Titanium Carbide. *Science* **2013**, *341*, 1502-1505.

(30) Naguib, M.; Mochalin, V. N.; Barsoum, M. W.; Gogotsi, Y. 25^{th} Anniversary Article: MXenes: A New Family of Two-Dimensional Materials. *Adv. Mater.* **2014**, *26*, 992-1005.

(31) Ghidiu, M.; Lukatskaya, M. R.; Zhao, M.-Q.; Gogotsi, Y.; Barsoum, M. W. Conductive Two-Dimensional Titanium Carbide 'Clay' with High Volumetric Capacitance. *Nature* **2014**, *516*, 78-82.

(32) Anasori, B.; Lukatskaya, M. R.; Gogotsi, Y. 2D Metal Carbides and Nitrides (MXenes) for Energy Storage. *Nat. Rev. Mater.* **2017**, *2*, 16098.

(33) Wang, X.; Kajiyama, S.; Iinuma, H.; Hosono, E.; Oro, S.; Moriguchi, I.; Okubo, M.; Yamada, A. Pseudocapacitance of MXene Nanosheets for High-Power Sodium-Ion Hybrid Capacitors. *Nat. Commun.* **2014**, *6*, 6544.

(34) Alhabeb, M.; Maleski, K.; Anasori, B.; Lelyukh, P.; Clark, L.; Sin, S.; Gogotsi, Y. Guidelines for

Synthesis and Processing of Two-Dimensional Titanium Carbide ($Ti_3C_2T_x$ MXene). *Chem. Mater.* **2017**, *29*, 7633-7644.

(35) Come, J.; Naguib, M.; Rozier, P.; Barsoum, M. W.; Gogotsi, Y.; Taberna, P.-L.; Morcrette, M.; Simon, P. A Non-Aqueous Asymmetric Cell with a Ti_2C-Based Two-Dimensional Negative Electrode. *J. Electrochem. Soc.* **2012**, *159*, A1368-A1373.

(36) Halim, J.; Kota, S.; Lukatskaya, M. R.; Naguib, M.; Zhao, M.-Q.; Moon, E. J.; Pitock, J.; Nanda, J.; May, S. J.; Gogotsi, Y.; Barsoum, M. W. Synthesis and Characterization of 2D Molybdenum Carbide (MXene). *Adv. Funct. Mater.* **2016**, *26*, 3118-3127.

(37) Lukatskaya, M. R.; Kota, S.; Lin, Z.; Zhao, M.-Q.; Shpigel, N.; Levi, M. D.; Halim, J.; Taberna, P.-L.; Barsoum, M. W.; Simon, P.; Gogotsi, Y. Ultra-High-Rate Pseudocapacitive Energy Storage in Two-Dimensional Transition Metal Carbides. *Nat. Energy* **2017**, *2*, 17105.

(38) Okubo, M.; Sugahara, A.; Kajiyama, S.; Yamada, A. MXene as a Charge Storage Host. *Acc. Chem. Res.* **2018**, *51*, 591-599.

(39) Zhang, C. J.; Pinilla, S.; McEvoy, N.; Cullen, C. P.; Anasori, B.; Long, E.; Park, S. H.; Seral-Ascaso, A.; Shmeliov, A.; Krishnan, D.; Morant, C.; Liu, X.; Duesberg, G. S.; Gogotsi, Y.; Nicolosi, V. Oxidation Stability of Colloidal Two-Dimensional Titanium Carbides. *Chem. Mater.* **2017**, *29*, 4848-4856.

(40) Sugahara, A.; Ando, Y.; Kajiyama, S.; Yazawa, K.; Gotoh, K.; Otani, M.; Okubo, M.; Yamada, A. Negative Dielectric Constant of Water Confined in Nanosheets. *Nat. Commun.* **2019**, *10*, 850.

(41) Kajiyama, S.; Szabova, L.; Iinuma, H.; Sugahara, A.; Gotoh, K.; Sodeyama, K.; Tateyama, Y.; Okubo, M.; Yamada, A. Enhanced Li-Ion Accessibility in MXene Titanium Carbide by Steric Chloride Termination. *Adv. Energy Mater.* **2017**, *7*, 1601873.

(42) Jaramillo, T. F.; Jørgensen, K. P.; Bonde, J.; Nielsen, J. H.; Horch, S.; Chorkendorff, I. Identification of Active Edge Sites for Electrochemical H_2 Evolution from MoS_2 Nanocatalysts. *Science* **2007**, *317*, 100-102.

(43) Benson, E. E.; Zhang, H.; Schuman, S. A.; Nanayakkara, S. U.; Bronstein, N. D.; Ferrere, S.; Blackburn, J. L.; Miller, E. M. Balancing the Hydrogen Evolution Reaction, Surface Energetics, and Stability of Metallic MoS_2 Nanosheets via Covalent Functionalization. *J. Am. Chem. Soc.* **2018**, *140*, 441-450.

(44) David, F.; Vokhmin, V.; Ionova, G. Water Characteristics Depend on the Ionic Environment. Thermodynamics and Modelisation of the Aquo Ions. *J. Mol. Liq.* **2001**, *90*, 45-62.

(45) Shpigel, N.; Levi, M. D.; Sigalov, S.; Mathis, T. S.; Gogotsi, Y.; Aurbach, D. Direct Assessment of Nanoconfined Water in 2D Ti_3C_2 Electrode Interspaces by a Surface Acoustic Technique. *J. Am. Chem. Soc.* **2018**, *140*, 8910-8917.

(46) Owusu, K. A.; Qu, L.; Li, J.; Wang, Z.; Zhao, K.; Yang, C.; Hercule, K. M.; Lin, C.; Wei, Q.; Zhou, L.; Mai, L. Low-Crystalline Iron Oxide Hydroxide Nanoparticles Anode for High-Performance Supercapacitors. *Nat. Commun.* **2017**, *8*, 14264.

(47) Shan, X.; Charles, D. S.; Lei, Y.; Qiao, R.; Wang, G.; Yang, W.; Feygenson, M.; Su, D.; Teng, X. Bivalence Mn_5O_8 with Hydroxylated Interphase for High-Voltage Aqueous Sodium-Ion Storage. *Nat. Commun.* **2016**, *7*, 13370.

(48) Zhu, K.; Zhang, H.; Ye, K.; Zhao, W.; Yan, J.; Cheng, K.; Wang, G.; Yang, B.; Cao, D. Two-Dimensional Titanium Carbide MXene as a Capacitor-Type Electrode for Rechargeable Aqueous Li-Ion and Na-Ion Capacitor Batteries. *ChemElectroChem* **2017**, *4*, 3018-3025.

(49) Gao, Q.; Demarconnay, L.; Raymundo-Piñero, E.; Béguin, F. Exploring the Large Voltage Range of Carbon/Carbon Supercapacitors in Aqueous Lithium Sulfate Electrolyte. *Energy Environ. Sci.* **2012**, *5*, 9611-9617.

(50) Xia, H.; Meng, Y. S.; Yuan, G.; Cui, C.; Lu, L. A Symmetric RuO_2/RuO_2 Supercapacitor Operating at 1.6 V by Using a Neutral Aqueous Electrolyte. *Electrochem. Solid State Lett.* **2012**, *15*, A60-A63.

Chapter 4: Interfacial dissociation of contact-ion-pair on MXene electrodes in concentrated aqueous electrolytes

4.1 Introduction

Reliable energy storage devices that achieve both high-energy and high-power densities are an important goal for sustainable developments, because their wide deployment in a power grid affords us clean energy.[1,2] Although lithium-ion batteries offer high energy density, slow ion transport disables quick (dis)charging, resulting in low power density.[3] Moreover, flammable organic electrolytes used in lithium-ion batteries give rise to serious safety concerns, which undermines confidence in their reliability.[4]

An aqueous electric double-layer capacitor (EDLC) is a promising candidate as safe and high-power electrochemical energy storage devices owing to fast electric double-layer (EDL) formation as well as a use of nonflammable aqueous electrolytes.[5,6] However, as the energy density of EDLCs is expressed as $C\Delta E^2/2$ (C: capacitance, ΔE: voltage window),[7] the narrow electrochemical potential window of water (V = 1.23 V) severely restricts the energy density of aqueous EDLCs relative to that of batteries and nonaqueous EDLCs. As an effective strategy to solve this dilemma, concentrated aqueous electrolytes have attracted significant attention.[8-10] In concentrated aqueous electrolytes, charge-transport cations are coordinated by both water and anions, while a trace of non-coordinating water cannot form a hydrogen-bonding network. Thus, the highest occupied molecular orbital (HOMO) level of most water molecules is lowered by the coordination to cations, which suppresses an anodic oxygen evolution reaction. On the other hand, a cathodic hydrogen evolution reaction is suppressed by the formation of a solid-electrolyte interphase (SEI) derived from the reductive decompositon of anions. Consequently, concentrated aqueous electrolytes can offer a much wider electrochemical potential window ΔE > 3 V,[9,10] which significantly increases the aqueous EDLCs' energy density.

For example, a 21 mol/kg lithium bis(trifluoromethanesulfonyl)imide ($LiN(SO_2CF_3)_2$, LiTFSI) aqueous electrolyte (5.2 M LiTFSI/H_2O, H_2O/Li ratio: 2.5) called water-in-salt was applied to a hybrid capacitor consisting of an activated carbon positive electrode and a MnO_2 negative electrode, which achieved a wide operation potential window of ΔE = 2.0 V.[11] Using binary salts (LiTFSI and LiBETI where BETI is bis(perfluoroethyl sulfonyl) imide, $LiN(SO_2C_2F_5)_2$), a superconcentrated aqueous electrolyte $Li(TFSI)_{0.7}(BETI)_{0.3}/2H_2O$ (H_2O/Li molar ratio: 2.0) called hydrate melt can further expand an electrochemical potential window,[10] which was applied to a hybrid capacitor

consisting of an activated carbon positive electrode and a MXene Ti_2CT_x negative electrode.[12] However, although the applications of concentrated aqueous electrolytes to EDLCs successfully increased the energy density, it was also revealed that their power density is sacrificed[11,13]; the energy density of the EDLC of MXene Ti_2CT_x|hydrate melt|activated carbon decreases from 23 to 7 Wh/kg with increasing the power density from 10 to 200 W/kg (per the total weight of active materials).[12] For the improvement of the limited rate performance with concentrated aqueous electrolytes, the first step should be to clarify the rate-determining step during (dis)charging.

In this work, I study the ion transport mechanism of MXene $Ti_3C_2T_x$ electrode with aqueous electrolytes. MXene is an emerging class of two-dimensional transition-metal carbides/nitrides with general formula of $M_{n+1}X_nT_x$, where M is Ti, Mo, Nb, V, *etc.*, X is C, N, *n* is 1, 2, or 3, T_x is a surface termination group such as -OH, -O, -F, -Cl.[14-22] Owing to high electronic conductivity and large interlayer space, MXene $Ti_3C_2T_x$ with an aqueous Li^+ electrolyte exhibits fast intercalation of hydrated Li^+ to form an EDL within the interlayer space (**Figure 4.1**), delivering a large EDL capacitance over 120 F/g at high charge/discharge rates.[15,23,24] As shown in **Figure 4.1**, a MXene-aqueous electrolyte system is approximated by a Randles circuit consisting of a series resistance R_s, a surface EDL capacitance C_{dl}, an interfacial Li^+ transfer resistance R_i, and a Warburg element of hydrated Li^+ diffusion in interlayer space Z_w.[25,26] Importantly, the energy barrier of each ion-transport resistance (R_s and R_i) can be evaluated using temperature dependent electrochemical impedance spectroscopy (EIS),[27-30] which sheds light on the atomic/molecular-scale ion-transport mechanism.

Herein, I demonstrate that increasing salt concentration causes the increase of energy barriers for both bulk and interfacial ion transports, leading to the limited rate performance of MXene electrodes with concentrated aqueous electrolytes.

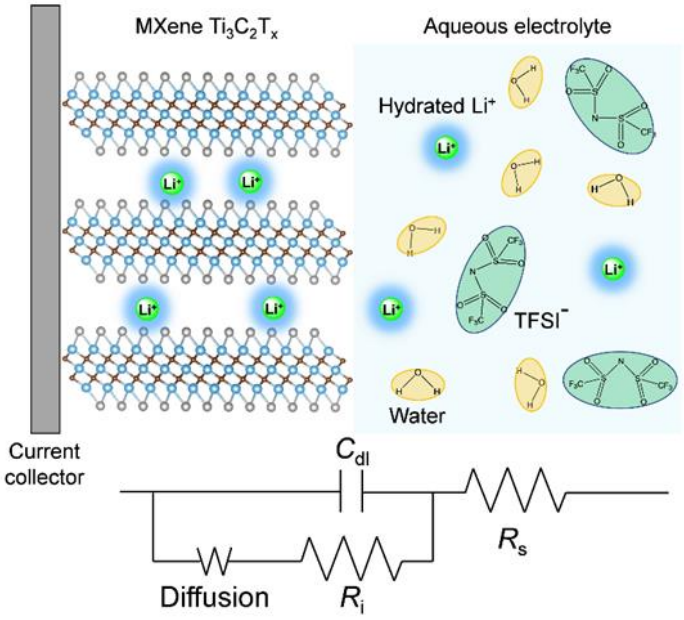

Figure 4.1 Schematic illustration of a $Ti_3C_2T_x$ electrode and an aqueous LiTFSI electrolyte. Hydrated Li^+ ions are intercalated/de-intercalated upon charge and discharge. An equivalent Randles circuit is also shown. R_s: a series resistance including a bulk electrolyte resistance, R_i: interfacial Li^+ transfer resistance, C_{dl}: a surface double-layer capacitance, W: Warburg element of hydrated Li^+ diffusion in MXene.

4.2 Synthesis and characterization of Ti_3AlC_2 and $Ti_3C_2T_x$

MAX phase Ti_3AlC_2 was prepared by heating the mixture of Ti_2AlC and TiC at 1350 ˚C for 1 h under Ar flow. The X-ray diffraction (XRD) pattern of Ti_3AlC_2 (**Figure 4.2**) is fully indexed to hexagonal $P6_3/mmc$, indicating the successful synthesis of Ti_3AlC_2. MXene $Ti_3C_2T_x$ was prepared by extracting Al layers from Ti_3AlC_2 using LiF/HCl aqueous solution (**Table 4.1**). As shown in Figure 2, 002 and 004 diffraction peaks corresponding to the interlayer distance (d_{inter}) shift to lower 2θ angle, which suggests the expansion of d_{inter} from 9.2 to 11.4 Å after the removal of Al layers. Scanning electron microscope (SEM) images, **Figure 4.3**, show that particulate Ti_3AlC_2 is transformed to partially exfoliated morphology after the removal of Al layers. All these observations are consistent with those reported previously, confirming the successful synthesis of MXene $Ti_3C_2T_x$.[16,18] MXenes Ti_2CT_x and Nb_2CT_x were also synthesized according to the methods reported previously.[16,21] Note that, as the main interest in this work is the ion transport mechanism of MXene electrodes with existence of aqueous electrolytes, I used non-delaminated $Ti_3C_2T_x$ for electrochemical measurements to avoid complexities from the porous structure of delaminated MXenes.

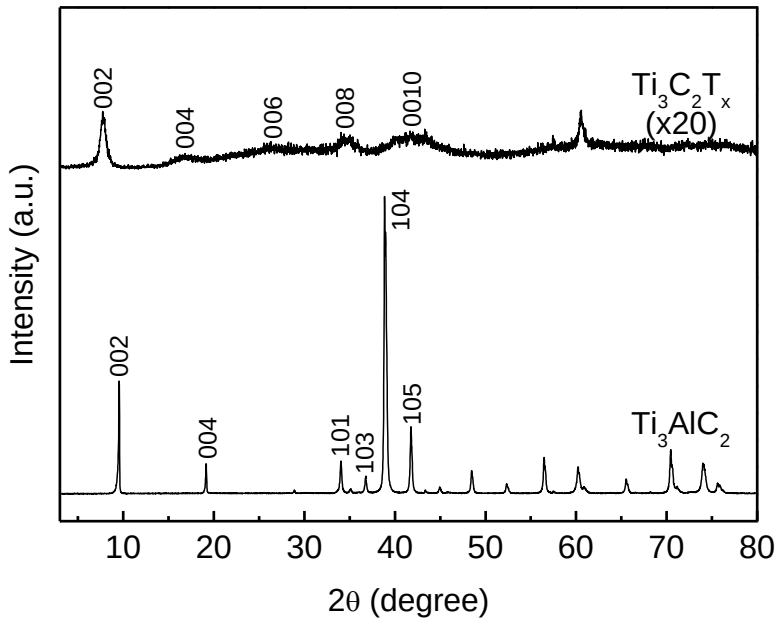

Figure 4.2 X-ray diffraction patterns for Ti_3AlC_2 and $Ti_3C_2T_x$.

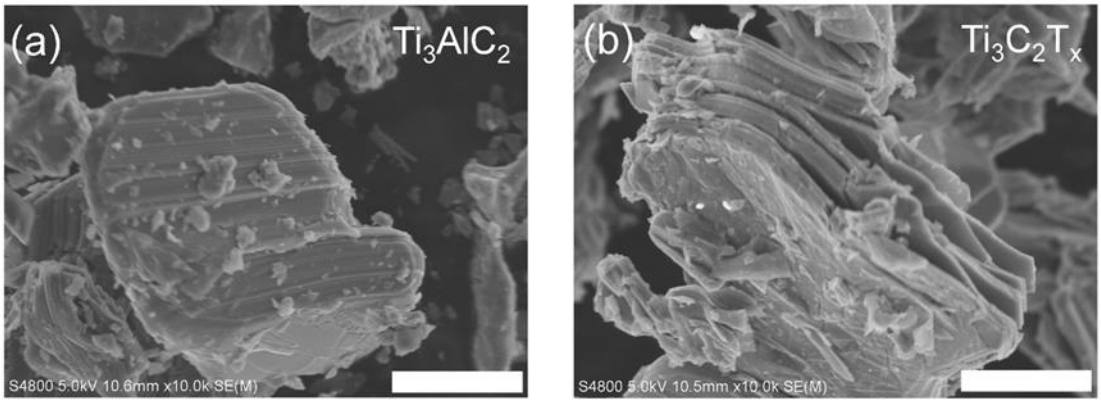

Figure 4.3 SEM images of (a) Ti_3AlC_2 and (b) $Ti_3C_2T_x$. The scale bars are 3 μm.

Table 4.1 Energy dispersive X-ray spectroscopy analysis of $Ti_3C_2T_x$.

	Ti atomic%	Al atomic%	C atomic%
$Ti_3C_2T_x$	59.7	0.5	39.8

4.3 Electrochemical properties of MXenes in aqueous electrolytes

First of all, the cathodic potential limit of $Ti_3C_2T_x$ electrode was determined by chronoamperometry (**Figure 4.4**) with various aqueous electrolytes (LiTFSI/47.7H_2O (1.0 M), LiTFSI/10.3H_2O (3.0 M), LiTFSI/2.5H_2O (water-in-salt), and $Li(TFSI)_{0.7}(BETI)_{0.3}$/2$H_2O$ (hydrate melt)). Concentrated electrolytes have lower cathodic potential limits (-1.1 V vs. Ag/AgCl for a hydrate melt and -1.0 V for a water-in-salt) than those of dilute electrolytes (-0.8 V vs. Ag/AgCl for 1.0 and 3.0 M LiTFSI).

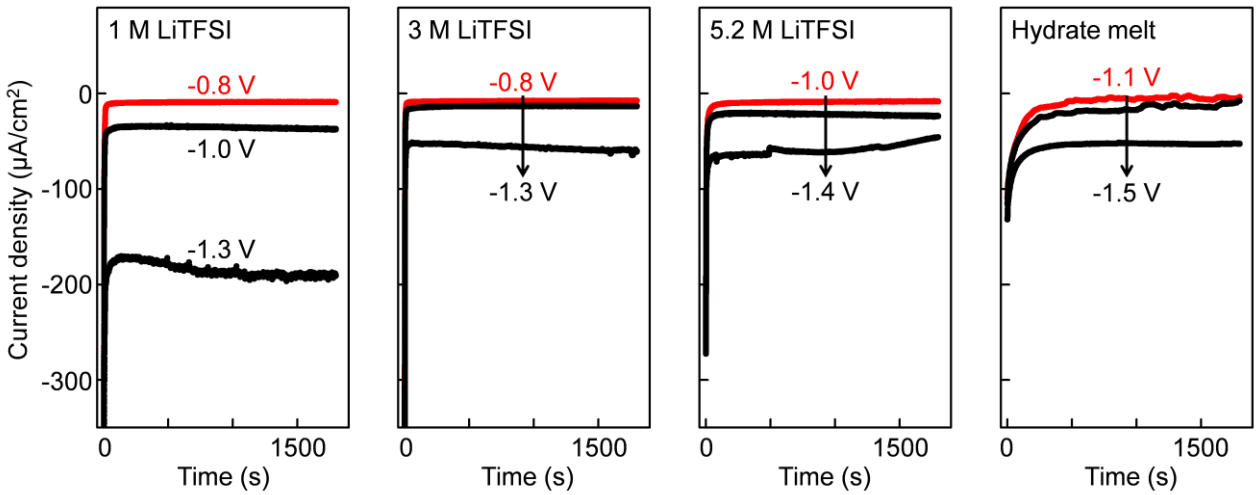

Figure 4.4 Chronoamperometry of $Ti_3C_2T_x$ at various applied potentials vs. Ag/AgCl with various aqueous electrolytes. Red lines indicate negligible steady-state cathodic current less than -10 μA/cm^2, which determines a cut-off voltage for each system.

After determination of stable potential window, the electrochemical properties of $Ti_3C_2T_x$ electrodes in various aqueous electrolytes (LiTFSI/47.7H_2O (1.0 M), LiTFSI/10.3H_2O (3.0 M), LiTFSI/2.5H_2O (water-in-salt), and $Li(TFSI)_{0.7}(BETI)_{0.3}/2H_2O$ (hydrate melt)) were evaluated by cyclic voltammetry (CV) at various scan rates (**Figure 4.5**). Regardless of an electrolyte concentration, $Ti_3C_2T_x$ electrodes in aqueous electrolytes exhibit rectangular shaped CV curves at a slow scan rate of 0.5 mV/s, which is characteristic of an EDLC electrode. Hydrated Li^+ ions intercalate into the interlayer space of $Ti_3C_2T_x$ without charge transfer, and EDL is formed within the interlayer space.[26,27]

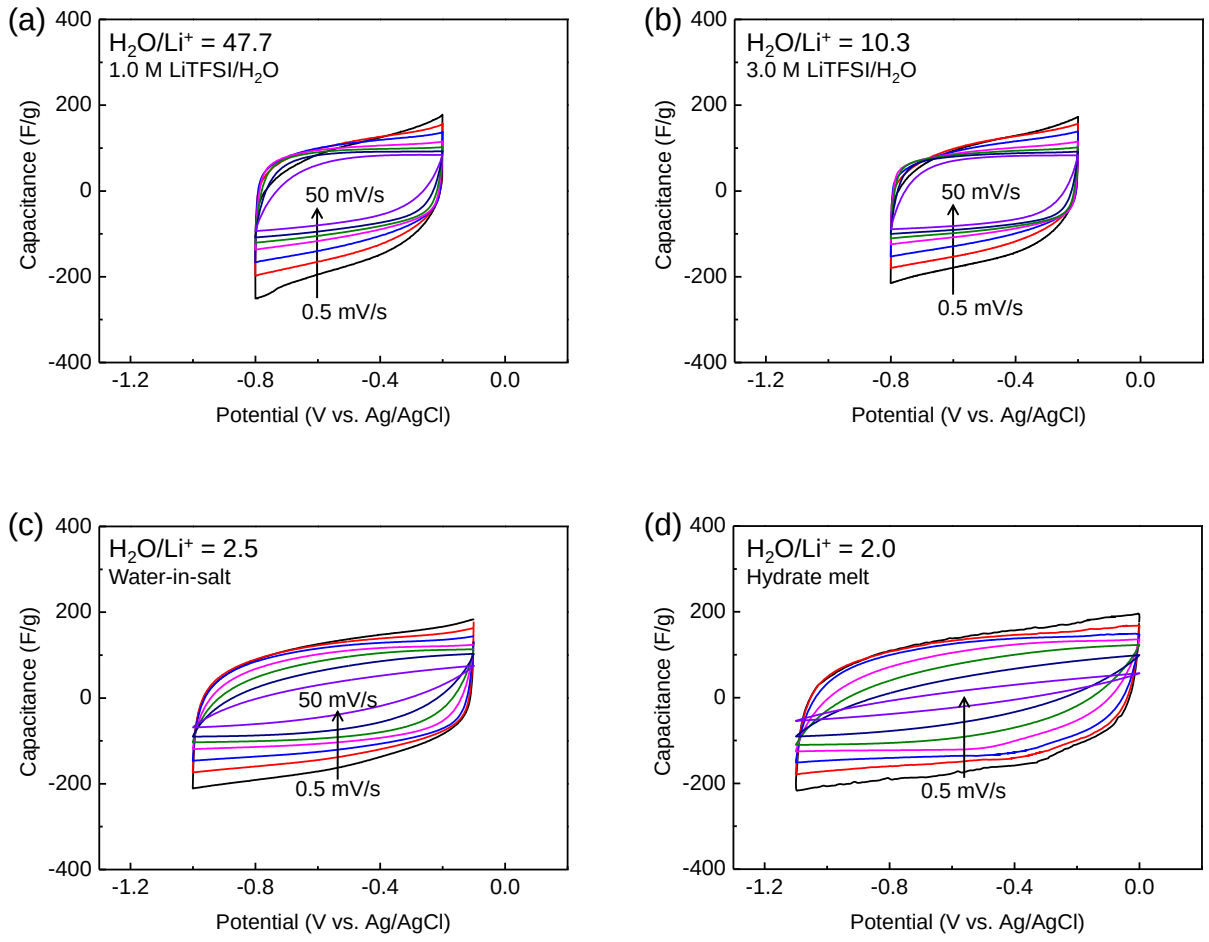

Figure 4.5 Scan rate dependence of CV curves of $Ti_3C_2T_x$ in (a) 1.0 M LiTFSI/H_2O, (b) 3.0 M LiTFSI/H_2O, (c) LiTFSI/2.5H_2O (a water-in-salt electrolyte), and (d) $Li(TFSI)_{0.7}(BETI)_{0.3}/2H_2O$ (a hydrate-melt electrolyte). CV scan starts from open circuit potential (OCP) with various aqueous electrolytes.

Concerning the scan-rate dependence with LiTFSI/47.7H_2O (1.0 M), 44% of the specific capacitance at a slow scan rate of 0.5 mV/s retains at the fast scan rate of 50 mV/s. However, increasing the salt concentration limits the rate performance (**Figure 4.6**). For example, with a hydrate-melt electrolyte, the specific capacitance largely decreases from 141 F/g at 0.5 mV/s to 12.9 F/g at 50 mV/s. If the capacitance is roughly divided into contributions from surface-control and diffusion-control currents using $i = Av^{0.5} + Bv$ (i : specific current, v : scan rate, A : diffusion-control contribution, B : surface-control contribution),[31,32] the fraction of a diffusion-control capacitance increases from 36% to 56% with increasing the salt concentration (inset in Figure 4d), which supports the limited rate performance with concentrated electrolytes. The limited rate performance of concentrated electrolytes was also confirmed using MXene Ti_2CT_x and Nb_2CT_x (**Figures 4.7 and 4.8**). As the salt concentration does not affect either ion transport or electric conduction in MXene, ion transport in an electrolyte and/or at an electrode-electrolyte interface is a rate-determining step at the scan rates faster than 10 mV/s.

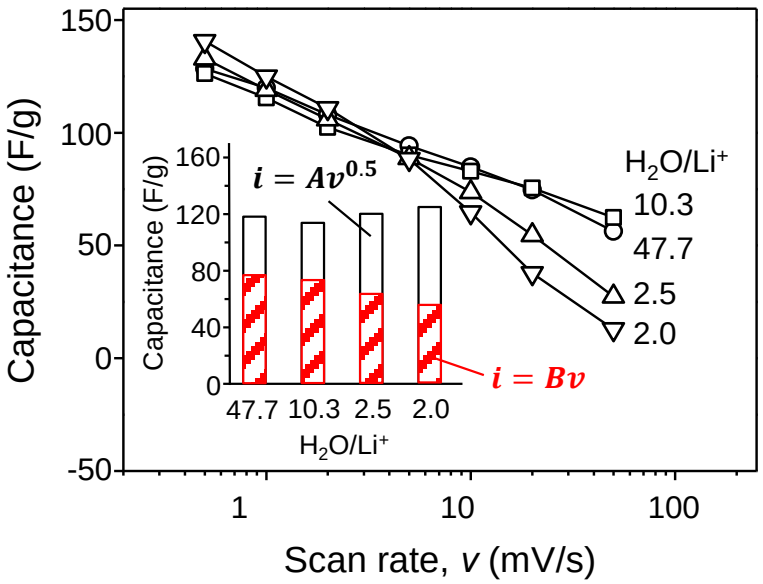

Figure 4.6 Scan rate v dependence of a specific capacitance. The inset shows the rough estimation of surface-control (red bar) and diffusion-control (empty bar) capacitances.

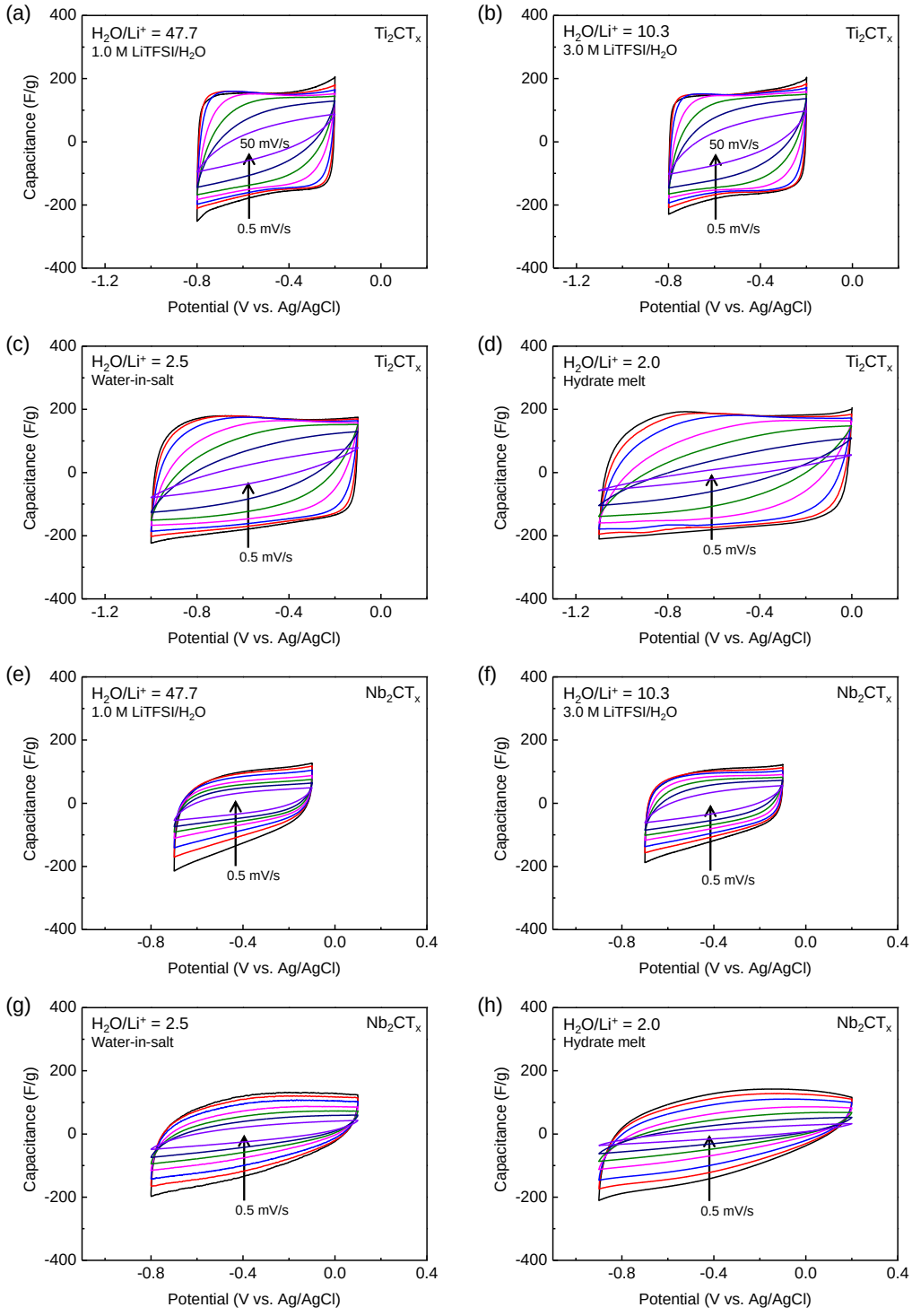

Figure 4.7 Scan rate dependence of CV curves of (a-d) Ti_2CT_x and (e-h) Nb_2CT_x in 1.0 M LiTFSI/H_2O, 3.0 M LiTFSI/H_2O, LiTFSI/2.5H_2O (a water-in-salt electrolyte), and $Li(TFSI)_{0.7}(BETI)_{0.3}/2H_2O$ (a hydrate-melt electrolyte).

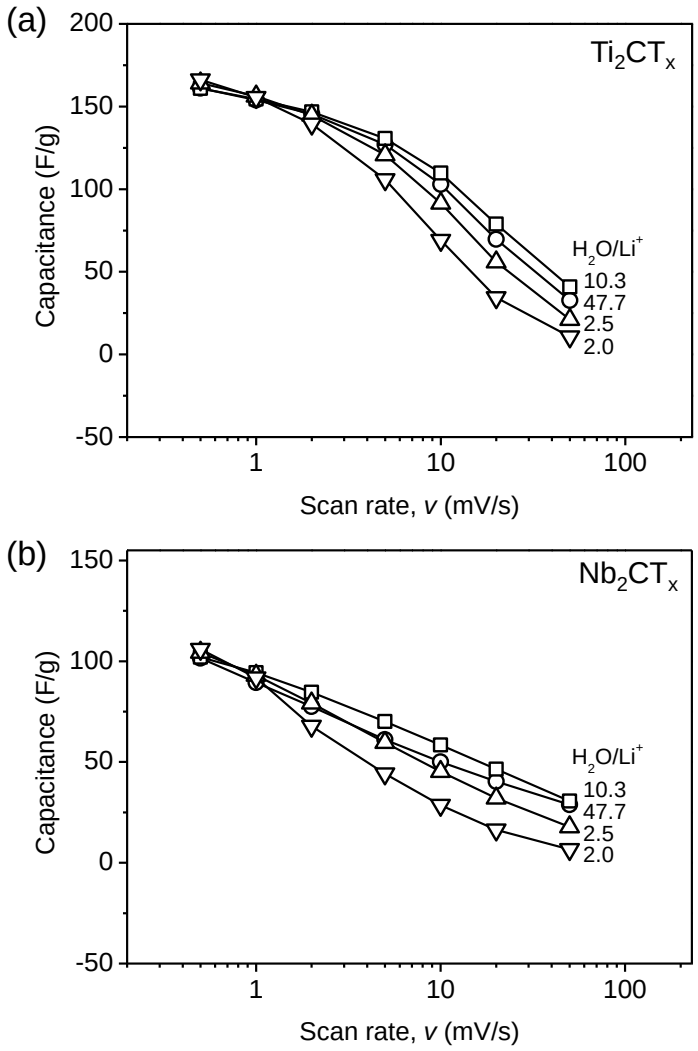

Figure 4.8 Scan rate *v* dependence of a specific capacitance for (a) Ti_2CT_x and (b) Nb_2CT_x with 1.0 M LiTFSI/H_2O, 3.0 M LiTFSI/H_2O, LiTFSI/2.5H_2O (a water-in-salt electrolyte), and $Li(TFSI)_{0.7}(BETI)_{0.3}/2H_2O$ (a hydrate-melt electrolyte).

4.4 Interfacial charge transfer of MXene with aqueous electrolytes

Figure 4.9 shows general trend of bulk electrolyte resistance (R_s) with increased concentration of electrolytes. In a region of extremely dilute concentration, R_s slightly decreases with increased concentration because charge carriers become abundant and ionic conductivity increases. However, R_s dramatically increases in a region of high concentration since charge mobility and ionic conductivity remarkably decreases.[8]

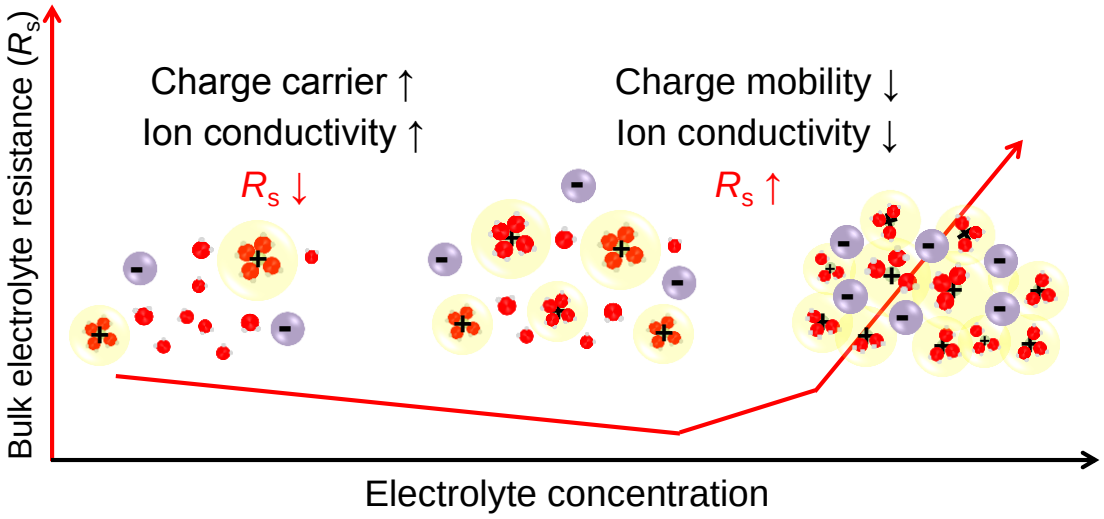

Figure 4.9 General trend of bulk electrolyte resistance with various concentrations of electrolytes.

To further analyze the internal resistances, electrochemical impedance spectroscopy (EIS) was applied. Nyquist plots at 298 K (**Figure 4.10**) show that both a series resistance (R_s, **Figure 4.1**) and an interface resistance (R_i, **Figure 4.1**) increase with increasing the salt concentration (**Table 4.2**). The increase in R_s is attributable to the increase of electrolyte resistivity (**Table 4.2**), while the increase in R_i can be explained by either SEI formation or a change in an interfacial ion-transport mechanism. It is important to note that R_i cannot be described as a charge-transfer resistance, because hydrated Li^+ forms EDL in the interlayer space without charge transfer.[23,24]

Table 4.2 Bulk resistivity, series resistance R_s, and interfacial resistance R_i of various aqueous electrolytes at 298 K.

	H_2O/Li^+ ratio	bulk resistivity [Ω cm]	R_s [Ω]	R_i [Ω]
1 M LiTFSI/H_2O	47.7	28.8	7.4	14.0
3 M LiTFSI/H_2O	10.2	19.2	7.9	20.5
Water-in-salt	2.5	117.6	59.2	48.2
Hydrate melt	2.0	448.4	78.7	75.8

In order to investigate the atomic/molecular-level origin of R_i, the temperature dependence of EIS was measured from 298 to 318 K (**Figure 4.10**). As concentration increases of LiTFSI aqueous electrolytes, R_s and R_i values gradually increase throughout the temperature. It should be noted that R_s for $Ti_3C_2T_x$ electrode with increasing concentration is well-consistent with the general trend (**Figure 4.9**).

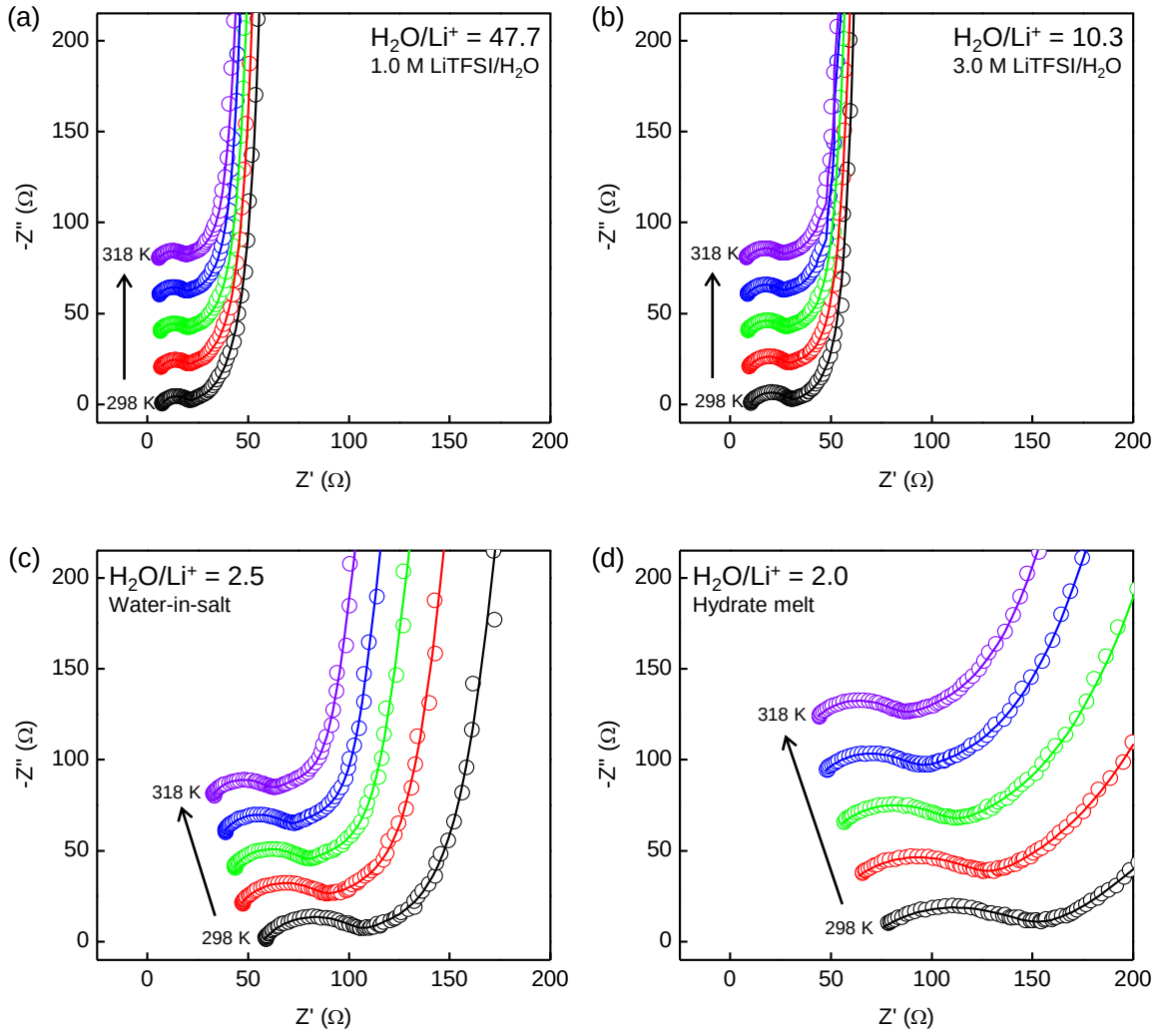

Figure 4.10 Electrochemical impedance spectra for $Ti_3C_2T_x$ in (a) 1.0 M LiTFSI/H_2O, (b) 3.0 M LiTFSI/H_2O, (c) LiTFSI/2.5H_2O (a water-in-salt electrolyte), and (d) $Li(TFSI)_{0.7}(BETI)_{0.3}/2H_2O$ (a hydrate-melt electrolyte). Solid line indicates a fitted curve obtained by Zview software.

For chemical reaction kinetics, Arrhenius plots are invaluable tools, which can predict activation energy (E_A) by analyzing temperature-dependent EIS parameters. Based on Arrhenius equation, $\ln R_i^{-1}$ (or R_s^{-1}) $= \ln A + \frac{-E_A}{1000R}(\frac{1000}{T})$ (A: frequency factor; E_A: activation energy; R: gas constant; T: absolute temperature), the Arrhenius plot (1000/T vs. $\ln R_i^{-1}$ (or R_s^{-1})) can be depicted in a linear form for $Ti_3C_2T_x$ (**Figure 4.11**), which could provide estimations of E_a from the slop value ($\frac{-E_A}{1000R}$).

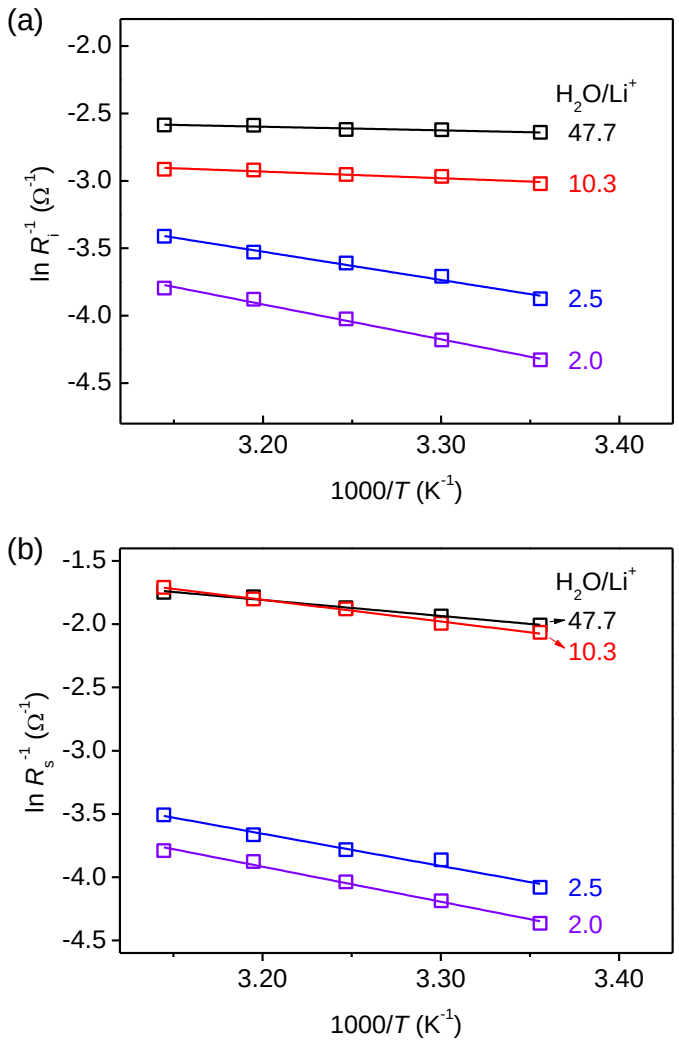

Figure 4.11 Arrhenius plots of (a) $\ln R_i^{-1}$ and (b) $\ln R_s^{-1}$ against 1000/T for $Ti_3C_2T_x$ in various aqueous electrolytes.

Figure 4.12 shows the salt-concentration dependence of E_A for R_i and R_s with a $Ti_3C_2T_x$ electrode. For comparison, E_A for ionic conductivity σ in bulk electrolytes is also plotted. For diluted electrolytes (1.0 M and 3.0 M aqueous LiTFSI electrolytes), E_A for R_s is in the range of 10-15 kJ/mol with a $Ti_3C_2T_x$ electrode, which is almost same as that for σ. Therefore, R_s is dominated by the ion conduction of a bulk electrolyte (**Figure 4.13a**). It is well known that a main energy barrier against ion transport in an aqueous solution is Stokes' friction force, where a water hydrogen-bonding network is broken and re-organized in association with the transport of a hydrated ion.[33,34] The energy required for breaking a hydrogen bond in pure water was reported as 23.3 kJ/mol,[35] which is slightly larger than E_A for R_s. Presumably, the water hydrogen-bonding network is disordered near a hydrated ion (Frank-Wen model),[36] making the hydrogen-bond breaking/re-organizing energy a bit smaller. On the other hand, E_A for R_i is negligibly small (< 5 kJ/mol) relative to that for R_s, because a water hydrogen-bonding network at inner/outer Helmholtz layers is largely disordered due to surface water adsorption and surface EDL formation,[37] and the interfacial transport of a hydrated ion does not need breaking/re-organizing hydrogen bonds (**Figure 4.13a**).

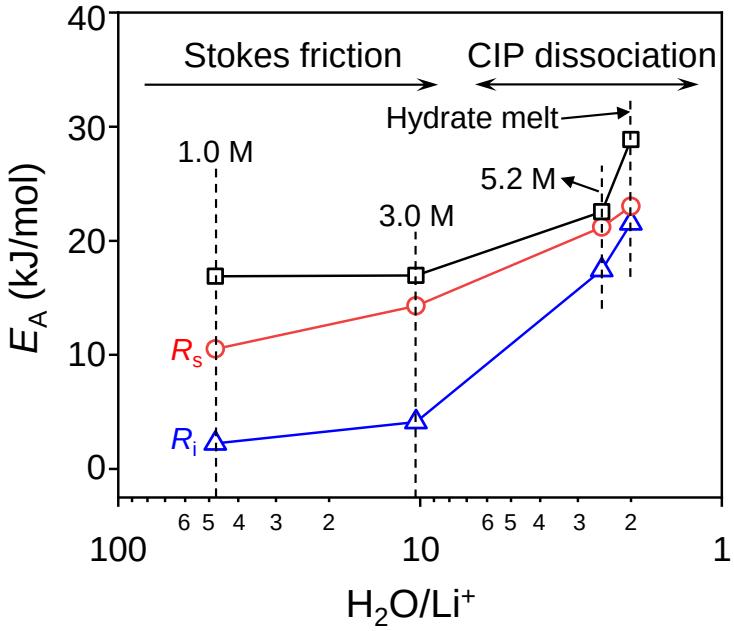

Figure 4.12 Concentration dependence of activation energy in $Ti_3C_2T_x$ for ionic conductivity σ, series resistance R_s, and interfacial resistance R_i. Stokes' friction and CIP dissociation regions indicate a dominant energy barrier for ion transport.

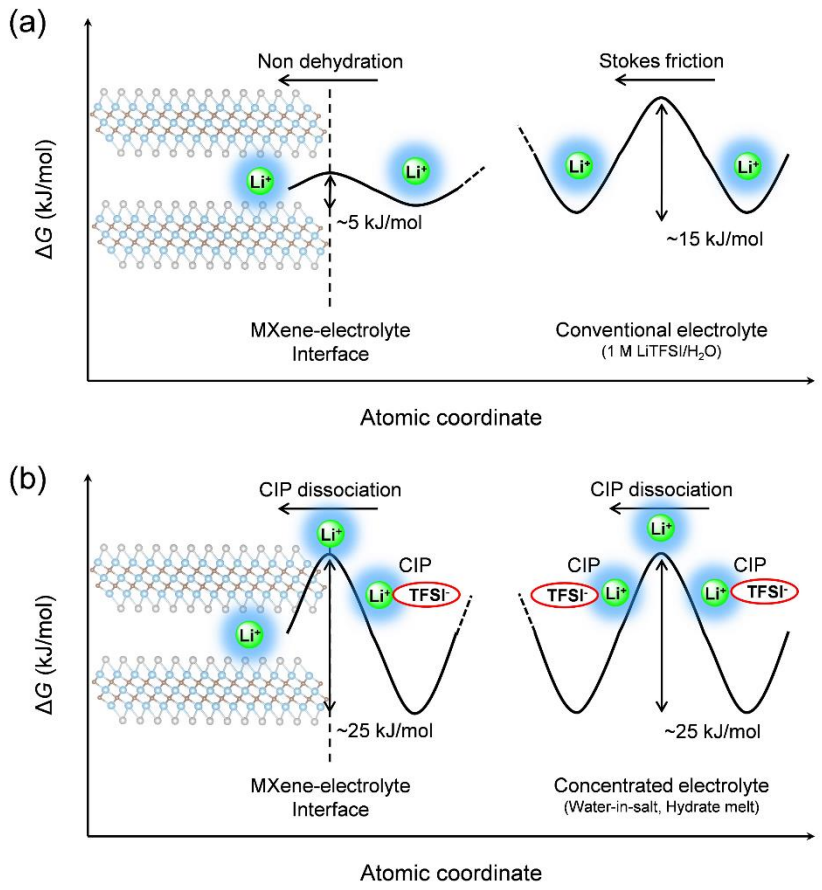

Figure 4.13 Schematic energy diagram for Li-ion transport in MXene electrodes with (a) diluted aqueous electrolytes and (b) concentrated aqueous electrolytes.

With increasing the salt concentration, E_A for R_s and σ increase significantly (*e.g.*, 23.0 and 28.9 kJ/mol for the $Ti_3C_2T_x$ electrode with a hydrate-melt electrolyte). As Li^+ is coordinated by anions as well as H_2O to form contact-ion-pair in concentrated electrolytes,[8,38,39] large E_A for R_s and σ should be ascribed to the dissociation of CIP (**Figure 4.13b**). Indeed, a Raman peak at around 750 cm^{-1} corresponding to the S-N-S bending of $TFSI^-$ shows a blue shift with increasing the salt concentration (**Figure 4.14a**), indicating the CIP formation in concentrated electrolytes.[10] Similarly, E_A for R_i also increases, *e.g.*, from 2.25 (the $Ti_3C_2T_x$ electrode with a 1.0 M aqueous LiTFSI electrolyte) to 21.5 kJ/mol (the $Ti_3C_2T_x$ electrode with a hydrate-melt electrolyte), as an electrolyte concentration increases, which indicates change in an interfacial ion-transport mechanism. One possible explanation is resistive SEI formation, because E_A for R_i was evaluated using cells after 10 charge/discharge cycles, where an anion-derived SEI should be formed as reported previously.[9,10,40] However, when comparing E_A for R_i of the MXene electrodes with a hydrate-melt electrolyte before and after 10 charge/discharge cycles (*i.e.*, without and with SEI), E_A without SEI (22.2 kJ/mol) is identical with that with SEI (**Figure 4.14b**). Therefore, the energy barrier for interfacial ion transport

is not influenced by the ion conduction in SEI. Considering E_A for R_i is in the same range of E_A for R_s and σ in concentrated electrolytes, it is reasonable to consider that the energy barrier for interfacial ion transport is also dominated by the dissociation of CIP (**Figure 4.13b**).

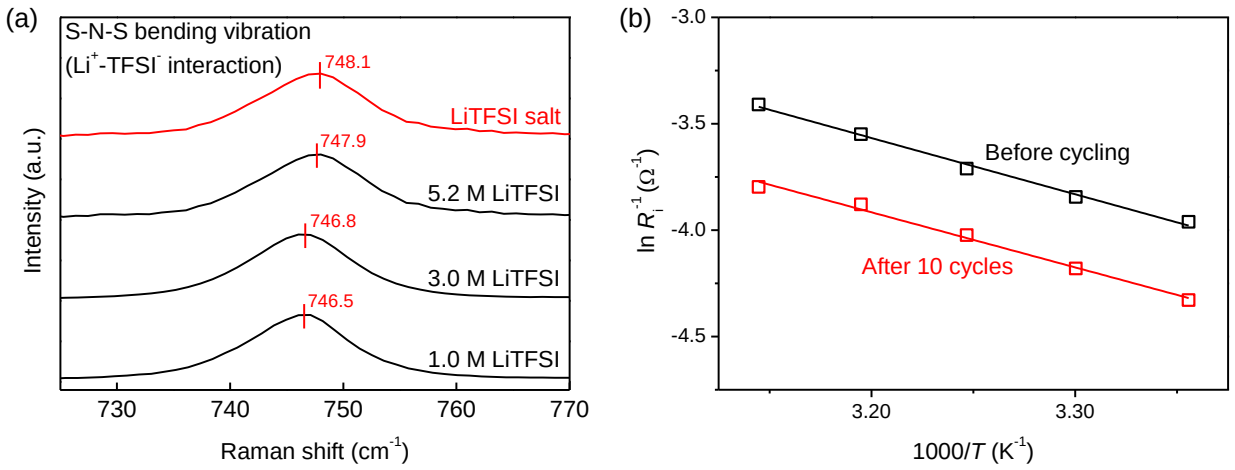

Figure 4.14 (a) Raman spectra of 1.0, 3.0, 5.2 M LiTFSI aqueous electrolytes, and LiTFSI salt in the region of S-N-S bending vibration and (b) Arrhenius plots of the interfacial resistance R_i for $Ti_3C_2T_x$ electrode before and after 10 cycles in a hydrate-melt electrolyte.

The similar trend of Nyquist plots (**Figure 4.15**) and activation energy E_A with various concentrations of aqueous electrolytes is generally observed for other MXenes (Ti_2CT_x and Nb_2CT_x). Activation energy E_A for Ti_2CT_x and Nb_2CT_x was also estimated from an Arrhenius plot (**Figure 4.16**). **Figure 4.17** shows the concentration dependence of E_A for R_i and R_s. Similar to the case of $Ti_3C_2T_x$, E_A for R_s is in the range of 10-15 kJ/mol for diluted electrolytes (1.0 M and 3.0 M), which is almost same as that for σ (**Figure 4.12**). Therefore, R_s is dominated by the ion conduction of a bulk electrolyte. However, with increasing an electrolyte concentration, E_A for R_s increase significantly (*e.g.*, 21.9 kJ/mol (Ti_2CT_x) and 21.1 kJ/mol (Nb_2CT_x) for a hydrate melt) due to formation of CIP in concentrated electrolytes. E_A for R_i in Ti_2CT_x and Nb_2CT_x also increases with increasing electrolyte concentration, which indicates that interfacial ion transport into the MXene interlayer is dominated by the dissociation of CIP in concentrated electrolytes.

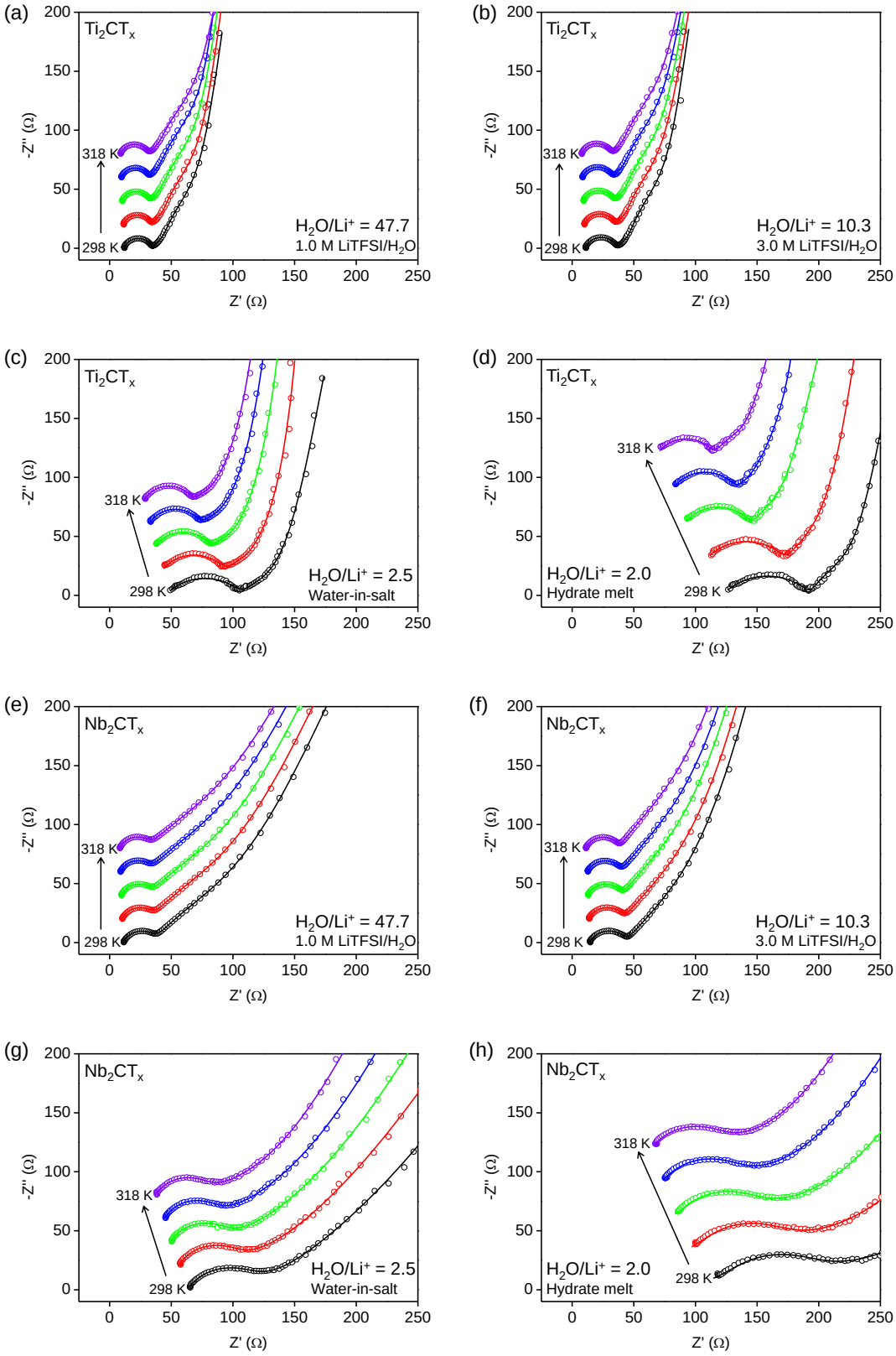

Figure 4.15 Electrochemical impedance spectra for (a-d) Ti_2CT_x and (e-h) Nb_2CT_x in 1.0 M LiTFSI/H_2O, 3.0 M LiTFSI/H_2O, LiTFSI/2.5H_2O (a water-in-salt electrolyte), and $Li(TFSI)_{0.7}(BETI)_{0.3}/2H_2O$ (a hydrate-melt electrolyte).

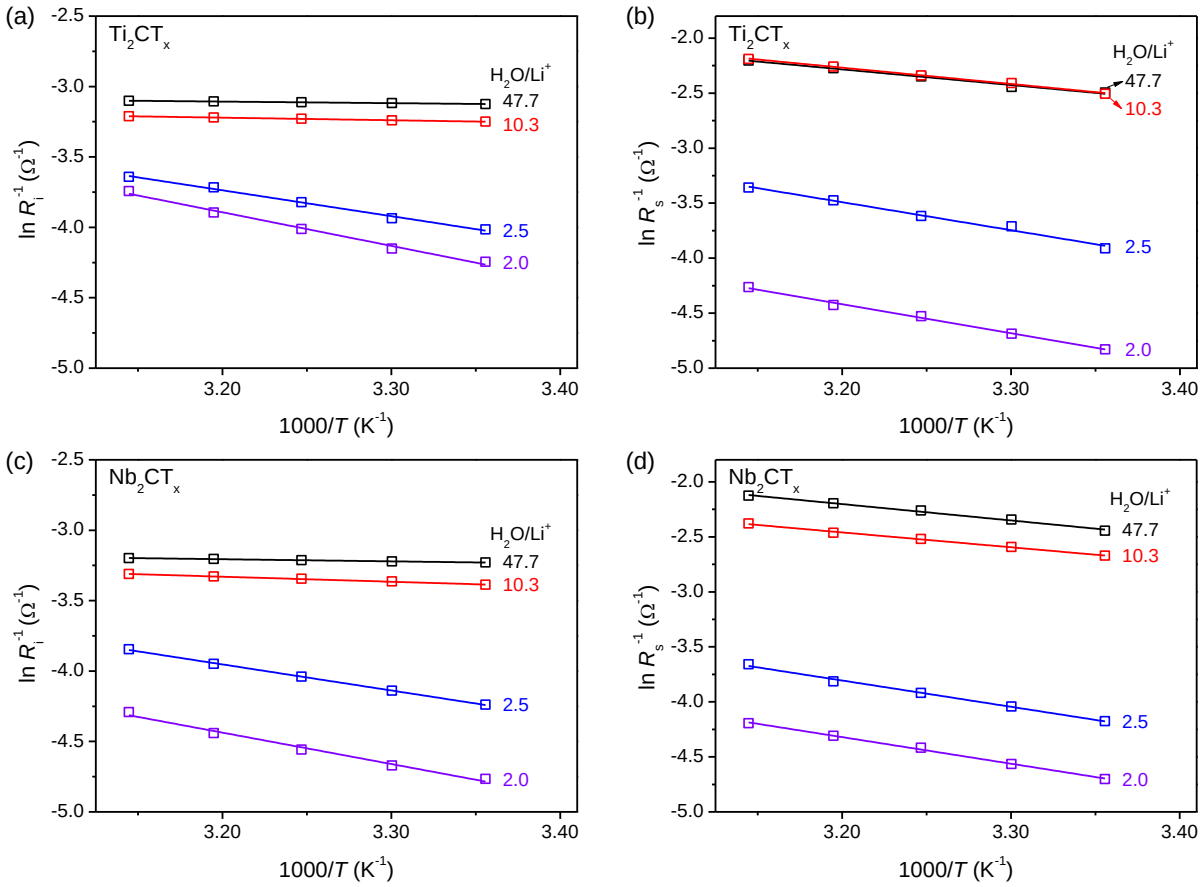

Figure 4.16 Arrhenius plots of (a) ln R_i^{-1} (Ti_2CT_x), (b) ln R_s^{-1} (Ti_2CT_x), (c) ln R_i^{-1} (Nb_2CT_x), and (d) ln R_s^{-1} (Nb_2CT_x) against 1000/T in various aqueous electrolytes.

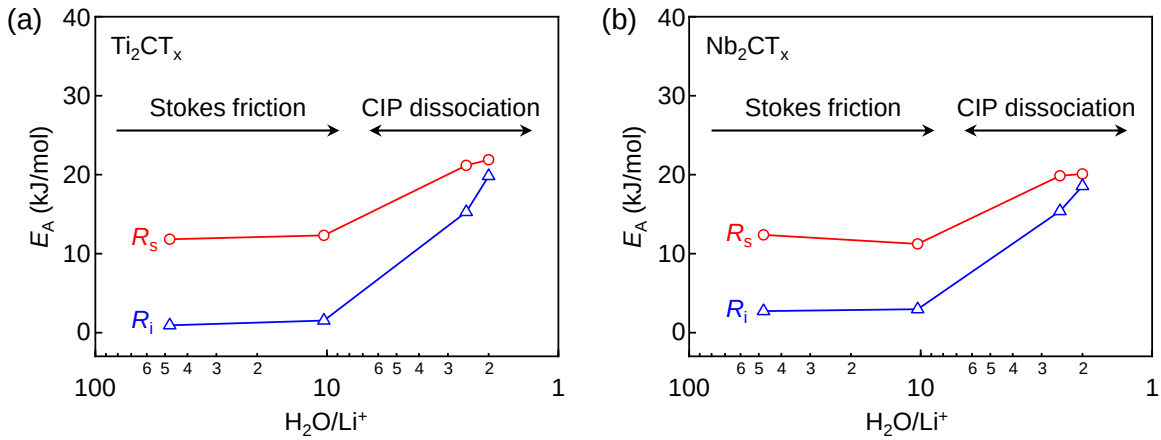

Figure 4.17 Concentration dependence of activation energy in (a) Ti_2CT_x and (b) Nb_2CT_x for series resistance R_s and interfacial resistance R_i.

As illustrated in **Figure 4.13**, in the case of diluted electrolytes (1.0 M and 3.0 M aqueous LiTFSI electrolytes), hydrate Li^+ can rapidly migrate and intercalate into MXene with low E_A for both bulk and interfacial ion transport, achieving better capacitance retention at high rates. However, with increasing the salt concentration, CIP dissociation with large E_A becomes to dominate both bulk and interfacial ion transports, which limits fast (dis)charging capability required for high-power capacitor application. Therefore, to further improve the rate performance of MXene electrodes while maintaining the high voltage operation with concentrated electrolytes, CIP suppression can be a strategy, for example, by using an additive that is able to coordinate to Li^+ preferentially.[41,42]

Figure 4.18 illustrates the overall summary of charge-transport barrier E_A and electrochemical potential window ΔE for conventional organic electrolytes, conventional aqueous electrolytes, and concentrated aqueous electrolytes. It is well known that, despite wide ΔE exceeding 4 V, conventional organic electrolytes have large E_A of approximately 50 kJ/mol for interfacial desolvation, which hinders the high-power operation of Li-ion batteries.[27-30] Although conventional aqueous electrolytes have small E_A of approximately 10 kJ/mol for fast bulk ion transport that enables high-power operation of aqueous capacitors, narrow ΔE severely restricts their energy density. In a striking contrast with this dilemma, concentrated aqueous electrolytes achieve a good balance of low E_A of approximately 20 kJ/mol and wide ΔE exceeding 3.0 V. Such balanced properties of concentrated aqueous electrolytes may offer electrochemical energy storage devices suitable for various applications.

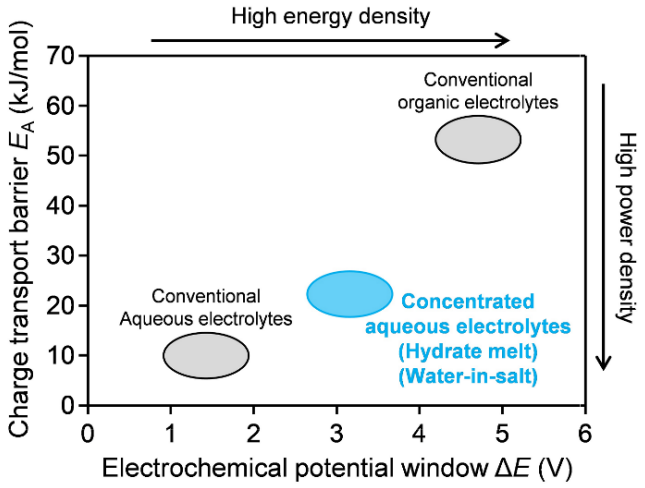

Figure 4.18. Schematic illustration of charge transport barrier E_A and electrochemical potential window ΔE of conventional organic electrolytes (large E_A and wide ΔE), conventional aqueous electrolytes (small E_A and narrow ΔE), and concentrated aqueous electrolytes (small E_A and wide ΔE). Hydrate melt and water-in-salt can offer the intermediate balanced performances.

4.5 Conclusion

I have clarified the ion transport mechanism of MXene electrodes with aqueous electrolytes. With conventional diluted aqueous electrolytes, bulk ion transport is dominated by Stokes' friction force while an energy barrier for interfacial ion transport is negligibly small because a disordered water hydrogen-bonding network at inner/outer Helmholtz layers is not effective to induce frictional interaction with mobile ions. When concentrated electrolytes are used, both bulk and interfacial ion transports are dominated by CIP dissociation with E_A of approximately 20 kJ/mol, which is the main cause for the limited rate performance of MXene electrodes in concentrated electrolytes with respect to the capacitor requirement. However, the emphasis should be placed on the fact that the values of conductivity and activation energy observed in water-in-salt and hydrate-melt electrolytes are much better than those of standard materials in present batteries.

References

(1) Braff, W. A.; Mueller, J. M.; Trancik, J. E. Value of Storage Technologies for Wind and Solar Energy. *Nat. Clim. Change* **2016**, *6*, 964.

(2) Schmidt, O.; Hawkes, A.; Gambhir, A.; Staffell, I. The Future Cost of Electrical Energy Storage Based on Experience Rates. *Nat. Energy* **2017**, *2*, 17110.

(3) Noorden, R. V. The Rechargeable Revolution: A better Battery. *Nature* **2014**, *507*, 26.

(4) Wang, J.; Yamada, Y.; Sodeyama, K.; Watanabe, E.; Takada, K.; Tateyama, Y.; Yamada, A. Fire-Extinguishing Organic Electrolytes for Safe Batteries. *Nat. Energy* **2018**, *3*, 22.

(5) Simon, P.; Gogotsi, Y. Materials for Electrochemical Capacitors. *Nat. Mater.* **2008**, *7*, 845.

(6) Wang, G.; Zhang, L.; Zhang, J. A Review of Electrode Materials for Electrochemical Supercapacitors. *Chem. Soc. Rev.* **2012**, *41*, 797.

(7) Béguin, F.; Frąckowiak, E. Supercapacitors: Mateirlas, Systems and Applications. *Wiley-VCH: Weinheim* **2013**.

(8) Yamada, Y.; Wang, J. H.; Ko, S.; Watanabe, E.; Yamada, A. Advances and Issues in Developing Salt-Concentrated Battery Electrolytes. *Nat. Energy* **2019**, *4*, 269.

(9) Suo, L.; Borodin, O.; Gao, T.; Olguin, M.; Ho, J.; Fan, X.; Luo, C.; Wang, C.; Xu, K. "Water-In-Salt" Electrolyte Enables High-Voltage Aqueous Lithium-Ion Chemistries. *Science* **2015**,

350, 938.

(10) Yamada, Y.; Usui, K.; Sodeyama, K.; Ko, S.; Tateyama, Y.; Yamada, A. Hydrate-Melt Electrolytes for High-Energy-Density Aqueous Batteries. *Nat. Energy* **2016**, *1*, 16129.

(11) Zhang, M.; Makino, S.; Mochizuki, D.; Sugimoto, W. High-Performance Hybrid Supercapacitors Enabled by Protected Lithium Negative Electrode and "Water-In-Salt" Electrolyte. *J. Power Sources* **2018**, *396*, 498-505.

(12) Kim, K.; Ando, Y.; Sugahara, A.; Ko, S.; Yamada, Y.; Otani, M.; Okubo, M.; Yamada, A. Dense Charge Accumulation in MXene with a Hydrate-Melt Electrolyte. *Chem. Mater.* **2019**, *31*, 5190-5196.

(13) Lannelongue, P.; Bouchal, R.; Mourad, E.; Bodin, C.; Olarte, M.; LeVot, S.; Favier, F.; Fontaine, O. "Water-In-Salt" for Supercapacitors: A Compromise between Voltage, Power Density, Energy Density and Stability. *J. Electrochem. Soc.* **2018**, *165*, A657.

(14) Naguib, M.; Kurtoglu, M.; Presser, V.; Lu, J.; Niu, J.; Heon, M.; Hultman, L.; Gogotsi, Y.; Barsoum, M. W. Two-Dimensional Nanocrystals Produced by Exfoliation of Ti_3AlC_2. *Adv. Mater.* **2011**, *23*, 4248.

(15) Lukatskaya, M. R.; Mashtalir, O.; Ren, C. E.; Agnese, Y. D.; Rozier, P.; Taberna, P. L.; Naguib, M.; Simon, P.; Barsoum, M. W.; Gogotsi, Y. Cation Intercalation and High Volumetric Capacitance of Two-Dimensional Titanium Carbide. *Science* **2013**, *341*, 1502.

(16) Ghidiu, M.; Lukatskaya, M. R.; Zhao, M. Q.; Gogotsi, Y.; Barsoum, M. W. Conductive Two-Dimensional Titanium Carbide 'Clay' with High Volumetric Capacitance. *Nature* **2014**, *516*, 78-81.

(17) Wang, X.; Kajiyama, S.; Iinuma, H.; Hosono, E.; Oro, S.; Moriguchi, I.; Okubo, M.; Yamada, A. Pseudocapacitance of MXene Nanosheets for High-Power Sodium-Ion Hybrid Capacitors. *Nat. Commun.* **2015**, *6*, 6544.

(18) Kajiyama, S.; Szabova, L.; Sodeyama, K.; Iinuma, H.; Morita, R.; Gotoh, K.; Tateyama, Y.; Okubo, M.; Yamada, A. Sodium-Ion Intercalation Mechanism in MXene Nanosheets. *ACS Nano* **2016**, *10*, 3334.

(19) Lukatskaya, M. R.; Kota, S.; Lin, Z.; Zhao, M. Q.; Shpigel, N.; Levi, M. D.; Halim, J.; Taberna,

P. L.; Barsoum, M. W.; Simon, P.; Gogotsi, Y. Ultra-High-Rate Pseudocapacitive Energy Storage in Two-Dimensional Transition Metal Carbides. *Nat. Energy* **2017**, *2*, 17105.

(20) Anasori, B.; Lukatskaya, M. R.; Gogotsi, Y. 2D Metal Carbides and Nitrides (MXenes) for Energy Storage. *Nat. Rev. Mater.* **2017**, *2*, 16098.

(21) Kajiyama, S.; Szabova, L.; Iinuma, H.; Sugahara, A.; Gotoh, K.; Sodeyama, K.; Tateyama, Y.; Okubo, M.; Yamada, A. Enhanced Li-Ion Accessibility in MXene Titanium Carbide by Steric Chloride Termination. *Adv. Energy Mater.* **2017**, *7*, 1601873.

(22) Wang, X.; Mathis, T. S.; Li, K.; Lin, Z.; Vlcek, L.; Torita, T.; Osti, N. C.; Hatter, C.; Urbankowski, P.; Sarycheva, A.; Tyagi, M.; Mamontov, E.; Simon, P.; Gogotsi, Y. Influences from Solvents on Charge Storage in Titanium Carbide MXenes. *Nat. Energy* **2019**, *4*, 241.

(23) Okubo, M.; Sugahara, A.; Kajiyama, S.; Yamada, A. MXene as a Charge Storage Host. *Acc. Chem. Res.* **2018**, *51*, 591.

(24) Sugahara, A.; Ando, Y.; Kajiyama, S.; Yazawa, K.; Gotoh, K.; Otani, M.; Okubo, M.; Yamada, A. Negative Dielectric Constant of Water Confined in Nanosheets. *Nat. Commun.* **2019**, *10*, 850.

(25) Randles, J. E. B. Kinetics of Rapid Electrode Reactions. *Discuss. Faraday Soc.* **1947**, *1*, 11.

(26) Mei, B. A.; Munteshari, O.; Lau, J.; Dunn, B.; Pilon, L. Physical Interpretations of Nyquist Plots for EDLC Electrodes and Devices. *J. Phys. Chem. C* **2018**, *122*, 194.

(27) Yamada, I.; Abe, T.; Iriyama, Y.; Ogumi, Z. Lithium-Ion transfer at $LiMn_2O_4$ Thin Film Electrode Prepared by Pulsed Laser Deposition. *Electrochem. Commun.* **2003**, *5*, 502.

(28) Abe, T.; Fukuda, H.; Iriyama, Y.; Ogumi, Z. Solvated Li-ion Transfer at Interface between Graphite and Electrolyte. *J. Electrochem. Soc.* **2004**, *151*, A1120.

(29) Yamada, Y.; Iriyama, Y.; Abe, T.; Ogumi, Z. Kinetics of Lithium Ion Transfer at the Interface between Graphite and Liquid Electrolytes: Effects of Solvent and Surface Film. *Langmuir* **2009**, *25*, 12766.

(30) Mizuno, Y.; Okubo, M.; Hosono, E.; Kudo, T.; Zhou, H.; Oh-Ishi, K. Suppressed Activation Energy for Interfacial Charge Transfer of a Prussian Blue Analog Thin Film Electrode with Hydrated Ions (Li^+, Na^+, and Mg^{2+}). *J. Phys. Chem. C* **2013**, *117*, 10877.

(31) Lindström, H.; Södergren, S.; Solbrand, A.; Rensmo, H.; Hjulm, J.; Hagfeldt, A.; Lindquist, S. Li^+ Ion Insertion in TiO_2 (Anatase). *J. Phys. Chem. B* **1997**, *101*, 7717.

(32) Brezesinski, T.; Wang, J.; Tolbert, S. H.; Dunn, B. Ordered mesoporous α-MoO_3 with Iso-Oriented Nanocrystalline Walls for Thin-Film Pseudocapacitors. *Nat. Mater.* **2010**, *9*, 146.

(33) Luzar, A.; Chandler, D. Hydrogen-Bond Kinetics in Liquid Water. *Nature* **1996**, *379*, 55.

(34) Marcus, Y. Effect of Ions on the Structure of Water: Structure Making and Breaking. *Chem. Rev.* **2009**, *109*, 1346.

(35) Suresh, S. J.; Naik, V. M. Hydrogen Bond Thermodynamic Properties of Water from Dielectric Constant Data. *J. Chem. Phys.* **2000**, *113*, 9727.

(36) Frank, H. S.; Wen, W.-Y. Ion-Solvent Interaction. Structural Aspects of Ion-Solvent Interaction in Aqueous Solutions: A Suggested Picture of Water Structure. *Discuss. Faraday Soc.* **1957**, *24*, 133.

(37) Toney, M. F.; Howard, J. N.; Richer, J.; Borges, G. L.; Gordon, J. G.; Melroy, O. R.; Wiesler, D. G.; Yee, D.; Sorensen, L. B. Voltage-Dependent Ordering of Water Molecules at an Electrode–Electrolyte Interface. *Nature* **1994**, *368*, 444.

(38) Bjerrum, N. The Electric Forces between the Ions and Their Effects. *Ergebnisse der exakten naturwissenschaften* **1926**, *6*, 125.

(39) Hasted, J. B.; Ritson, D. M.; Collie, C. H. Dielectric Properties of Aqueous Ionic Solutions. *J. Chem. Phys.* **1948**, *16*, 1.

(40) Suo, L.; Oh, D.; Lin, Y.; Zhuo, Z.; Borodin, O.; Gao, T.; Wang, F.; Kushima, A.; Wang, Z.; Kim, H. C.; Qi, Y.; Yang, W.; Pan, F.; Li, J.; Xu, K.; Wang, C. How Solid-Electrolyte Interphase Forms in Aqueous Electrolytes. *J. Am. Chem. Soc.* **2017**, *139*, 18670.

(41) Lukatskaya, M. R.; Feldblyum, J. I.; Mackanic, D. G.; Lissel, F.; Michels, D. L.; Cui, Y.; Bao, Z. Concentrated Mixed Cation Acetate "Water-In-Salt" Solutions as Green and Low-Cost High Voltage Electrolytes for Aqueous Batteries. *Energy Environ. Sci.* **2018**, *11*, 2876.

(42) Dou, Q.; Lei, S.; Wang, D. W.; Zhang, Q.; Xiao, D.; Guo, H.; Wang, A.; Yang, H.; Li, Y.; Shi, S.; Yan, X. Safe and High-Rate Supercapacitors Based on an "Acetonitrile/Water-In-Salt" Hybrid Electrolyte. *Energy Environ. Sci.* **2018**, *11*, 3212.

Chapter 5: Topochemical synthesis of phase-pure Mo_2AlB_2 through staging mechanism

5.1 Introduction

2D materials such as graphene,[1,2] transition-metal dichalcogenides (TMDs),[3,4] and hexagonal boron nitride (h-BN)[5,6] have incresingly attracted interest owing to their possible widespread use in various applications including electronics, energy conversion, environment, and energy storage: Atomically thin 2D morphology yields unique physical and chemical properties that are distinct from those of conventional three-dimensional materials.[7,8]

Since the discovery by the research group led by Gogotsi and Barsoum in 2011, transition metal carbides and nitrides, collectively called as MXenes, have emerged as a new class of 2D materials.[9] As MXenes are synthesized by removing Al, Si or Ga layers from layered carbides and nitrides (MAX phases $M_{n+1}AX_n$, M: Ti, V, Cr, Zr, Nb, Mo, Ta; A: Al, Si, Ga; X : C, N; n = 1, 2, or 3), MXenes consist of 2D nanosheets with a general formula of $M_{n+1}X_nT_x$ (T_x (surface termination group): OH, O, F, Cl), and their compositional and structural versatility allows alteration of physical and chemical properties as shown in **Figure 5.1**.[10-22] For example, the ion storage ability of MXenes for battery and supercapacitor applications can significantly be enhanced by changing M, X, T_x or n.[23,24] Therefore, of essential importance at this early stage of the development of MXenes is to extend a range of their chemical composition. Nontheless, albeit a relatively wide range of choice in M, T_x and n, severe limiation presently applies to X, wherein MXenes accomodate only X = C and N. As a valence band of MXenes is comprised of the 2p orbital of X hybridized with the d orbital of M, MXenes with different X should drastically modulate the electronic structure.[25]

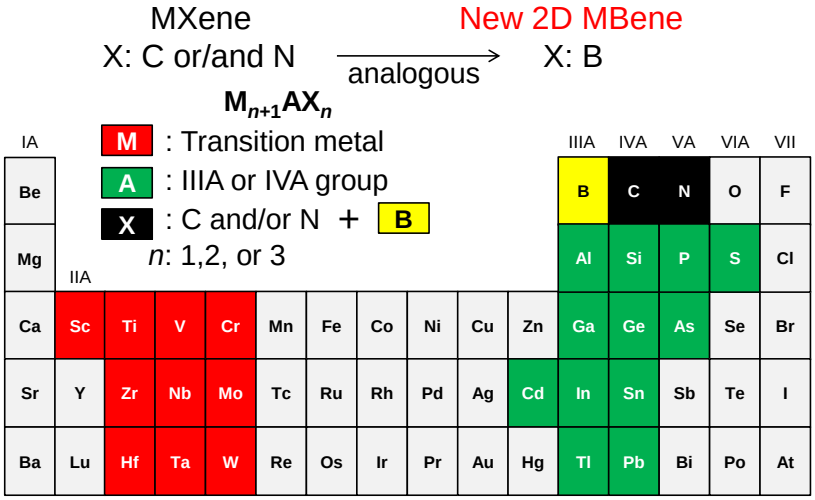

Figure 5.1 A variety of combination for MXene ($M_{n+1}X_nT_x$) including X: B (MBene).

In this context, it has been an aspirational goal to synthesize MXene with X = B, referred to as MBenes as shown in **Figure 5.1**, which can provide favorable properties for energy storage applications. Indeed, theoretical calculations predicted that MBenes have high electronic conductivity and a large capacity of Li-ion storage.[26] It was expected, in analogy with the synthesis of MXenes from MAX phases, that MBenes could be synthesized by the removal of Al layers from layered binary borides (MAB phases M_nAlB_m) as shown in **Figure 5.2**.[27-34]

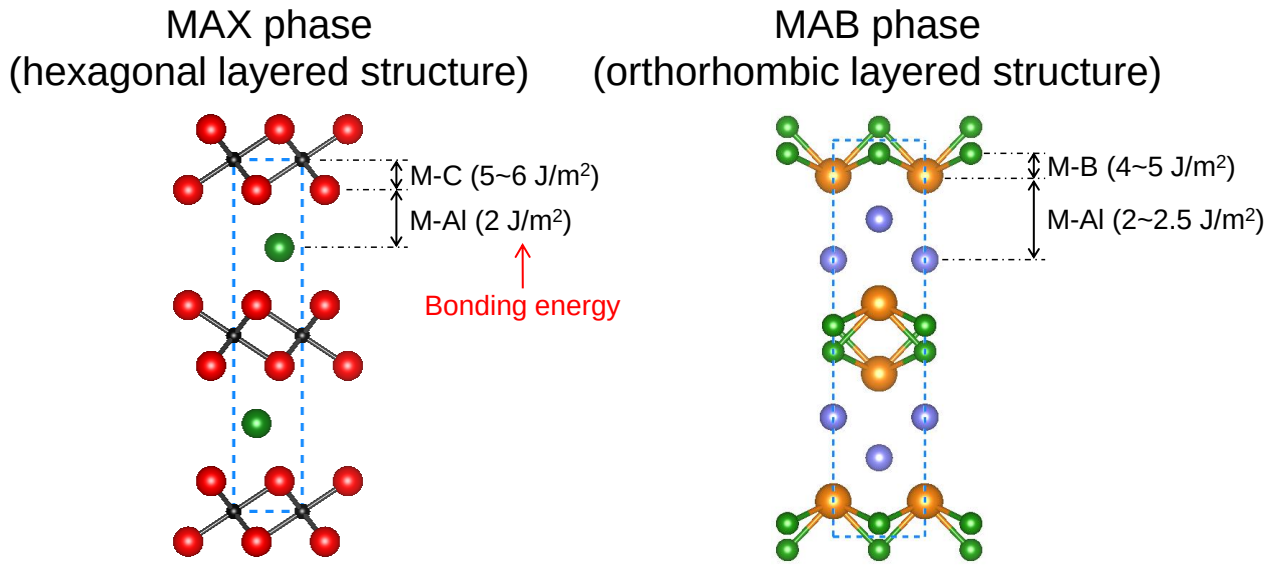

Figure 5.2 Similar to MAX phase with a hexagonal layered structure, MAB phase exhibits an orthorhombic layered structure where Al layers are interleaved between transition-metal boride (MB) slabs. Based on first-principle calculations, it is expected that 2D MBene could be synthesized by selective Al etching in MAB phase because bonding energies of M-B and M-Al for a MAB phase are analogous to those of M-C and M-Al for a MAX phase.

However, a pioneering work to remove Al layers from a MoAlB single crystal by Alameda *et al.*[35] revealed that MBene could not be obtained directly from MoAlB becaues of a structural difference in the Al layers between MAX and MAB phases: MAX phases have a single Al layer while MAB phases have a zigzag double Al layer. Therefore, Alameda *et al.*[36] proposed to synthesize a MAB phase with a single Al layer as a precursor for Mbenes. However, because of their thermodynamically metastable nature, the phase-pure synthesis of an MAB phase with a single Al layer has not been established.

In this work, I report the topochemical synthesis of phase-pure Mo_2AlB_2, an MAB phase with a single Al layer, as a possible presursor for MBenes. I also show the possible elemental steps upon topochemical transformation from MoAlB to Mo_2AlB_2 using theoretical calculations.

5.2 Synthesis of MAB phase MoAlB and Mo_2AlB_2

An MAB phase, MoAlB with a zigzag double Al layer, was synthesized by heating the mixture of MoB and Al at 1200 ℃ for 1 h under Ar atmosphere using a high-frequency induction furnace. Mo_2AlB_2 with a single Al layer was synthesized topochemically by removing Al layers from MoAlB: powdered MoAlB was treated with an etchant LiF/HCl aqueous solution (**Figure 5.3**). The intensive optimization of synthetic conditions determined that etching with a concentrated etchant (3 M LiF/10 M HCl solution) at elevated temperature of 40 ℃ for more than 48 h is necessary for the complete transformation.

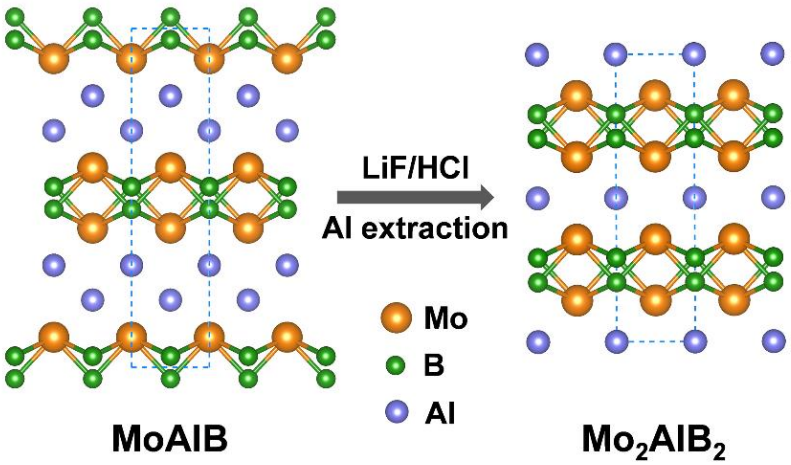

Figure 5.3 Schematic design for the synthesis of Mo_2AlB_2 treated by LiF/HCl from MAB phase MoAlB.

The powder X-ray diffraction (XRD) pattern for MoAlB (**Figure 5.4**) is fully indexed to orthorhombic *Cmcm*, indicating the successful synthesis of MoAlB.[28] It should be noted that energy-dispersive X-ray (EDX) analysis shows the existence of surface-segregated oxygen (**Figure 5.5**). The XRD patterns in **Figure 5.4** show that a 020 diffraction peak at 2θ = 12.6° for MoAlB shifts to 13.6° after the etching process. Based on the 020 diffraction corresponding to the interlayer distance (d_{inter}) of MoB layers, d_{inter} decreases from 7.1 Å to 6.1 Å, suggesting successful removal of Al layers from MoAlB.

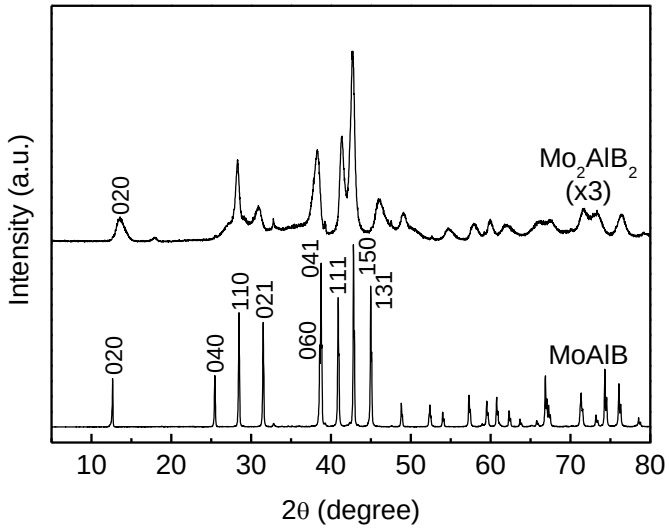

Figure 5.4 XRD patterns of MoAlB and Mo_2AlB_2. 020 diffraction peak shifts to higher angle, indicating shrinkage of interlayer distance due to an Al layer loss.

Indeed, energy-dispersive X-ray (EDX) analysis (**Figure 5.5**) revealed that the atomic ratio of Mo/Al increases from 1.0 for MoAlB to 2.0 for the product, which confirms the formation of Mo_2AlB_2 by the removal of Al layers from MoAlB. Importantly, as a single 020 diffraction peak was observed for the XRD pattern of the product, MoAlB was completely transformed to phase-pure Mo_2AlB_2. Using a MoAlB single crystal as precursor, Alameda *et al.* found the formation of several unidentified intergrowth phases of Mo_2AlB_2, $Mo_3Al_2B_3$, $Mo_4Al_3B_4$, and $Mo_6Al_5B_6$.[36] In contrast, this work successfully isolated phase-pure Mo_2AlB_2 under the optimized synthetic conditions including etchant concentration, temperature, and reaction duration time.

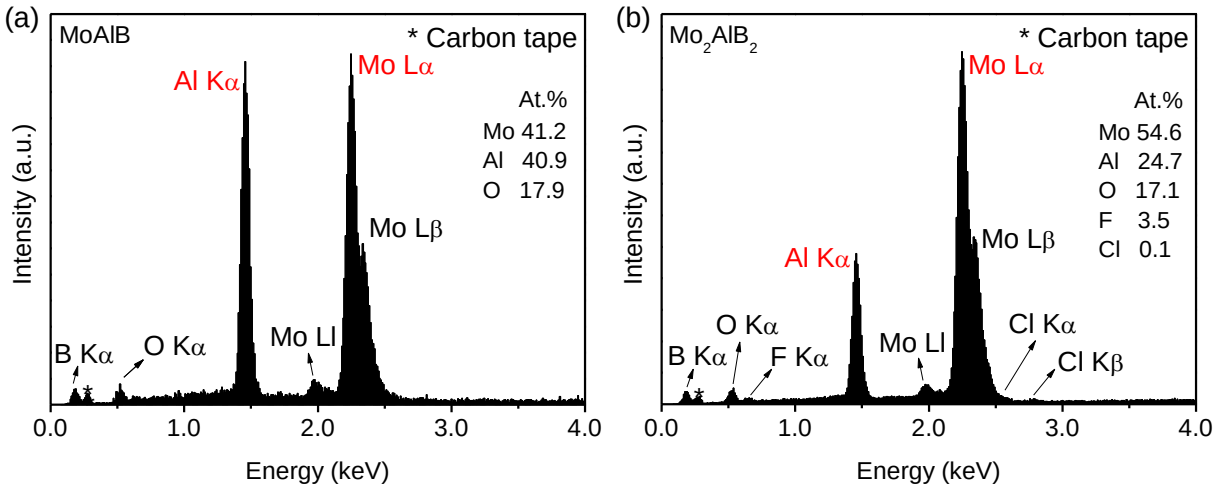

Figure 5.5 EDX results for (a) MoAlB and (b) Mo_2AlB_2.

Scanning electron microscopy (SEM) images (**Figures 5.6a** and **5.6b**) show that the flake morphology of MoAlB changes to the partially exfoliated morphology of Mo_2AlB_2 presumably due to the formation of etched cavities as reported previously.[35,36] Transmission electron microscopy (TEM) images (**Figures 5.6c** and **5.6d**) indicate that the layered structure of MoAlB is maintained after the etching process. The observed d_{inter} are 7.1 and 6.4 Å for MoAlB and Mo_2AlB_2, respectively, which are in complete agreement with the XRD results (**Figure 5.4**). Furthermore, the TEM-EDS analysis confirmed that the oxygen detected in SEM-EDX is a minority element (3.2% per total atoms). Therefore, all the experimental observations support that the MoAlB with a zigzag double Al layer is transformed to Mo_2AlB_2 with a single Al layer topochemically, *i.e.*, maintaining the stacking structure of MoB layers, (**Figure 5.3**). As the single Al layer of Mo_2AlB_2 is identical with that of MAX phases, Mo_2AlB_2 is a possible precursor for MBenes.

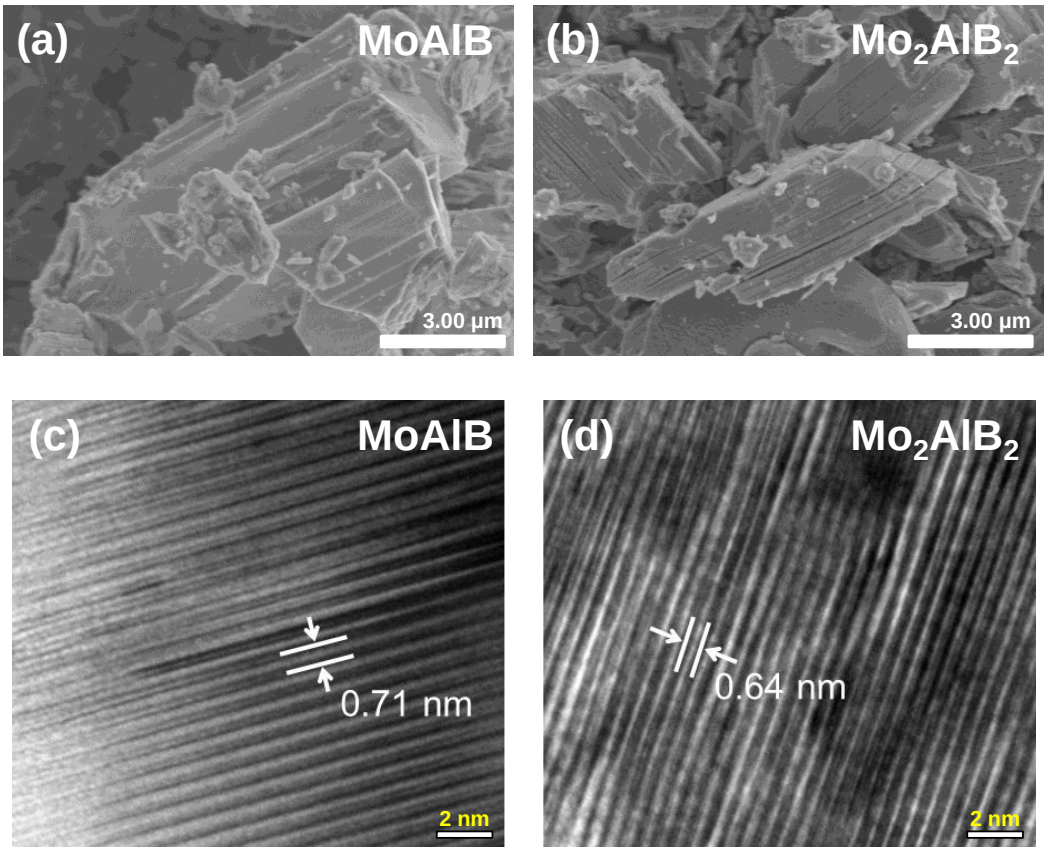

Figure 5.6 SEM images of (a) MoAlB and (b) Mo_2AlB_2, and TEM images of (c) MoAlB and (d) Mo_2AlB_2.

5.3 Sequential staging transformation

Figure 5.7 shows the power X-ray diffraction pattern of the samples with different etching times (0, 24, 48, and 144 h). The XRD pattern for the sample after 24 h etching shows the coexistence of a phase with an intermediate interlayer distance of d_{inter} = 6.8 Å , suggesting the formation of $Mo_4Al_3B_4$ (stage II) before the formation of Mo_2AlB_2 (stage I). Indeed, this XRD results support staging transformation mechanism proposed using *ex situ* annular dark-field scanning transmission electron microscopy (ADF-STEM).[36] However, the XRD pattern for the sample after an etching time of 144 h exhibits no further change of interlayer distance same with that of the sample after an etching time of 24 h, indicating a thermodynamically stable compound of Mo_2AlB_2. Therefore, other harsh etching condition might be needed for fully-etching of Al layers to synthesize the 2D MBene.

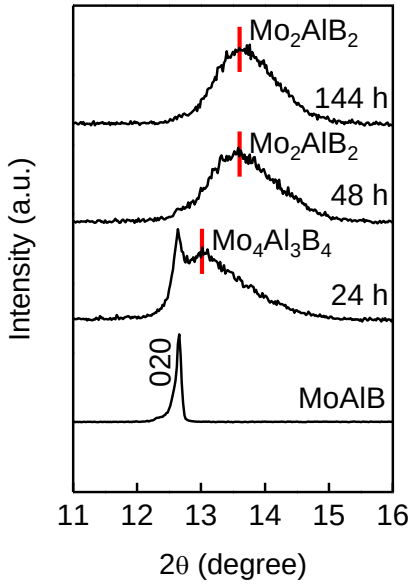

Figure 5.7 Powder X-ray diffraction patterns for MoAlB, the sample after 24 h etching, the sample after 48 h etching, and the sample after 144 h. After 24 h etching, a new diffraction peak appears at 2θ = 13°, corresponding to the interlayer distance of d_{inter} = 6.8 Å (presumably, $Mo_4Al_3B_4$). Based on XRD and ADF-STEM results, staging transformation from MoAlB through $Mo_4Al_3B_4$ to Mo_2AlB_2 should occur.

5.4 Conclusion

Phase-pure Mo_2AlB_2 with a single Al layer was synthesized topochemically by removing an Al layer from a zigzag double Al layer in MoAlB. XRD and ADF-STEM results predicted that the transformation from MoAlB to Mo_2AlB_2 proceeds through a staging route rather than generating random Al defects in the zigzag double Al layer. As Mo_2AlB_2 has a single Al layer which is identical with MAX phases, it can be a precursor to form MBene under an appropriate etching condition.

Reference

(1) Geim, A. K. Graphene : Status and Prospects. *Science* **2009**, *324*, 1530–1535.

(2) Stankovich, S.; Dikin, D. A.; Dommett, G. H. B.; Kohlhaas, K. M.; Zimney, E. J.; Stach, E. A.; Piner, R. D.; Nguyen, S. T.; Ruoff, R. S. Graphene-Based Composite Materials. *Nature* **2006**, *442*, 282-286.

(3) Wang, Q. H.; Kalantar-zadeh, K.; Kis, A.; Coleman, J. N.; Strano, M. S. Electronics and Optoelectronics of Two-Dimensional Transition Metal Dichalcogenides. *Nat. Nanotechnol.* **2012**, *7*, 699–712.

(4) Bhimanapati, G. R.; Lin, Z.; Meunier, V.; Jung, Y.; Cha, J.; Das, S.; Xiao, D.; Son, Y.; Strano, X. M. S.; Cooper, V. R.; Liang, L.; Louie, S. G.; Ringe, E.; Zhou, W.; Kim, S. S.; Naik, R. R.; Sumpter, B. G.; Terrones, H.; Xia, F.; Wang, Y.; Zhu, J.; Akinwande, D.; Alem, N.; Schuller, J. A.; Schaak, R. E.; Terrones, M.; Robinson, J. A. Recent Advances in Two-Dimensional Materials beyond Graphene. *ACS Nano* **2015**, *12*, 11509–11539.

(5) Dean, C. R.; Young, A. F.; Meric, I.; Lee, C.; Wang, L.; Sorgenfrei, S.; Watanabe, K.; Taniguchi, T.; Kim, P.; Shepard, K. L.; Hone, J. Boron Nitride Substrates for High-Quality Graphene Electronics. *Nat. Nanotechnol.* **2010**, *5*, 722-726.

(6) Giovannetti, G.; Khomyakov, P. A.; Brocks, G.; Kelly, P. J.; Brink, J. V. D. Substrate-Induced Band Gap in Graphene on Hexagonal Boron Nitride : *Ab Initio* Density Functional Calculations. *Phys. Rev. B* **2007**, *76*, 073103.

(7) Koski, K. J.; Cui, Y. *ACS Nano* **2013**, *7*, 3739–3743.

(8) Xu, M.; Liang, T.; Shi, M.; Chen, H. Graphene-Like Two-Dimensional Materials. *Chem. Rev.* **2013**. *113*, 3766-3798.

(9) Naguib, M.; Kurtoglu, M.; Presser, V.; Lu, J.; Niu, J.; Heon, M.; Hultman, L.; Gogotsi, Y.; Barsoum, M. W. Two-Dimensional Nanocrystals Produced by Exfoliation of Ti_3AlC_2. *Adv. Mater.* **2011**, 4248–4253.

(10) Naguib, M.; Mashtalir, O.; Carle, J.; Presser, V.; Lu, J.; Hultman, L.; Gogotsi, Y.; Barsoum, M. W. Two-Dimensional Transition Metal Carbides. *ACS Nano* **2012**, *6*, 1322–1331.

(11) Lukatskaya, M. R.; Mashtalir, O.; Ren, C. E.; Agnese, Y. D.; Rozier, P.; Taberna, P. L.; Naguib,

M.; Simon, P.; Barsoum, M. W.; Gogotsi, Y. Cation Intercalation and High Volumetric Capacitance of Two-Dimensional Titanium Carbide. *Science* **2013**, *341*, 1502-1505.

(12) Mashtalir, O.; Naguib, M.; Mochalin, V. N.; Agnese, Y. D.; Heon, M.; Barsoum, M. W.; Gogotsi, Y. Intercalation and Delamination of Layered Carbides and Carbonitrides. *Nat. Commun.* **2013**, *4*, 1716.

(13) Naguib, M.; Mochalin, V. N.; Barsoum, M. W.; Gogotsi, Y. 25th Anniversary Article: MXenes: A New Family of Two-Dimensional Materials. *Adv. Mater.* **2014**, 26, 992–1005.

(14) Ghidiu, M.; Lukatskaya, M. R.; Zhao, M.-Q.; Gogotsi, Y.; Barsoum, M. W. Conductive Two-Dimensional Titanium Carbide 'Clay' with High Volumetric Capacitance. *Nature* **2014**, *516*, 78–81.

(15) Naguib, M.; Halim, J.; Lu, J.; Cook, K. M.; Hultman, L.; Gogotsi, Y.; Barsoum, M. W. New Two-Dimensional Niobium and Vanadium Carbides as Promising Materials for Li-Ion Batteries. *J. Am. Chem. Soc.* **2013**, *135*, 15966-15969.

(16) Wang, X.; Kajiyama, S.; Iinuma, H.; Hosono, E.; Oro, S.; Moriguchi, I.; Okubo, M.; Yamada, A. Pseudocapacitance of MXene Nanosheets for High-Power Sodium-Ion Hybrid Capacitors. *Nat. Commun.* **2015**, *6*, 6544.

(17) Seh, Z. W.; Fredrickson, K. D.; Anasori, B.; Kibsgaard, J.; Strickler, A. L.; Lukatskaya, M. R.; Gogotsi, Y.; Jaramillo, T. F.; Vojvodic, A. Two-Dimensional Molybdenum Carbide (MXene) as an Efficient Electrocatalyst for Hydrogen Evolution. *ACS Energy Lett.* **2016**, *1*, 589-594.

(18) Mashtalir, O.; Lukatskaya, M. R.; Zhao, M.-Q.; Barsoum, M. W.; Gogotsi, Y. Amine-Assisted Delamination of Nb_2C MXene for Li-Ion Energy Storage Devices. *Adv. Mater.* **2015**, *27*, 3501–3506.

(19) Anasori, B.; Lukatskaya, M. R.; Gogotsi, Y. 2D Metal Carbides and Nitrides (MXenes) for Energy Storage. *Nat. Rev. Mater.* **2017**, *2*, 16098.

(20) Okubo, M.; Sugahara, A.; Kajiyama, S.; Yamada, A. MXene as a Charge Storage Host. *Acc. Chem. Res.* **2018**, *51*, 591-599.

(21) Kajiyama, S.; Szabova, L.; Sodeyama, K.; Iinuma, H.; Morita, R.; Gotoh, K.; Tateyama, Y.; Okubo, M.; Yamada, A. Sodium-Ion Intercalation Mechanism in MXene Nanosheets. *ACS Nano* **2016**, *10*, 3334–3341.

(22) Sugahara, A.; Ando, Y.; Kajiyama, S.; Yazawa, K.; Gotoh, K.; Otani, M.; Okubo, M.; Yamada, A. Negative Dielectric Constant of Water Confined in Nanosheets. *Nat. Commun.* **2019**, *10*, 850.

(23) Kajiyama, S.; Szabova, L.; Iinuma, H.; Sugahara, A.; Gotoh, K.; Sodeyama, K.; Tateyama, Y.; Okubo, M.; Yamada, A. Enhanced Li-Ion Accessibility in MXene Titanium Carbide by Steric Chloride Termination. *Adv. Energy Mater.* **2017**, 1601873.

(24) Hart, J. L.; Hantanasirisakul, K.; Lang, A. C.; Anasori, B.; Pinto, D.; Pivak, Y.; Omme, J. T. V.; May, S. J.; Gogotsi, Y.; Taheri, M. L. Control of MXenes' Electronic Properties through Termination and Intercalation. *Nat. Commun.* **2019**, *10*, 522.

(25) Khazaei, M.; Ranjbar, A.; Arai, M.; Yunoki, S. Electronic Properties and Applications of MXenes: a Theoretical Review. *J. Mater. Chem. C* **2017**, *5*, 2488–2503.

(26) Guo, Z.; Zhou, J.; Sun, Z. New Two-Dimensional Transition Metal Borides for Li Ion Batteries and Electrocatalysis. *J. Mater. Chem. A Mater.* **2017**, *5*, 23530–23535.

(27) Ade, M.; Hillebrecht, H. Ternary Borides Cr_2AlB_2, Cr_3AlB_4, and Cr_4AlB_6: The First Members of the Series $(CrB_2)_nCrAl$ with n = 1, 2, 3 and a Unifying Concept for Ternary Borides as MAB-Phases. *Inorg. Chem.* **2015**. *54*, 6122-6135.

(28) Kota, S.; Zapata-solvas, E.; Ly, A.; Lu, J.; Elkassabany, O.; Huon, A.; Lee, W. E.; Hultman, L.; May, S. J.; Barsoum, M. W. Synthesis and Characterization of an Alumina Forming Nanolaminated Boride: MoAlB. *Sci. Rep.*, **2016**, *6*, 26475.

(29) Kádas, K.; luşan, D.; Hellsvik, J.; Cedervall, J.; Berastegui, P.; Sahlberg, M.; Jansson, U.; Eriksson, O. AlM_2B_2 (M = Cr, Mn, Fe, Co, Ni): a Group of Nanolaminated Materials. *J. Phys.: Condens. Matter* **2017**, *29*, 155402.

(30) Lu, J.; Kota, S.; Barsoum, M. W.; Hultman, L. Atomic Structure and Lattice Defects in Nanolaminated Ternary Transition Metal Borides. *Mater. Res. Lett.* **2017**, *5*, 235-241.

(31) Zhou, Y.; Xiang, H.; Dai, F.-Z.; Feng, Z. Electrical Conductive and Damage-Tolerant Nanolaminated MAB Phases Cr_2AlB_2, Cr_3AlB_4 and Cr_4AlB_6. *Mater. Res. Lett.* **2017**, *5*, 440-448.

(32) Ke, L.; Harmon, B. N.; Kramer, M. J. Electronic Structure and Magnetic Properties in T_2AlB_2 (T = Fe, Mn, Cr, Co, and Ni) and Their Alloys. *Phys. Rev. B* **2017**, *95*, 104427.

(33) Zhang, H.; Xiang, H.; Dai, F.-Z.; Zhang, Z.; Zhou, Y. First Demonstration of Possible

Two-Dimensional MBene CrB Derived from MAB Phase Cr_2AlB_2. *J. Mater. Sci. Technol.* **2018**, *34*, 2022-2026.

(34) Chai, P.; Stoian, S. A.; Tan, X.; Dube, P. A.; Shatruk, M. Investigation of Magnetic Properties and Electronic Structure of Layered-Structure Borides AlT_2B_2 (T = Fe, Mn, Cr) and $AlFe_{2-x}Mn_xB_2$. *J. Solid State Chem.* **2015**, *224*, 52-61.

(35) Alameda, L. T.; Holder, C. F.; Fenton, J. L.; Schaak, R. E. Partial Etching of Al from MoAlB Single Crystals to Expose Catalytically Active Basal Planes for the Hydrogen Evolution Reaction. *Chem. Mater.* **2017**, *29*, 8953–8957.

(36) Alameda, L. T.; Moradifar, P.; Metzger, Z. P.; Alem, N.; Schaak, R. E. Topochemical Deintercalation of Al from MoAlB: Stepwise Etching Pathway, Layered Intergrowth Structures, and Two-Dimensional MBene. *J. Am. Chem. Soc.* **2018**, *140*, 8833–8840.

Chapter 6: General conclusion

6.1 Conclusions in this study

The main perspective of this thesis was to develop MXene/concentrated aqueous electrolyte system because MXenes are promising materials to give large amounts of active sites for energy storage and the wide electrochemical potential window was provided by concentrated electrolytes.

Due to light gravimetric weight of a MXene Ti_2CT_x, its cyclic voltammetry curve exhibited the highest averaged capacitance (168 F/g) among $Ti_3C_2T_x$, Nb_2CT_x, and Mo_2CT_x. Many kinds of cation (Li, Na, K, Mg, Ca, and Zn) were investigated because large interlayer distance provide intercalation/deintercalation pathway of various chemical species. Although ZnTFSI system offered the largest capacitance (> 200 F/g), it was proved that ZnTFSI system easily becomes acidic atmosphere when dissolved in water; the largest capacitance could be attributed to redox reaction between proton and surface termination of MXenes. Thus, Ti_2CT_x/Zn system showed narrow electrochemical potential window because of hydrogen evolution in acidic atmosphere.

Taking advantage of wide operating potential of a hydrate melt, Ti_2CT_x has a capacity of 60 mAh/g at a specific current rate of 30mA/g three times larger than that of a 1 M Li_2SO_4 commercial aqueous electrolyte. MXene aqueous supercapacitor (Ti_2CT_x|hydrate melt|AC) with a hydrate melt also shows a higher energy density (> 15 Wh/kg) at a scan rate of 100 W/kg compared to that of 1 M Li_2SO_4 aqueous electrolyte. However, capacity of Ti_2CT_x is decreased dramatically at high current densities in a hydrate melt electrolyte.

To clarify capacity decay mechanism, interfacial charge transfer was investigated in dilute and concentrated systems based on temperature-dependent EIS analysis. Concentrated system showed much higher activation energy of charge transfer than that of dilute system. Based on Raman spectroscopy, interaction between anions and hydrated-Li^+ hinders the transportation of charges into the electrode. To enhance performances of MXene/concentrated system, hydrogen evolution should be suppressed by stable SEI formation while interaction between anions and hydrated-Li^+ should be reduced.

Since the report on high energy storage capability of MBenes based on first principle calculations, several studies on synthesis of MBenes have been conducted; however, fully-etching of Al layers from the MAB phase has not been reported. In this regard, the synthesis of 2D MBene was challenged with a MAB phase MoAlB.

Through the intensive optimization for etching process of MoAlB, pure-phase Mo_2AlB_2 has first

been successfully synthesized as a possible precursor of 2D MBene; however, further studies on optimization of etching process (*e.g.*, etching time, etching temperature, and etchants) are required to synthesize 2D MBene with fully-etching of Al layers from MoAlB.

6.2 Outlook

Although Ti_2CT_x/hydrate-melt system showed higher voltage operation and higher energy density with good cycle retention compared to those of a commercial 1 M Li_2SO_4 aqueous electrolyte, further studies on aqueous electrolytes and MXenes are required to enhance power density without sacrificing the high voltage operation for high-performance supercapacitors.

Aqueous electrolytes

Generally, aqueous electrolytes provide higher ionic conductivity than that of non-aqueous electrolytes; however, their operating potential is limited by the narrow electrochemical potential window of water, leading to low energy density. Although super-concentrated aqueous electrolyte (*e.g.*, a hydrate melt) exhibited high operation voltage as described in this work, there are still the number of requirements that should be addressed to enhance power density without sacrificing the electrochemical potential window for high-performance aqueous supercapacitors; i) stable SEI film should be formed on the electrode to suppress hydrogen evolution. ii) interfacial charge transfer resistance and bulk electrolyte charge transfer resistance should be minimized.

Exploring of new combination of MXenes

Novel MXenes could grant favorable properties (e.g., high electric conductivity, high charge storage capability) for energy storage applications. Over 60 different pure MAX phases have been reported up to now. Considering their combination of solid solution of transition-metal and mixing carbon/nitrogen, numerous MAX phases can be synthesized. The intensive optimization of etching process using different bonding energy of M-A and M-X could provide successful synthesis of new MXenes. Furthermore, new 2D compounds MXene with X = B (referred to as MBene) would be candidates, which can provide extraordinary properties for supercapacitors.

Tuning of MXenes

The versatile chemistry of MXenes offers new properties, which can be favorable to improve energy storage capability. Surface termination groups of MXenes can affect electrochemical performances by controlling electronic structure and by donating electrons to hydrated-cations. For

example, lower electronegativity with surface termination groups (*e.g.*, $Br^- < Cl^- < F^-$) can reduce Coulombic repulsion of intercalated-cations each other, leading to large amounts of charge storage in the MXene interlayers. Moreover, surface termination groups with larger atomic size provide larger interlayer distance, which can offer good ion accessibility in MXene interlayers.

Because MXenes have large interlayer distance, many chemical species have been reported as intercalants (*e.g.*, dimethyl sulfoxide, urea, hydrazine, long-chain alkylamines, *etc.*). These intercalants may not only enlarge the MXene interlayers but also make them transformed from 2D channel to 3D network, which can be new MXene hosts for new types of supercapacitors (*e.g.*, Ca-, Zn-, and Mg-ion supercapacitor).

Finally, multi-layered $Ti_3C_2T_x$ MXene can be easily delaminated by hand-shaking or sonication, which can provide high specific surface area and high electrical conductivity. Taking these advantages, they can be used as a conductive agent to enhance electrochemical performances.

Appendix A: MXene electrode with hybrid electrolyte (acetonitrile/hydrate-melt)

A hydrate melt electrolyte provides wider electrochemical potential window (-1.1 V vs. Ag/AgCl) than that of 1 M Li_2SO_4 aqueous electrolyte (-0.7 V vs. Ag/AgCl); however, low ionic conductivity and high charge transfer resistance coming from interaction between hydrated-Li^+ and anions lead to low power density. One approach to enhance power density without sacrificing high operation potential is to dilute a hydrate melt with miscible organic solvent (*e.g.*, acetonitrile).[1]

A.1 Liquid structure of hybrid electrolytes

A hydrate melt (28 m) and various concentrations (1, 5, 12, 20 m) of hybrid electrolyte (acetonitrile/hydrate-melt) were prepared by diluting a hydrate melt with an acetonitrile organic solvent. Hybrid electrolytes are referred as AHydrate-melt. **Figure A.1** shows the S-N-S bending vibration modes corresponding to the anion environment for pure acetonitrile, 1, 5, 12, 20 m AHydrate-melt, and a 28 m hydrate melt electrolytes. As electrolyte concentrations are diluted, the peaks shift to lower wave number far from that of hydrate melt electrolyte, indicating weakening of Li^+-anion interaction.

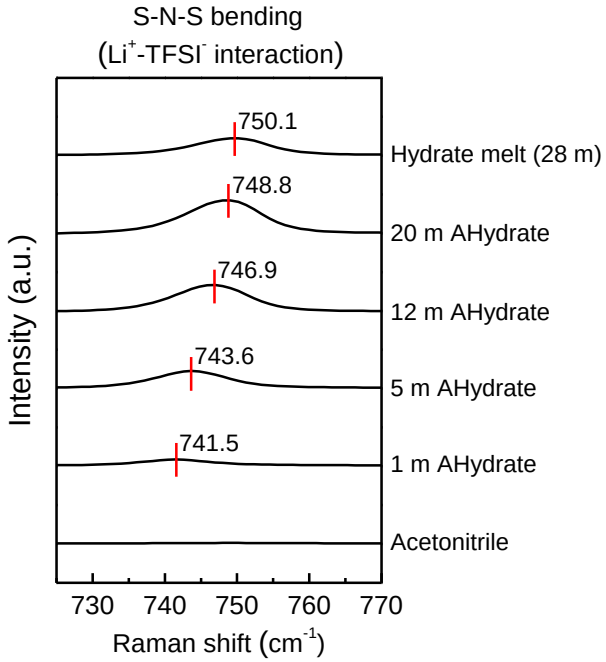

Figure A.1 Raman spectra of acetonitrile, 1, 5, 12, 20 m AHydrate, and a hydrate melt electrolytes in the region of S-N-S bending vibration.

Figure A.2 shows the O-H stretching vibration modes, indicating the existence of free water molecules. A 28 m hydrate melt shows the appearance of new peak around 3567 cm^{-1}, suggesting all water molecules are hydrated to Li^+ without any hydrogen bonding each other. As electrolyte concentrations are diluted, the peaks shift to lower wave number, indicating that hydration between Li^+ and water is weakened. However, the extent of weakening hydration between Li^+ and water is not severe until a 28 m hydrate melt electrolyte is diluted to the concentration of 5 m by acetonitrile.

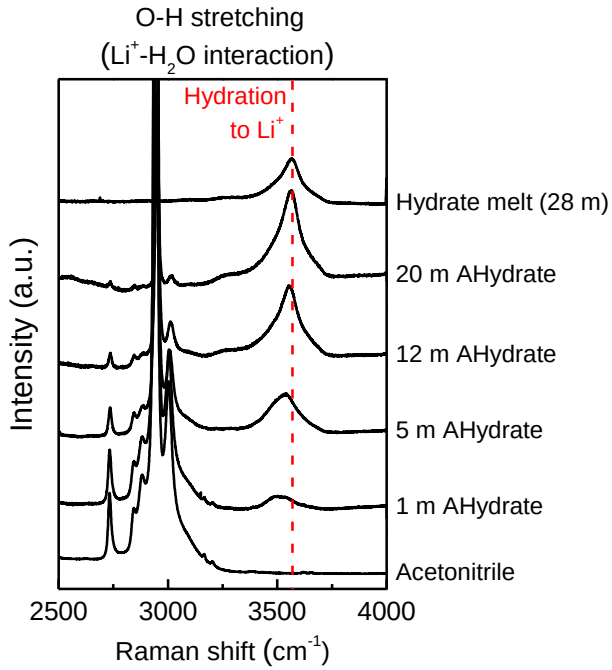

Figure A.2 Raman spectra of acetonitrile, 1, 5, 12, 20 m AHydrate, and a hydrate melt electrolytes in the region of O-H stretching vibration.

A.2 Electrochemical properties of MXenes in hybrid electrolytes

First of all, stable potential window of $Ti_3C_2T_x$ electrode was determined by chronoamperometry (red lines in **Figure A.3**, a steady-state cathodic current > –10 μA/cm^2) with a 5 m AHydrate-melt hybrid electrolyte. 5 m AHydrate-melt hybrid electrolyte shows wide operating potentials (-1.1 V vs. Ag/AgCl), which is same with that of hydrate melt.

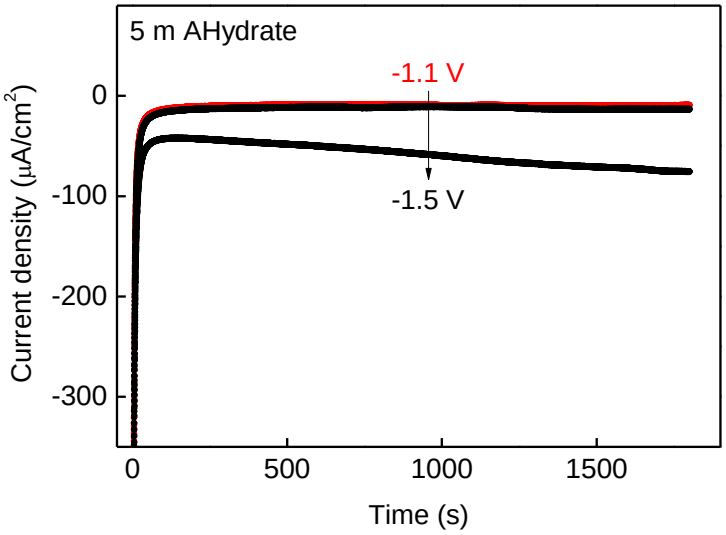

Figure A.3 Chronoamperometry of $Ti_3C_2T_x$ at various applied potentials vs. Ag/AgCl with a 5 m AHydrate-melt hybrid electrolyte. A red line exhibits negligible steady-state cathodic current less than -10 μA/cm^2, which determines a cut-off voltage.

After determination of stable potential window, cyclic voltammetry (CV) of $Ti_3C_2T_x$ electrode was measured with a 5 m AHydrate-melt hybrid electrolyte (**Figure A.4a-c**). For comparison, CVs of $Ti_3C_2T_x$ with 1 M LiTFSI and a 28 m hydrate melt aqueous electrolytes were also depicted. 5 m AHydrate-melt shows the similar degree of distorted curves at high scan rates with 1 M LiTFSI while the electrochemical potential window (-1.1 V vs. Ag/AgCl) is same with that of a 28 m hydrate melt. Averaged capacitances of $Ti_3C_2T_x$ with a 5 m AHydrate-melt hybrid electrolyte at a scan rate of 0.5 mV/s is 145.2 F/g. As shown in **Figure A.4d**, rate capability of $Ti_3C_2T_x$ with a 5 m AHydrate-melt hybrid electrolyte is comparable to that with 1 M LiTFSI. While a 5 m AHydrate-melt hybrid electrolyte offers high voltage operation of a $Ti_3C_2T_x$ electrode (-1.1 V vs. Ag/AgCl) same with that of a 28 m hydrate melt, rate capability is much improved.

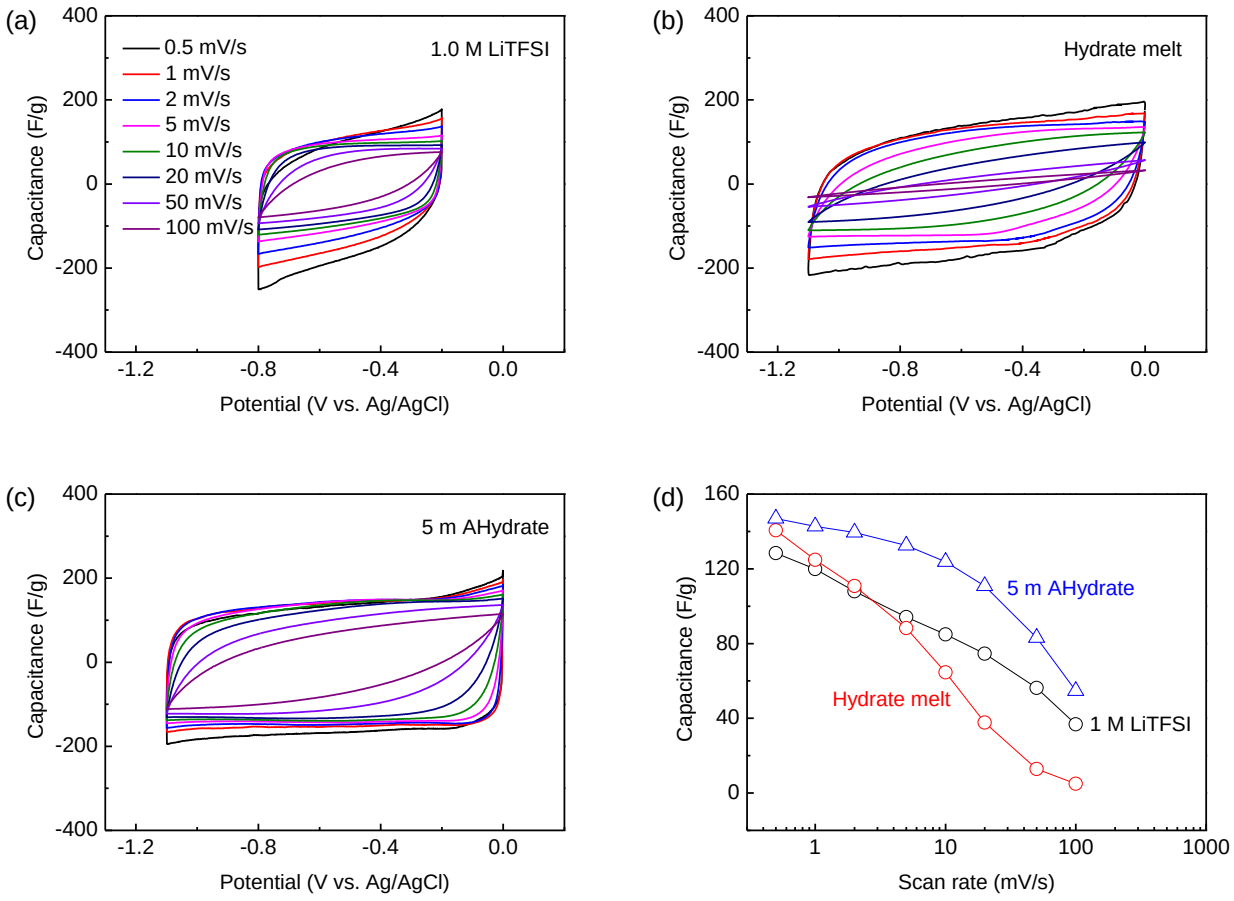

Figure A.4 Cyclic voltammograms for $Ti_3C_2T_x$ with (a) 1.0 M LiTFSI, (b) a hydrate melt and (c) 5 m AHydrate-melt electrolytes, and (d) rate capability at various scan rates of 0.5, 1, 2, 5, 10, 20, 50, and 100 mV/s.

Figure A.5 shows temperature-dependent EIS of $Ti_3C_2T_x$ electrode with a hydrate melt and a 5 m AHydrate-melt hybrid electrolyte. A 5 m AHydrate-melt hybrid electrolyte shows lower R_i and R_s than those of a hydrate melt. Based on Raman spectroscopy (**Figure A.1**), weakening the interaction between hydrated-Li^+ and anions brings about low resistance of interfacial charge transfer and bulk electrolyte, providing enhanced power density (**Figure A.4d**).

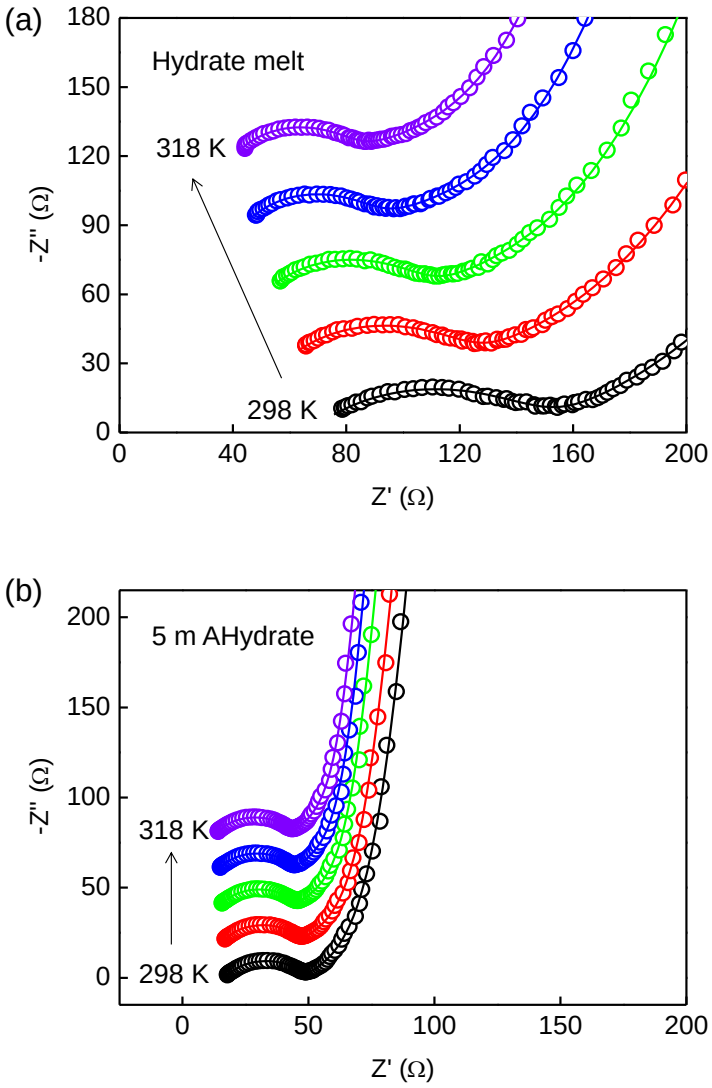

Figure A.5 Typical Nyquist plot for $Ti_3C_2T_x$ with (a) a hydrate melt and (b) a 5 m AHydrate-melt hybrid electrolyte at 298, 303, 308, 313, and 318 K.

Reference

(1) Dou, Q.; Lei, S.; Wang, D. W.; Zhang, Q.; Xiao, D.; Guo, H.; Wang, A.; Yang, H.; Li, Y.; Shi, S.; Yan, X. Safe and High-Rate Supercapacitors Based on An "Acetonitrile/Water-In-Salt" Hybrid Electrolyte. *Energy Environ. Sci.* **2018**, *11*, 3212-3219.

Appendix B: Power-law relationship in MXene electrode with non-aqueous electrolyte

Large interlayer distance of MXene offers great charge storage host with excellent ion accessibility and large amounts of active sites. While hydrated-cations are intercalated into MXene interlayers during charge process in aqueous system, M. Okubo *et al.*[1] reported solvated-cations are intercalated into MXene interlayers at initial charging and desolvation occurs at low potential region (*ca.* 1.0 V vs. Li^+/Li) in non-aqueous system. Therefore, EDL capacitance occurs at initial charging and is transferred to pseudocapacitance during further charging. Here, power-law relationship in MXene electrode is investigated with a different cut-off potential, indicating different charge storage mechanism between EDL capacitance and pseudocapacitance.

B.1 Cyclic voltammetry of MXenes

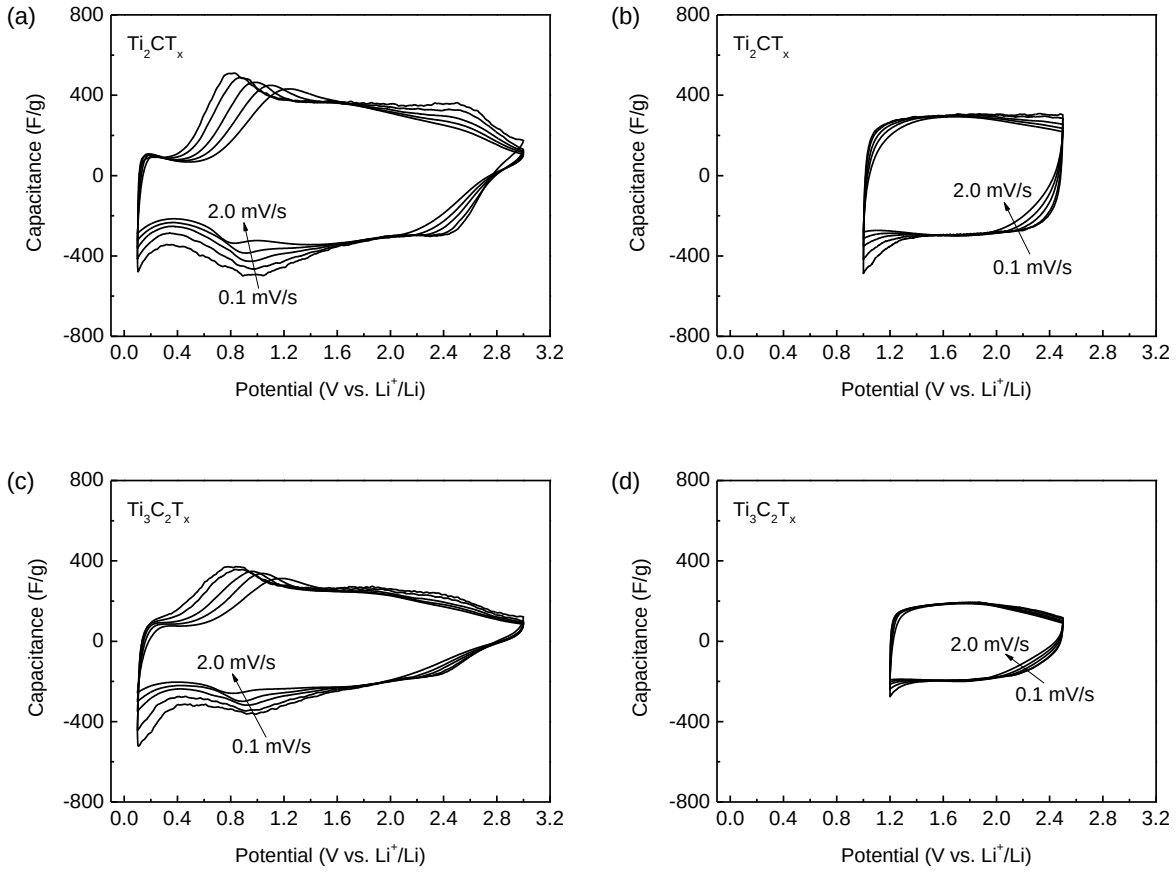

Figure B.1 Cyclic voltammograms of Ti_2CT_x in the potential range of (a) 0.1 – 3.0 V and (b) 1.0 – 2.5 V, and $Ti_3C_2T_x$ in the potential range of (c) 0.1 – 3.0 V and (d) 1.2 – 2.5 V with 1 M $LiPF_6$ in EC/DMC (vol.% 1/1).

Figure B.1 shows cyclic voltammograms of Ti_2CT_x and $Ti_3C_2T_x$ in different potential region with various scan rates of 0.1–2.0 mV/s. Low potential region (*ca.*, < 1.2 V vs. Li^+/Li) as shown in **Figure B.1a and B.1c** exhibits distorted rectangular CV shapes, indicating pseudocapacitance through orbital hybridization between Li^+ and MXene. On the other hand, **Figure B.1b and B.1d** shows rectangular CV shapes, which are characteristic of typical EDL capacitors.

B.2 *b*-value determination

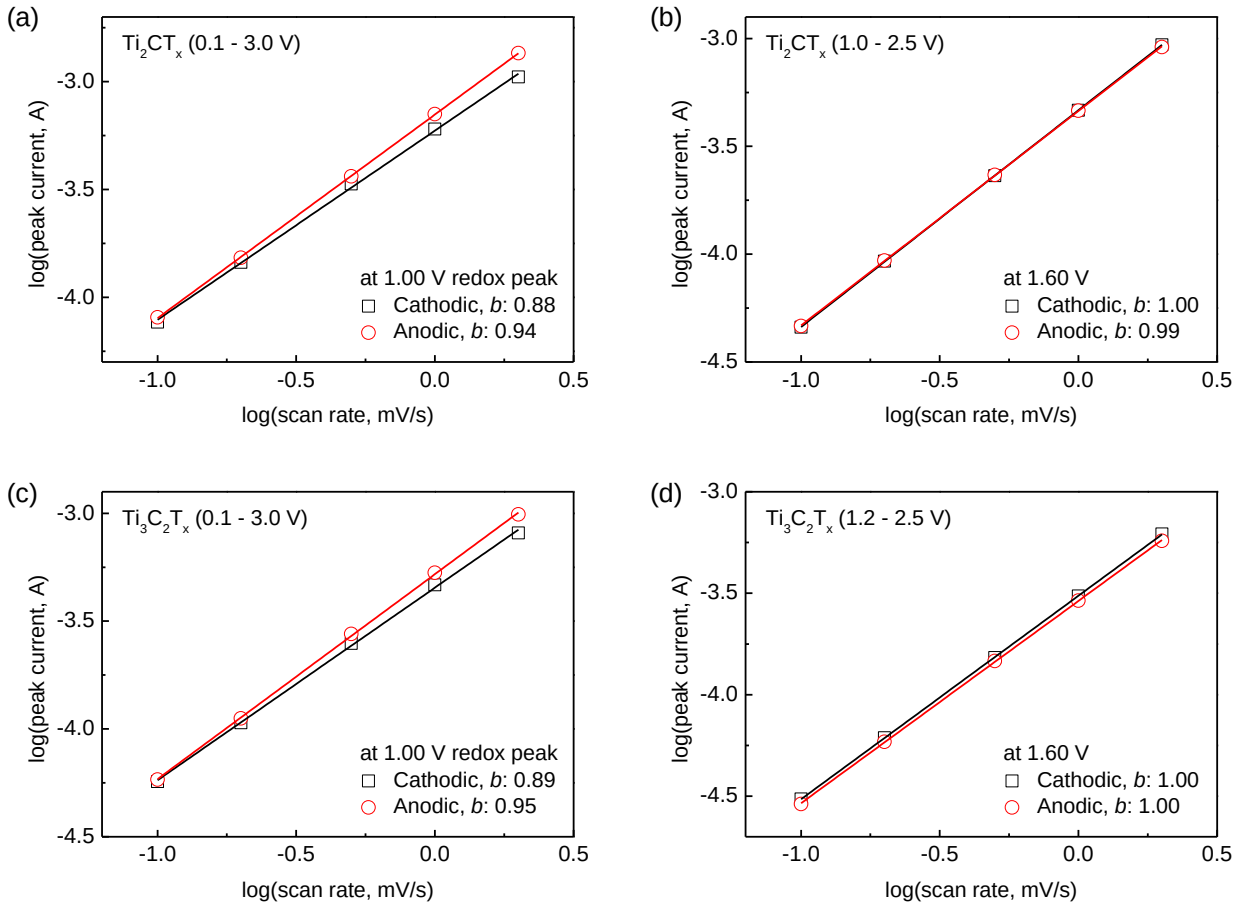

Figure B.2 *b*-value ($i = av^b$ where i is current, v is scan rate, and a and b are adjustable coefficients) determination; Ti_2CT_x in the potential range of (a) 0.1 – 3.0 V and (b) 1.0 – 2.5 V, and $Ti_3C_2T_x$ in the potential range of (c) 0.1 – 3.0 V and (d) 1.2 – 2.5 V with 1 M $LiPF_6$ in EC/DMC (vol.% 1/1). (a), (c) the relationship between the peak current (*ca.*, 1.00 V vs. Li^+/Li) and the scan rate. (b), (d) the relationship between the current at 1.60 V vs. Li^+/Li and the scan rate.

Figure B.2 exhibits the plots of log(i) as a function of log(v) for Ti_2CT_x and $Ti_3C_2T_x$ with different cut-off potential. The currents obey a power-law relationship ($i = av^b$) with the scan rate (0.1 – 2.0 mV/s), which shows a linear proportionality for the plots of log(i) vs. log(v). The *b*-value

of 1.0 indicates that the reaction is surface-controlled while the *b*-value of 0.5 manifests that the reaction is bulk-diffusion-controlled principally observed in intercalation-based materials.[2-4] The cathodic and anodic *b*-values of the current at 1.60 V vs. Li^+/Li for the samples with controlled cut-off potential (1.0 – 2.5 V for Ti_2CT_x and 1.2 – 2.5 V for $Ti_3C_2T_x$) are all 1.00, suggesting that a surface-controlled reaction is dominant (**Figure B.2b and B.2d**) and thus fast. The cathodic and anodic *b*-values of the peak current (*ca.*, 1.00 V vs. Li^+/Li) with full-range potential (0.1 – 3.0 V) for Ti_2CT_x and $Ti_3C_2T_x$ are 0.88/0.94 and 0.89/0.95, indicating that the reaction is partially bulk-diffusion-controlled (**Figure B.2a and B.2c**).

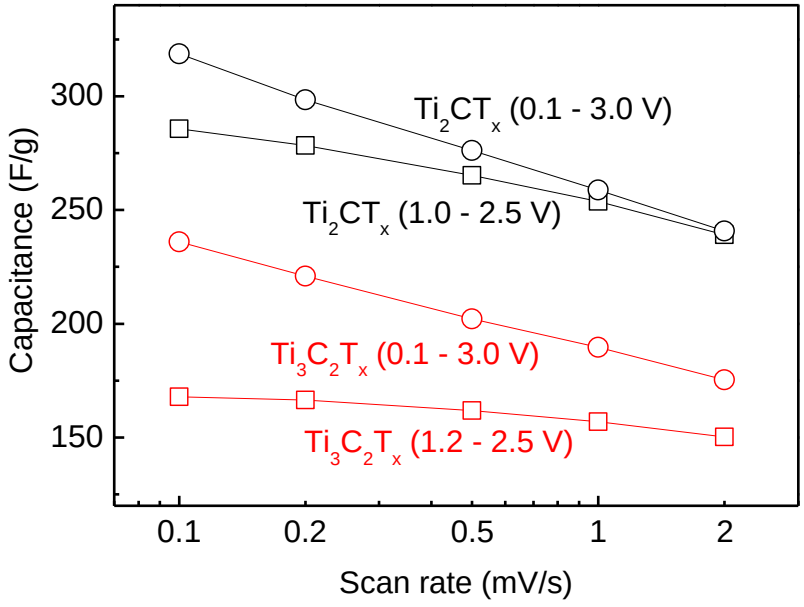

Figure B.3 Rate capability of Ti_2CT_x in the potential range of 0.1 – 3.0 V and 1.0 – 2.5 V, and $Ti_3C_2T_x$ in the potential range of 0.1 – 3.0 V and 1.2 – 2.5 V at various scan rates of 0.1 – 2.0 mV/s with 1 M $LiPF_6$ in EC/DMC (vol.% 1/1).

Redox reaction (*ca.*, 1.00 V vs. Li^+/Li) provides larger capacitances of 350 and 235 F/g for Ti_2CT_x and $Ti_3C_2T_x$ with full-range potential than those with controlled cut-off potential (285 and 170 for Ti_2CT_x and $Ti_3C_2T_x$). However, capacitances with full-range potential decreases sharply with increased scan rate compared to those with controlled cut-off potential. Based on the power-law relationship, the poor rate capability of Ti_2CT_x and $Ti_3C_2T_x$ with full-range potential can be attributed to diffusion barrier in MXene interlayers. Indeed, M. Okubo *et al.*[1] reported that interlayer distance decreases during charging process due to Coulombic attraction between Li^+ and MXene walls and

hence desolvation of solvated-Li^+, leading to the orbital hybridization between Li^+ and MXene walls. It is important to note that other factors (*e.g.*, SEI formation, low conductivity/slow ion diffusion of electrolyte, and low electronic conductivity/slow ion diffusion of Ti_2CT_x) can also be influenced on the rate capabilities of MXenes.

Reference

(1) Okubo, M.; Sugahara, A.; Kajiyama, S.; Yamada, A. MXene as a Charge Storage Host. *Acc. Chem. Res.* **2018**, *51*, 591-599.

(2) Zhang, Q.; Levi, M. D.; Dou, Q.; Lu, Y.; Chai, Y.; Lei, S.; Ji, H.; Liu, B.; Bu, X.; Ma, P.; Yan, X. The Charge Storage Mechanisms of 2D Cation-Intercalated Manganese Oxide in Different Electrolytes. *Adv. Energy Mater.* **2019**, *9*, 1802707.

(3) Augustyn, V.; Come, J.; Lowe, M. A.; Kim, J. W.; Taberna, P.-L.; Tolbert, S. H.; Abruña, H. D.; Simon, P.; Dunn, B. High-Rate Electrochemical Energy Storage through Li^+ Intercalation Pseudocapacitance. *Nat. Mater.* **2013**, *12*, 518–522.

(4) Jung, S.-K.; Kim, H.; Cho, M. G.; Cho, S.-P.; Lee, B.; Kim, H.; Park, Y.-U.; Hong, J.; Park, K.-Y.; Yoon, G.; Seong, W. M.; Cho, Y.; Oh, M. H.; Kim, H.; Gwon, H.; Hwang, I.; Hyeon, T.; Yoon, W.-S.; Kang, K. Lithium-Free Transition Metal Monoxides for Positive Electrodes in Lithium-Ion Batteries. *Nat. Energy* **2017**, *2*, 16208.

Acknowledgments

First of all, I would like to especially thank my supervisor, Prof. Atsuo Yamada, from the bottom of my heart. He gave me great opportunities to do the research in excellent laboratory environments. During the PhD course, his discipline and advice not only make me grow up to be a good student and researcher but also provide many chances to think how to study, how to solve the problems, and even how to live. I am sure that his guidance is very helpful in my future life. Again, I am deeply grateful of Prof. Atsuo Yamada for the encouragement and support. Also, I would like to express special thank of gratitude to Prof. Masashi Okubo from all my heart, too. He is very responsible to manage and guide my studies. He encouraged me to study systematically and think fundamentally every time. A lot of his managements could help me to go to scientifically right direction and come up with new ideas. In addition, I learned an important thing, which is to prepare figures and documents that are required to efficiently show my work to other people. I am really grateful that he has made time to discuss research, give guidance, and support my studies. Again, I am really thankful of Prof. Masashi Okubo for assistance and support during my PhD course. I feel very blessed to have great advisors, both of them, who considerably supported me, in turn, making me realize a lot of things about studies and life that will be very helpful in the future.

I wish to thank 7 committee members (Prof. Atsuo Yamada, Prof. Akira Nakayama, Prof. Ryuji Kikuchi, Prof. Toru Wakihara, Prof. Masashi Okubo, Prof. Yuki Yamada, and Prof. Wataru Sugimoto) for my PhD dissertation. They offered advice and guidance throughout the review of my PhD dissertation, making it high-quality outcome. Through PhD defense, not only my PhD dissertation is much improved but also I learned many things to be equipped as a researcher.

I would like to thank research collaborators and all Yamada-Okubo laboratory members (former and current staffs/students) for kind help and supports. Dr. Yasunobu Ando and Dr. Minoru Otani have contributed computational analysis of MXene/hydrate melt system. Dr. Chi Chen and Dr. Daisuke Nishio-Hamane have contributed computational studies and TEM analysis for phase-pure Mo_2AlB_2, respectively. Dr. Eriko Watanabe gave me opportunities to experience density functional theory (DFT) calculation. Dr. Akira Sugahara, Mr. Hiroki IInuma, and Mr. Yota Haruna with whom I have closely worked, kindly taught me how to use instruments at the first time and discussed with me. I should thank Dr. Qifeng Zheng and Mr. Seongjae Ko for giving me advices and making me fun a lot. Lastly, I should say to thank Japanese students. They have supported a lot of lab chores such as ordering materials and gases, disposing chemicals, making seminar schedules, holding lab parties,

etc.

I am also very grateful to my friends (Minhyuk Lee, Hakyong Lee, and Chaeseung Lim). They support me a lot and made me enjoyable time whenever we met. Finally, I would like to thank my family and relatives, especially my dad and mom, who have supported me and believed in me for 31 years. Without their supports and positive attitude, I believe that I could not study until PhD course. My brother also gave me big encouragement, and always welcomed and treated me well.